TECHNISCHE UNIVERSITÄT MÜNCHEN
LEHRSTUHL FÜR HOCHFREQUENZTECHNIK

# Position Offset Compensated Electromagnetic Cavity Resonators for Sensing Continuous Dielectric Material Streams

Muhammad Usman Faz

Vollständiger Abdruck der von der Fakultät für Elektrotechnik und Informationstechnik der Technischen Universität München zur Erlangung des akademischen Grades eines

*- Doktor-Ingenieurs -*

genehmigten Dissertation.

Vorsitzender: Prof. Dr.-Ing. Christian Jirauschek
Prüfer der Dissertation:
1. Prof. Dr.-Ing. Thomas Eibert
2. Prof. Dr. rer. nat. habil. Bernhard Wolf

Die Dissertation wurde am 07.01.2019 bei der Technischen Universität München eingereicht und durch die Fakultät für Elektrotechnik und Informationstechnik am 20.05.2019 angenommen.

# Abstract

Cavity based sensing and measurement is a well established frequency domain method commonly employed in one or two port configurations to characterize material properties extracted from the measure of the relative permittivity of dielectric specimens. The response of the cavity resonator comprises detuning of the resonance frequency and decrement of the quality factor upon interaction with possibly lossy dielectric objects. A commonly employed cavity resonator based measurement technique involves $TM_{010}$ mode based cylindrical cavities in pill-box shaped designs. In practice, thin rod like cylindrical dielectric specimens to be tested for their electrical or physical properties are either concentrically placed or continuously pass along the axis of the cavity. In the latter case, provisions for insertion holes or openings constitute a mandatory design specification to allow uninterrupted and smooth flow of the samples under test. The inner volume of the cavity marked by the permanent insertion openings of circular shape on the top and bottom lids can be defined as the sensing column of the cavity. It serves as the region where the sample interacts with the electric field of the cavity. In such measurement techniques it is often recommended and highly desired to have homogeneous electric field distribution inside the sensing column with minimal effects from the evanescent fields of the insertion holes. Usually, this specification is met by keeping the insertion holes to a minimum possible size in order to have a fairly good approximation of the homogeneous electric field in the sensing column. However, there exist applications where large insertion openings are needed to accommodate samples of various thicknesses and sizes. It implies the field distribution at all positions in the sensing column can not be treated as uniform and homogeneous due to which the concentric flow of the sample through the sensing column turns into a critical factor. Owing to the presence of various external factors such as lack of mechanical precision and vibrations of the apparatus on which the cavity sensor unit is installed, the concentric flow is neither possible nor guaranteed in practice. Consequently, the lateral movements of usually thin samples during the flow through the relatively larger sensing column characterized by the presence of non uniform field distribution causes false and undesired detuning of the resonance frequency. In order to solve the electric field homogeneity problem a set of solutions comprising optimized designs of the pill box cavity were numerically investigated during various phases of the presented work. The first phase of the solution involves the use of shaped bi-conical inserts made from quartz dielectric around the sensing column to improve the electric field homogeneity. A variety of insert shapes and profiles are numerically investigated with the aid of 3D Electromagnetic Solvers to arrive at an optimal dielectric insert shape. Nevertheless, the dielectric insert based solution mostly influences the uniformity or homogeneity of the longitudinal electric field component. The radial component due to the presence of circular insertion holes remains unaccounted. The second phase of the solution involves a novel cavity sensor configuration for simultaneous mass sensing and position detection. It constitutes a $TM_{010}$ excited cylindrical cavity that is bisected longitudinally in the transverse plane and coupled via a formation of circular apertures in a separating metal wall of finite thickness. The cavity is employed for simultaneous detection of change in mass density in addition to sensing the concentric flow of dielectric specimens. The dielectric sample under test usually in the form of textile fibers or threads concentrically passes the insertion holes in the top and bottom walls as well as the mutual electric coupling aperture of the coupled cavity sections. In contrast to the conventional $TM_{010}$ single mode cavity operation, the symmetrically bisected cavity operates on two resonance modes separated in frequency determined by the type and value of the coupling coefficients. One of the resonance modes that is anti-symmetrical with respect to the bisection plane detects the variations in

mass density of the specimen, similar to the standard permittivity based measurement in $TM_{010}$ cavities. Additionally, the coupled mode which is symmetrical with respect to the bisection plane senses the offset movement from the axial center of the cylindrical cavity. The distinguishing factor between the symmetric and the anti-symmetric electric field distributions is the stronger contribution of the radial component of the electric field and the corresponding stored electric energy for the symmetric resonance mode. The working principle of the coupled cavity method employed as a sensor is discussed and its performance is numerically evaluated and verified through simulations and measurements results.

# Zusammenfassung

Hohlraumresonator basiertes Messen ist eine fest etablierte Frequenzbereichsmethode, die oft in Konfigurationen mit einem oder zwei Messtoren verwendet wird, um Materialeigenschaften zu charakterisieren, die aus der relativen Permittivität von dielektrischen Proben extrahiert werden. Die Antwort des Hohlraumresonators umfasst das Verstimmen der Resonanzfrequenz und das Verringern der Güte bei der Wechselwirkung mit möglicherweise verlustbehafteten dielektrischen Objekten. Eine allgemein verwendete auf einem Hohlraumresonator basierende Messtechnik arbeitet mit $TM_{010}$-Mode-basierten zylindrischen Hohlräumen in Pill-Box-Form. In der Praxis werden dünne stabförmige zylindrische dielektrische Proben, die auf ihre elektrischen oder physikalischen Eigenschaften getestet werden sollen, entweder konzentrisch angeordnet oder durchlaufend entlang der Achse des Hohlraums geführt. Im letzteren Fall ist das Vorhandensein von Ein- und Auslassöffnungen eine verbindliche Entwurfsspezifikation, um den ununterbrochenen und gleichmäßigen Fluss der zu prüfenden Proben zu ermöglichen. Das innere Volumen des Hohlraums, das durch die Einführungsöffnungen mit kreisförmiger Form in den oberen und unteren Deckeln markiert ist, kann als die Messsäule des Hohlraums definiert werden. Es dient als der Bereich, in dem die Probe mit dem elektrischen Feld wechselwirkt. Bei solchen Messtechniken ist es meist empfehlenswert und erwünscht, eine homogene elektrische Feldverteilung innerhalb der Messsäule mit minimalen Auswirkungen durch die evaneszenten Felder der Einführungsöffnungen zu haben. Üblicherweise wird diese Spezifikation erfüllt, indem die Öffnungen möglichst klein gehalten werden, um eine gute Annäherung an ein homogenes elektrisches Feld in der Sensorspalte zu erhalten. Es gibt jedoch Anwendungen, bei denen große Öffnungen benötigt werden, um Proben verschiedener Dicken und Größen aufzunehmen. Dies impliziert, dass die Feldverteilung in der Messsäule nicht an allen Positionen homogen ist, wodurch der konzentrische Fluss der Probe durch die Messsäule ein kritischer Faktor wird. Aufgrund des Vorhandenseins verschiedener äußerer Faktoren, wie zum Beispiel mangelnde mechanische Präzision und Vibrationen der Vorrichtung, auf der die Hohlraumsensoreinheit installiert ist, ist der konzentrische Fluss in der Praxis oft weder möglich noch garantiert. Folglich verursachen die lateralen Bewegungen von üblicherweise dünnen Proben während der Strömung durch die relativ große Messsäule, die durch das Vorhandensein einer ungleichmäßigen Feldverteilung gekennzeichnet ist, eine falsche und unerwünschte Verstimmung der Resonanzfrequenz. Um das Problem der elektrischen Feldhomogenität zu lösen, wurde eine Reihe von Lösungen mit optimierten Designs des Pillbox-Hohlraums in verschiedenen Phasen der vorgestellten Arbeit untersucht. Die erste Phase der Lösung beinhaltet die Verwendung von speziell geformten bikonischen Einsätzen, die aus Quarzdielektrikum um die Messsäule herum hergestellt sind, um die Homogenität des elektrischen Feldes zu verbessern. Eine Vielzahl von Einsatzformen und -profilen wird numerisch mit Hilfe von 3D Feldlösern untersucht, um eine optimale dielektrische Einsatzform zu erhalten. Die auf dem dielektrischen Einsatz basierende Lösung beeinflusst hauptsächlich die Gleichförmigkeit oder Homogenität der longitudinalen elektrischen Feldkomponente. Die radiale Komponente aufgrund des Vorhandenseins von kreisförm Öffnungen bleibt unberücksichtigt. Die zweite Phase der Lösung beinhaltet eine neuartige Hohlraumsensorkonfiguration für die gleichzeitige Erfassung der Masse und der Position. Sie besteht aus einem $TM_{010}$-angeregten zylindrischen Hohlraum, der in der Querebene in Längsrichtung halbiert und über eine Anordnung von kreisförmigen Öffnungen in einer trennenden Metallwand mit endlicher Dicke gekoppelt ist. Der Hohlraum wird zur gleichzeitigen Erfassung der Änderung der Masse und des konzentrischen Flusses der dielektrischen Proben verwendet. Die zu testende dielektrische Probe, zum Beispiel in Form von Textilfasern oder -fäden, durchläuft konzentrisch die Einführungslöcher in den

oberen und unteren Wänden sowie die gegenseitige elektrische Kopplungsöffnung der gekoppelten Hohlraumabschnitte. Im Gegensatz zum herkömmlichen $TM_{010}$-Einmodenhohlraumbetrieb arbeitet der symmetrisch halbierte Hohlraum auf zwei Resonanzmoden, die in der Frequenz getrennt sind, abhängig von der Art und der Stärke der Kopplungs. Einer der Resonanzmodi, der anti-symmetrisch in Bezug auf die Bisektionsebene ist, detektiert die Variationen in der Masse der Probe, ähnlich der Standard-Permittivitätsmessung in $TM_{010}$-Hohlräumen. Zusätzlich erfasst der gekoppelte Modus, der in Bezug auf die Bisektionsebene symmetrisch ist, die Versatzbewegung von der axialen Mitte des zylindrischen Hohlraums. Der Unterschied in der Funktionalität zwischen den eng auftretenden Resonanzmoden ist auf die symmetrische und die anti-symmetrische Verteilung der Felder im Hohlraum zurückzuführen. Der Unterscheidungsfaktor zwischen den symmetrischen und den anti-symmetrischen elektrischen Feldverteilungen ist der stärkere Beitrag der radialen Komponente des elektrischen Feldes und der entsprechenden gespeicherten elektrischen Energie beim symmetrischen Resonanzmodus. Das Arbeitsprinzip des gekoppelten Hohlraumverfahrens, das als Sensor verwendet wird, wird diskutiert und seine Leistungsfähigkeit wird numerisch ausgewertet und durch Simulationen und Messergebnisse verifiziert.

# Contents

# List of Figures

# List of Tables

# 1 Microwave Sensors: An Overview

The term microwave sensor is commonly used for electromagnetic structures which generate distinguishable and measurable responses upon interaction with various materials having certain electromagnetic characteristics. In principle, microwave sensors undergo transducer effects of electromagnetic nature corresponding to the properties of the material under test. The significance and the utility of microwave sensors date back to the early development era of electromagnetic methods for wave propagation and resonances. Over the decades improvements in microwave sensing techniques have taken place owing to prolific research and development [Baker-Jarvis et al., 2010]. In recent times, the emergence of advanced electromagnetic computational tools, for example CST Microwave Studio [Computer Simulation Technology, 2017], have paved the way for further development in improving the design aspects of microwave sensing techniques. Such computational tools obtain the solution of an electromagnetic problem by employing a number of efficient algorithms and meshing schemes. The utility of microwave sensors is further established due to an ever growing demand for characterization of novel materials. Microwave sensors constitute a wide range of realizable forms, with each realization being unique in its characteristics and applicability to a certain set of problems. This chapter reviews the significance and the utility of microwave sensors which are commonly employed in a number of applications. The review contains an account of classification of microwave sensors based on the principle of operation and practical application. Additionally, the motivation for the presented work followed by the background of the problem in question are detailed in the concluding section of the ongoing chapter.

## 1.1 Material Characterization

The techniques for material characterization have an ever-expanding range of applications from laboratory testing to a variety of industrial environments. Material characterization is essentially the process of analysing the properties of materials, which are identified under the terms of electric permittivity, symbolized as $\epsilon$, and the magnetic permeability, denoted by $\mu$. The appropriate selection of a sensing technique is usually based on required design parameters and specifications. When there exists a correlation between the electric and the non-electric nature of test materials, physical and chemical compositions as well as the shape features of materials can also be extracted from the measured permittivity and permeability data [Kraszewski and Nelson, 1992, 1991b]. A few examples of these non electric quantities include properties of density, moisture content, thickness or similar physical features. For instance, the percentage of moisture in a test sample or the increase in the volume of a sample have proportional effects on the electromagnetic response. Such effects can solely be deduced from the electromagnetic response, provided the permittivity and permeability of the sample are known prior to the test. Hence, it is of foremost significance to quantitatively define the nature and behaviour of a medium under the influence of an electromagnetic field, before discussing appropriate microwave measurement techniques.

### 1.1.1 Dielectric Properties

The electric and the magnetic properties of materials are defined by the dielectric permittivity tensor $\boldsymbol{\epsilon}$ and the magnetic permeability tensor $\boldsymbol{\mu}$ via the constitutive relations, which are stated as [Harrington, 2001]

$$\boldsymbol{D} = \boldsymbol{\epsilon} \cdot \boldsymbol{E} \qquad \text{and} \qquad \boldsymbol{B} = \boldsymbol{\mu} \cdot \boldsymbol{H}, \tag{1.1}$$

respectively. In the above expressions under $e^{j\omega t}$ time convention, $\boldsymbol{E}$ and $\boldsymbol{H}$ are time harmonic vectors representing electric and magnetic fields, measured in $^{\mathrm{V}}/_{\mathrm{m}}$ and $^{\mathrm{A}}/_{\mathrm{m}}$. In addition, the vectors $\boldsymbol{D}$ and $\boldsymbol{B}$ represent time harmonic electric and magnetic flux densities, measured in $^{\mathrm{As}}/_{\mathrm{m}^2}$ and $^{\mathrm{Vs}}/_{\mathrm{m}^2}$. The permittivity and the permeability can be specified in a dyadic representation of a $3 \times 3$ matrix stated in Cartesian vector components as [Balanis, 2012]

$$\boldsymbol{\epsilon} = \begin{bmatrix} \epsilon_{xx} & \epsilon_{xy} & \epsilon_{xz} \\ \epsilon_{yx} & \epsilon_{yy} & \epsilon_{yz} \\ \epsilon_{zx} & \epsilon_{zy} & \epsilon_{zz} \end{bmatrix} \qquad \text{and} \qquad \boldsymbol{\mu} = \begin{bmatrix} \mu_{xx} & \mu_{xy} & \mu_{xz} \\ \mu_{yx} & \mu_{yy} & \mu_{yz} \\ \mu_{zx} & \mu_{zy} & \mu_{zz} \end{bmatrix} \quad ,$$

respectively. In the above representation, each matrix entry represents the complex permittivity with its respective subscript indicating the corresponding component. For example, $D_x = \epsilon_{xy} E_y$ represents the scalar value of permittivity, relating $D_x$ and $E_y$ components. Generally, anisotropic materials have all non-zero matrix entries, whereas in few cases such as passive reciprocal ionic single crystals only diagonal elements ($\epsilon_{xx}, \epsilon_{yy}, \epsilon_{zz}$) are non-zero [Krupka, 2006]. The permittivity representation reduces to a scalar quantity for isotropic, passive and reciprocal materials, which mostly include polycrystalline solids of glass and plastics. The electric permittivity of a dielectric material is often stated in terms of the unit-less relative permittivity $\epsilon_r$, which is defined as the ratio of a material's permittivity value $\epsilon$ to the absolute permittivity of vacuum $\epsilon_0$, with value given as $\epsilon_0 \approx 8.854 \times 10^{-12}\,^{\mathrm{F}}/_{\mathrm{m}}$. Similarly, the relative magnetic permeability given by the relative permeability term $\mu_r$ is considered unity for non-magnetic materials, i.e. $\mu_r = 1$. In complex frequency domain with time convention $e^{j\omega t}$, the phasor form of the Maxwell's equation of magnetic curl is stated as [Pozar, 2011]

$$\nabla \times \boldsymbol{H} = j\omega \boldsymbol{D} + \boldsymbol{J}, \tag{1.2}$$

where

- $\boldsymbol{H}$ is the magnetic field expressed in dimensions of $^{\mathrm{A}}/_{\mathrm{m}}$.
- $\boldsymbol{D}$ is the electric displacement vector in $^{\mathrm{As}}/_{\mathrm{m}^2}$.
- $\boldsymbol{J} = \boldsymbol{J}_s + \boldsymbol{J}_c$ is the sum of impressed and conduction current densities in $^{\mathrm{A}}/_{\mathrm{m}^2}$, respectively.
- $\omega = 2\pi f$ is the angular frequency for harmonic signals with assumed time factor of $e^{j\omega t}$.

In source-free media with zero impressed current ($\boldsymbol{J_s} = 0$), the above magnetic curl equation can be expressed as a general sum of only induced currents [Harrington, 2001],

$$\nabla \times \boldsymbol{H} = (j\omega\epsilon + \sigma)\boldsymbol{E}, \tag{1.3}$$

where the definition of the displacement current density, i.e. $= \boldsymbol{J}_d = j\omega\boldsymbol{D} = j\omega\epsilon\boldsymbol{E}$, and the conduction current density, i.e. $\boldsymbol{J}_c = \sigma\boldsymbol{E}$, are used. The displacement current density indicates the sum of free space and bounded charges in a medium proportional to the electric permittivity $\epsilon$, whereas the conduction current density represents the current due to conductivity $\sigma$ in conducting media like metal surfaces or walls.

Dielectric materials usually have negligible conductivity ($\sigma \approx 0$) due to the rare number of free conductive charges. Therefore, the sum of induced currents can be restricted to the contribution from free-space displacement currents contributed by $\epsilon_0$, and currents caused by bounded charges, which collectively fall under the category of polarization currents. Bounded charges in a dielectric medium occur, when atoms or molecules constituting the dielectric, align themselves in a definite order under the influence of an externally applied electric field. This alignment causes polarization currents which are represented by the electric polarization $\boldsymbol{P_e}$.

Hence, the total electric displacement vector $\boldsymbol{D}$ is the sum of the applied field $\boldsymbol{E}$ and the polarization vector $\boldsymbol{P_e}$ as [Pozar, 2011]

$$\boldsymbol{D} = \epsilon_0 \boldsymbol{E} + \boldsymbol{P_e}. \tag{1.4}$$

In linear media the orientation of the applied field $\boldsymbol{E}$ and the electric polarization $\boldsymbol{P_e}$ are identical, therefore, the relationship between these quantities is proportional to the electric susceptibility $\chi_e$ of the medium given by [Pozar, 2011]

$$\boldsymbol{P_e} = \epsilon_0 \chi_e \boldsymbol{E}. \tag{1.5}$$

Using Eq.(1.4) and (1.5), the static relative permittivity $\epsilon_r$ of the medium can be defined as [Pozar, 2011]

$$\epsilon = \epsilon_0(1 + \chi_e) = \epsilon_0 \epsilon_r. \tag{1.6}$$

In general, the susceptibility $\chi_e = \chi_e' - j\chi_e''$ is a complex number, because of which the permittivity $\epsilon$ of a linear and isotropic medium can be stated as the sum of real and imaginary components under the complex permittivity $\hat{\epsilon}$, or equivalently the relative permittivity $\epsilon_r$ notation [Afsar et al., 1986]

$$\hat{\epsilon} = \epsilon' - j\epsilon'' = (\epsilon_r' - j\epsilon_r'')\epsilon_0 = \epsilon_r \epsilon_0, \tag{1.7}$$

where the real part $\epsilon_r'$ represents the reactive current or the dielectric strength of the material. The imaginary part $\epsilon_r''$ represents the dissipative current contribution as heat losses caused by the damping of dipole moments. Both real and imaginary components are actually frequency-dependent functions with each having a different dependence, however, they can be usually considered constant over a narrow frequency band. In practice, another notation representing the dissipation is called dielectric loss tangent $\tan\delta$, which is the ratio of the imaginary to the real permittivity component [Collin, 2001],

$$\epsilon_r \epsilon_0 = \epsilon_0 \epsilon_r'(1 - j\tan\delta). \tag{1.8}$$

From a physics point of view, the source of the loss mechanism comprises different physical processes such as electrical conduction, dielectric relaxation, dielectric resonance as well as loss contributions from non-linear processes [Krupka, 2006]. The loss tangent $\tan\delta$ is an all-inclusive term representing dissipation originating from conduction currents due to $\sigma$ and frequency dependent reactive currents due to $\hat{\epsilon}$ [Collin, 2001],

$$\tan\delta = \frac{\omega\epsilon'' + \sigma}{\omega\epsilon'}. \tag{1.9}$$

For non-conductive materials the equation simplifies to the ratio of the imaginary permittivity to the real permittivity,

$$\tan\delta = \frac{\epsilon''}{\epsilon'} = \frac{\epsilon_r''}{\epsilon_r'}. \tag{1.10}$$

In summary, while stating dielectric properties of a material in its specification sheet, relative permittivity $\epsilon_r$ is the convention used to mention the dielectric strength. Similarly, the practical measure of dissipation is represented by $\tan\delta$ as per Eq.(1.9) and (1.10). Together, both quantities represent the fundamental parameters that uniquely and quantitatively define the electrical properties of any dielectric material.

### 1.1.2 Measurement Methods

There are several realizable forms of material sensing techniques in the frequency domain, ranging from DC to millimeter wave and further up to the optical region of the electromagnetic spectrum. The primary distinguishing factor among these techniques resides in the type of response a sensor produces upon interaction with a dielectric material. Lumped elements are usually concerned with changes in static capacitance measurement caused by the presence of a sample. Microwave methods employ waveguides, antennas, and cavity resonators which produce the so called electromagnetic wave response. Above the microwave and millimeter-wave regions optical sensing systems are utilized where the properties of non-magnetic test materials are treated in terms of the refractive index, whose scalar measure is given by the relation $n = \sqrt{\epsilon_r}$.

#### 1.1.2.1 Circuit Based Methods

Lumped circuit methods used from DC to low frequencies (commonly up to 1 -10 MHz) generate the response as a change in the complex impedance ($Z = R + jX$) or inversely in the complex admittance ($Y = G+jB$). In practice, these impedance or admittance characteristics are usually recorded using balanced bridge setups [Bussey, 1967]. In such capacitance based measurement setups, dielectric samples are usually placed between a pair of parallel plate electrodes. The dielectric properties at lower frequencies are extracted from the measurement of the difference of the capacitance with and without the sample, i.e. $\Delta C = C' - C_0$, respectively. The parallel sum capacitance in the presence of the sample between electrodes is given by

$$C' = C_0 + \Delta C = (1 + \hat{\epsilon_r})\epsilon_0 \frac{S}{d}, \tag{1.11}$$

where $S$ represents the surface area of the electrode plates and $d$ the distance between the plates. Dielectric losses are extracted from the change in the real part or the conductance ($\Re\{\Delta Y\} = \Delta G$), whereas the value of the real permittivity is determined from the change in the imaginary component or the susceptance ($\Im\{\Delta Y\} = \Delta B$). Using the relation $Y + \Delta Y = j\omega(C_0 + \Delta C)$ [Bussey, 1967],

$$\epsilon_r' = 1 + \frac{\Delta C}{C_0}, \tag{1.12a}$$

$$\epsilon_r'' = \frac{\Delta G}{\omega C_0}, \tag{1.12b}$$

i.e., both real and imaginary permittivity components are evaluated, respectively. This technique of lumped circuit measurements is also known as admittance cell technique.

#### 1.1.2.2 Microwave Methods

The methods for characterization of dielectric materials at higher frequencies up to millimeter waves collectively fall under the techniques of microwave sensing and measurement. The microwave response in the form of electromagnetic wave quantities, whether as propagating or standing waves, constitute a specific relation to the dielectric properties of the material under test. When compared to other methods, microwave techniques owe their practical viability to the efficient generation, transmission and detection of coherent electromagnetic signals [Stuchly and Hamid, 1971]. The attenuation or loss of the microwave signal caused by environmental effects of moisture, dirt, water vapours or any other contamination source is of relatively low degree [Stuchly and Hamid, 1971]. Furthermore, microwaves can penetrate into low-loss dielectrics and provide medium to high levels of sensitivity. The benefits of employing microwave sensors for material characterization and measurement are summed up as follows:

1. **Non-destructive Sensing:** Microwave sensors are effectively non-destructive in nature while performing measurements. The sample under test does not undergo any physical or chemical alteration due to its interaction with the microwave sensor. The non-destructive property of microwave methods can be attributed to the common practice of using sensors at lower power levels which ensures that the microwave energy does not alter the nature of the test object. For example, a sensor is usually required to be connected in the first stage with an op-amp in certain voltage follower configurations, in order to provide the needed gain and eventually drive the current in the circuitry.

2. **Broad Operating Range:** Measurements in microwave sensors takes place over the entire volume or the area of the sample. In the microwave region there is a wide spectrum of frequencies and wavelengths to opt for material characterization. Thus the operation frequency and hence proper wavelength can be chosen to match the object dimension. The sample undergoes uniform illumination to attain a fair degree of accuracy. As a consequence, the unnecessary influences of local deformities, like surface roughness, on the measurement are mitigated accordingly.

3. **Contactless Measurement:** Measurements performed by microwave sensors are effectively contactless. For open structures and unbounded regions, like antennas, the term is self-explanatory. However, for closed cavities the contact-less measurement is ensured by selecting a proper geometry of the cavity and an appropriate placement of the sample.

4. **Continuous Sensing:** Measurements carried out by using a microwave sensor are mostly continuous and can be applied in real-time situations. Particularly, in industrial applications for automated and monitoring systems microwave sensors can very well be integrated into the control system to provide real time closed feedback to the process speed or other required control variables.

5. **Robustness:** The measurement setup of microwave sensors has the capability to withstand variations in temperature, pressure and humidity within the operational domain. This property of microwave sensors owes its characteristic to the robustness of metal or other low loss ceramic materials commonly used in the construction and fabrication of sensors.

## 1.2 Categorization of Microwave Sensors

In microwave methods the specific relation between the electromagnetic wave quantities of the sensor and the dielectric properties of the medium involved is the key to characterize the material under observation. The wave quantities of a microwave sensor fundamentally depend on the applicator setup or the fixture employed for performing the measurements. These fixtures include coaxial lines, rectangular and circular waveguides, antennas of various types, and cavities of different shapes which are either made from metal or low-loss ceramics. The measurement fixtures can be further classified according to the response they produce, i.e. either the time-domain or the frequency domain. Restricting to the frequency response, it can further be sub-divided into two major categories of broadband and discrete frequency types. Broadband methods provide a continuous frequency sweep over an allowed band of electromagnetic signals that pass through the fixture. In comparison discrete frequency applicators, such as cavity resonators, operate at either single or multiple yet discrete frequency modes of resonances. Furthermore, the practical choice of the type of a microwave sensor is partly governed by the physical composition and the state of sample materials involved. Solid bulk form [Kumar and Singh, 2007], thin laminated films [Thomas and Dube, 1997], liquid samples inside capillary tubes or sample holders [Gregory and Clarke, 2006], or even pressurized ionized gaseous state [Rouleau et al., 2001] are some common types of sample forms that are usually required to be characterized in microwave sensing

applications. Consequently, preparation of samples in required shapes and states are critical factors in the selection of a suitable fixture or an applicator geometry.

In the following overview, microwave sensors are broadly categorized into two large groups comprising non-resonance and resonance methods. The classification is primarily based on the response of the applicator employed for measuring the properties of the material under test. Propagating wave responses in broad frequency sweeps are tied together under the category of non-resonance methods. These are realized in different forms of closed or open-ended transmission lines and narrow beam radiators. On the other hand, resonance based techniques which are realized as closed cavity structures, exhibit the response in the form of a discrete set of resonance modes.

### 1.2.1 Non-Resonance Techniques

The non-resonance techniques employ propagating wave methods which work either with guided structures or with free space radiators. These methods are concerned with the measurement of the change in transmitted and reflected electromagnetic signals in the presence of a dielectric sample. The sample is appropriately dimensioned and positioned in the field of an incident electromagnetic wave. The phenomenon of reflection and transmission occurs at the sample interfaces when the sample is illuminated by the wave. In one-port reflection methods the measured complex reflection coefficient ($\mathbf{\Gamma} = |\Gamma|e^{-j\theta}$), i.e. the magnitude and phase of the reflection coefficient is sufficient to deduce the dielectric properties of a bulk material piece, which can not be usually shaped into a suitable form. When the materials are non-reciprocal in nature, transmission type measurements with both the values of transmission ( $T$) and reflection ($\Gamma$) coefficients are required. For passive reciprocal materials the phase and magnitude of the transmission coefficient would suffice, if either of the two sample quantities of thickness or the dielectric permittivity are known prior to the measurement.

Mathematically, the change in transmitted and reflected power is due to the difference in propagating wave parameters occurring as a consequence of the absence and the presence of the dielectric sample. A propagating wave inside a transmission medium can be quantitatively described by the complex propagation coefficient, i.e. $\gamma$, and the characteristic impedance $Z_0$ of the transmission medium. Both quantities are interlinked wave parameters with direct dependence on the medium permittivity $\epsilon$ and the permeability $\mu$. In a lossless medium, for example free space ($\epsilon_r = 1$ and $\mu_r$=1) the relationship can be simply expressed as [Balanis, 2012]

$$\gamma_0 = j\omega\sqrt{\epsilon_0\mu_0} = jk_0 \qquad \text{and} \qquad Z_0 = \sqrt{\mu_0/\epsilon_0}, \tag{1.13}$$

where only the imaginary part of the complex propagation, $\gamma = jk$, is used with $k_0$ specifying the free space wavenumber of a uniform plane wave. In general lossy media, the complex term propagation coefficient $\gamma$ is defined as the sum of the attenuation coefficient $\alpha$ or the real part, and the phase coefficient $\beta$ or the imaginary part. For guided structures the propagation coefficient of any non-magnetic dielectric material with complex permittivity $\epsilon_r = \epsilon_r' - j\epsilon_r''$ can be stated as [Balanis, 2012]

$$\gamma = \alpha + j\beta = j\sqrt{k_c^2 - k_0^2\epsilon_r}, \tag{1.14}$$

where the free space and the cut-off wavenumbers of the waveguide are mentioned, which can also be stated in terms of the respective wavelengths, given by $k_0 = 2\pi/\lambda_0$ and $k_c = 2\pi/\lambda_c$. Here, $\lambda_c$ the cut-off wavelength is dependent on the broader transverse dimension of the waveguide. For purely transverse electromagnetic (TEM) waves, which are characterized by the electric and the magnetic fields lying in the plane transverse to the direction of propagation, the cut off wavenumber $k_c$ is zero ($k_c = 0$) and the cut-off wavelength $\lambda_c$ goes to infinity, so the Eq.(1.14) reduces to $\gamma = jk_0\hat{\epsilon}$. The examples of such TEM waves include uniform plane waves in free space and the fundamental propagation mode of coaxial lines. In hollow waveguides,

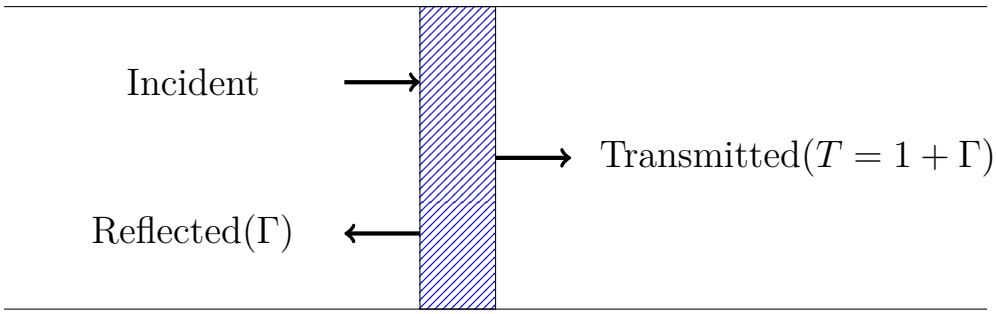


Figure 1.1: General depiction of a two-port non-resonance scheme

where a component of the electric or the magnetic or both fields lie in the longitudinal direction of the propagating wave, the cut off wavenumber $k_c$ has some finite real value. For instance, the impedance expression for the transverse electric (TE) wave propagation, where the longitudinal electric field component is zero but the magnetic component is non-zero, in terms of the propagation coefficient $\gamma$ is expressed as [Balanis, 2012]

$$Z = \frac{j\omega\mu_0}{\gamma}, \tag{1.15}$$

which is real for lossless propagation and imaginary for the non-propagating or the evanescent case. In non-resonance methods these characteristic wave parameters of $\gamma$ and $Z$ are measured via a vector network analyser (VNA) in the form of the scattering parameters, which represent the reflected and transmitted power. For a waveguide in two-port configuration, as depicted in Fig.1.1 with an appropriate sample placed inside the waveguide, the ratios of reflected and transmitted waves to incident wave quantities in terms of impedances are stated as [Pozar, 2011]

$$\Gamma = \frac{Z - Z_0}{Z + Z_0}, \tag{1.16a}$$

$$T = \frac{2Z}{Z + Z_0}, \tag{1.16b}$$

where $Z = j\omega\mu_0/\gamma$ and $Z_0 = j\omega\mu_0/\gamma_0$ are the complex impedances of the waveguide with and without the sample of the material, respectively. The measured values of the reflected and the transmitted signals are extracted from the scattering parameters, namely, $\boldsymbol{S_{11}}$ and $\boldsymbol{S_{21}}$ while taking a broad frequency sweep. Consequently, the differences in the wave impedance and the associated propagation coefficient are deduced. Eventually, real and imaginary components of the complex permittivity of the material can be extracted using the relations [Saeed et al., 2002]

$$\epsilon' = \frac{k_c^2 - \alpha^2 + \beta^2}{k_0^2}, \tag{1.17a}$$

$$\epsilon'' = \frac{2\alpha\beta}{k_0^2}. \tag{1.17b}$$

#### 1.2.1.1 Guided Wave

Guided wave techniques are also referred to as closed cell methods, since they are implemented in various types of closed transmission line structures. In this technique, either TEM based coaxial guides or transverse electric/magnetic (TE/TM) mode based hollow waveguide structures are employed as sensors or applicators. In some instances, quasi-TEM structures like

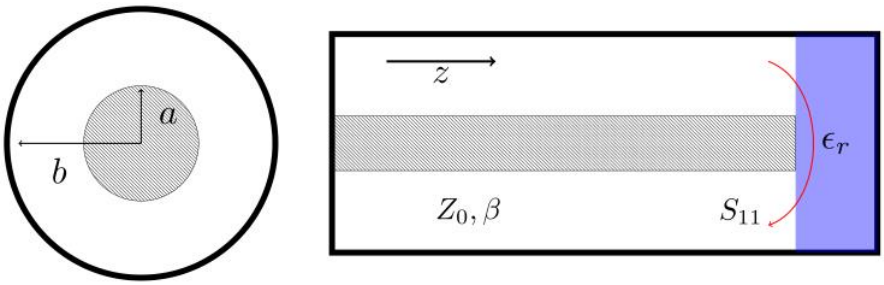


(a) One-Port Setup

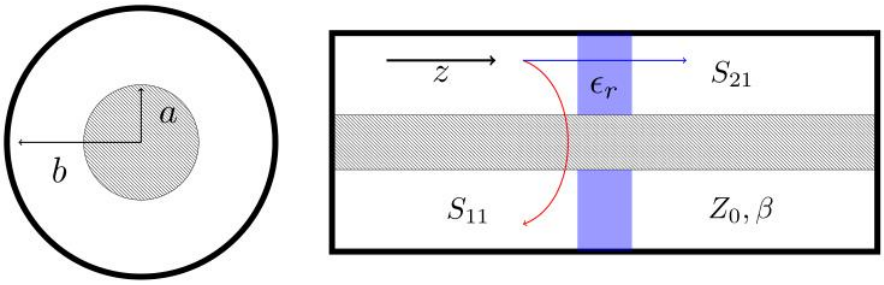


(b) Two-Port Setup

Figure 1.2: Coaxial Configurations

planar or etched transmission lines are also implemented, that include coplanar and micro-strip methods [Saeed et al., 2002; Narayanan, 2014]. Usually these techniques involve placing or filling an appropriately dimensioned sample of a dielectric material inside a section of closed guided structures. The optimal choices of sample dimensions and shape are governed by the type of guide applied for the measurement purpose. The suitable sample shapes are either in the form of thick and flat rectangular slabs fitted inside hollow rectangular waveguides, or annular concentric rings mounted over inner coaxial conductors, or thick cylindrical discs fitted at the end of coaxial waveguides [Venkatesh and Raghavan, 2005]. On the other hand, samples in the form of substrate or superstrate films or similar planar shapes are usually suitable for etched transmission line applicators [Ocera et al., 2006].

Partially transmitted and reflected portions of the incident energy are extracted from the reflection ($\Gamma$) and the transmission ($T$) coefficients, which are computed directly from the measured scattering parameters. Closed transmission lines are operated over the entire broad range of allowed propagating modes either in two-port configurations, as shown in Figs.1.2a and 1.3a, or in closed short-circuited cells also called one-port reflectometry schemes [Gregory and Clarke, 2006], as depicted in Figs.1.2b and 1.3b. The choice of port configuration is usually governed by the physical state and the dissipation ability of the material under test. Two-port configurations are preferred for relatively low real permittivity values with medium level of losses. In contrast, one-port schemes or reflectometry methods are a viable option when the materials under test have higher losses and dissipation besides larger permittivity values. The reason for such a distinction is attributed to the insertion loss value that tends to increase due to a high loss factor of the material. Moreover, the impedance mismatch for large permittivity values also reduces the accuracy of the two-port configuration [Krupka, 2006].

Robert and Van Hippel are the pioneers of one-port closed transmission line sensors [Afsar et al., 1986]. The technique proposed in their work requires a sample with thickness equal to the odd multiples of a quarter wavelength ($n\lambda/4, n = 1, 3, 5, ....$) inserted into a coaxial waveguide with radial ratio $b/a$, as depicted in Fig.1.2a. The shorted end in the scheme is usually fixed but it can also be provided with a moveable shorted wall or plunger to allow for a number of measurements in regions of the varying electric field.

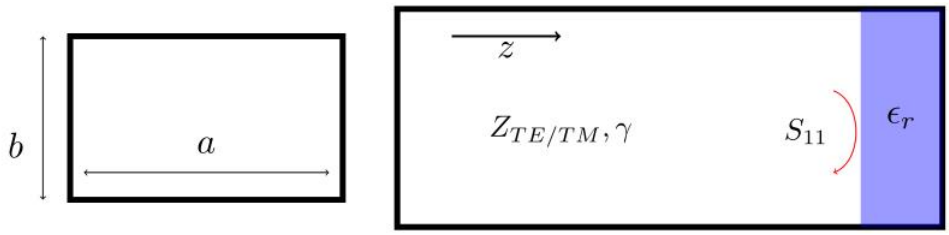


(a) One-Port Setup

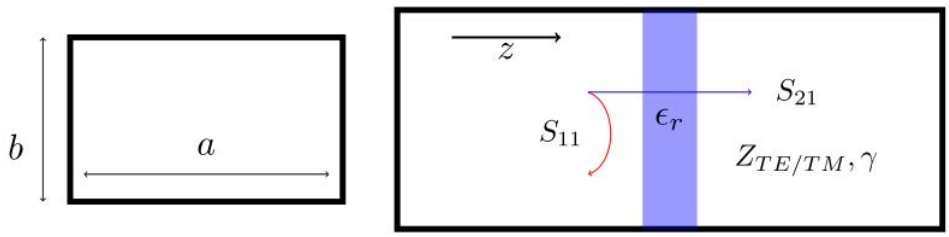


(b) Two-Port Setup

Figure 1.3: Waveguide Configurations

Coaxial waveguides provide the operating range for material sensing typically within 10 GHz, whereas hollow waveguides generally operate to a higher theoretical limit of 30 GHz. In practice, beyond 10 GHz the parasitic losses increase and the influence of imperfections in the measurement becomes a significant factor due to smaller dimensions of the sample size. In addition, the probable occurrence of resonances inside the sample particularly with relatively larger dimensions also tends to disturb the desired measurement. In order to avoid sample resonances in two-port schemes, the thickness of the sample should not be allowed to reach half of a wavelength or multiples of half wavelengths at the operating frequencies.

The major limitation of guided wave measurement techniques is the air-gap problem. It occurs due to the inevitable air-dielectric interface between the applicator's conductor and the sample's dielectric. The air gaps cause an additional series or parallel capacitive effect depending upon the orientation of the applied electric field. The air-gap problem is particularly critical for solid samples with large real permittivity inside coaxial waveguides due to the presence of an inner conductor. It has to be accounted for by using correction factors, otherwise it causes substantial errors in permittivity based evaluations. Some practical solutions against air gap problems include applying metallization and covering the space with conductive pastes or solders, though such compensations cause reduced accuracy in loss measurements [Krupka, 2006]. In comparison, the air gap problem is relatively less critical in hollow waveguide geometries simply due to the absence of an inner conductor.

#### 1.2.1.2 Free-space Techniques

Free-space techniques have a similar principle of operation as guided wave methods. A pair of radiating antennas is used as applicators to test and measure the properties of the sample placed in between the radiators, as depicted in Fig.1.4. Sample preparations in free-space techniques have relatively less stringent requirements as compared to guided methods. Nevertheless, samples should have flat and smooth surfaces at the air-dielectric interface. Moreover, the lateral dimensions of samples should be large enough to avoid the scattering phenomenon from their edges. The condition on the lateral size of the sample is set by the electromagnetic beamwidth of the radiating antennas. Alternatively, attempts are made to employ narrow beam antennas, such as horn-shaped waveguide antennas, to accomplish minimally divergent beams.

The measured quantities for a sample placed between transmitting and receiving antennas are the attenuation and the phase shift of the radiated signal. The extracted measurements

are translated into a fitting mathematical model to establish a relationship with the complex permittivity and other derived quantities of non-electrical nature. Samples with medium level of losses yet homogeneous in nature yield results with higher accuracy. Free-space methods work well for the high frequencies above 10 GHz and they are practically suited for harsh environments such as high temperature regions inside boiler pipes or tubes. Moreover, these techniques have the advantage of performing continuous and real time measurements of the sample because it is possible for unbounded material streams to flow in a contact-less fashion along a fixed transverse plane.

The accuracy of free-space techniques is dependent on the measurement system and the validity of the mathematical model used for computations. The simplified computational model comprises a propagating uniform plane wave interacting at the flat surface of a homogeneous dielectric sample extending to infinity in the lateral plane, causing zero diffraction from the edges. In practice, these simplified assumptions need to be accounted for in final computations to compensate for possible irregularities within the sample and at the surfaces and edges. In addition, some other sources of error include the phenomenon of multiple reflections caused by the surroundings and mismatching errors for high permittivity materials [Venkatesh and Raghavan, 2005]. Moreover, when unfocussed beams are employed there exists a need for compensating the diverging portions of the beams by including an additional attenuation factor between transmission and reception. In order to avoid corrections for diverging beams in the computations, focused beam are rather employed with the help of dielectric lenses and concave mirrors. Another example of a focussed beam is the calculable Gaussian beam radiated from corrugated horn antennas [Krupka, 2006]. The beam decays exponentially as the Gaussian function in radial direction resulting in minimal diffraction at the edges of samples and the antenna apparatus.

#### 1.2.1.3 Open Cell

The open cell or open-ended transmission line method is one of the most widely used techniques. It is particularly suited for non-destructive testing in laboratories as well as industrial environments. It is originally a modified structural form of the closed waveguide technique, where one end is physically removed to attain an electric open circuit condition, as depicted in Figs.1.5a and 1.5b. Stuchly and Gajda are attributed as the pioneers of this one-port measurement technique [Stuchly et al., 1980; Gajda and Stuchly, 1983; Gajda et al., 1983]. The complex permittivity of the material is evaluated from the magnitude and the phase of the reflected signal computed via the measured complex scattering coefficient, i.e. $\boldsymbol{S_{11}} = S_{11}e^{-j\theta}$, stated here

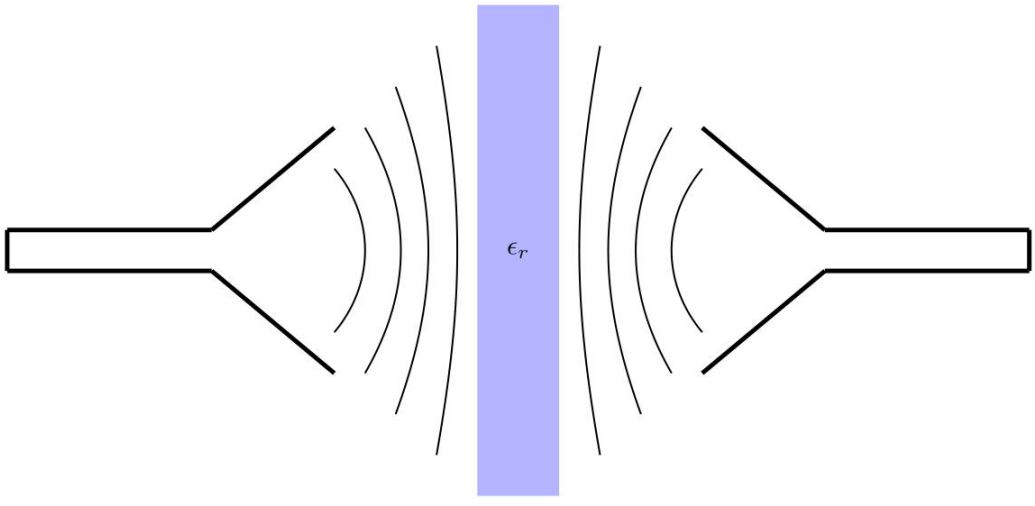


Figure 1.4: Example of Free-Space Setup

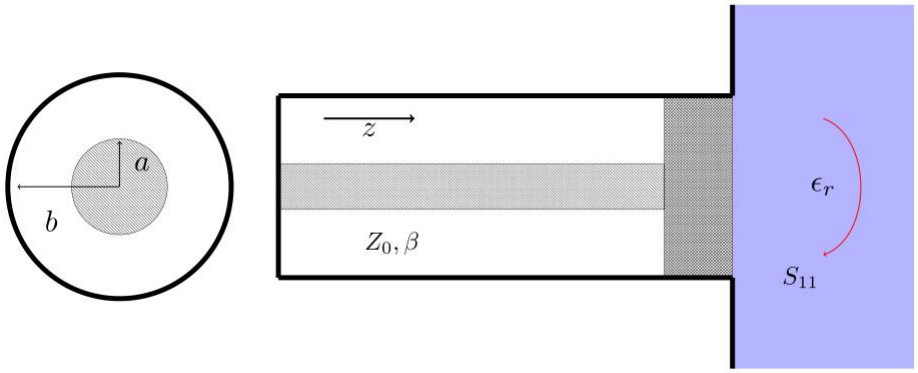


(a) Open-Ended Coaxial Probe

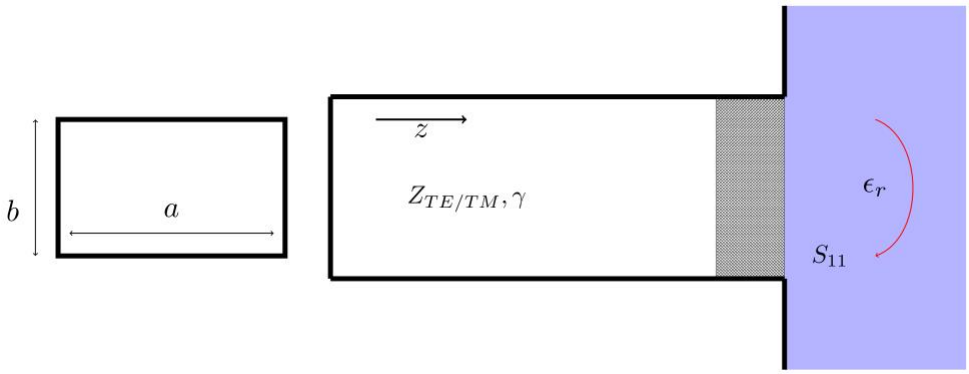


(b) Open-Ended Waveguide Probe

Figure 1.5: Open Cell Reflectometry

in polar form. The attained reflection coefficient is a function of the dimensions of the sensor, the frequency of operation, and the complex permittivity of the sample. Sample preparations in an open ended measurement have no specific requirement except for a flat surface condition in solid state bulk size samples. The open-ended waveguides are either immersed in liquid samples or directly flushed against the flat surface of solid samples.

The measurement fixture consists of both types of waveguides, i.e. the TEM coaxial waveguides and the TE/TM rectangular/circular hollow waveguides. Coaxial structures, more commonly called coaxial probes, are preferred due to the availability of larger operating bandwidths and relatively small dimensions at lower frequencies. Such probes are usually provided with flat and large circular flanges at the end to improve the approximation of infinite half space at the open end interface [Venkatesh and Raghavan, 2005]. Moreover, the probes are mostly equipped with low permittivity and low-loss dielectric inserts or beads at the sensing end to protect the inner portion of the probe from contamination due to the sample, particularly in a fluid state [Gregory and Clarke, 2006]. Coaxial probes are commercially available in varying outer dimensions, among which the most common are the 7 mm and 3.5 mm probes with operating ranges up to 18 GHz and 27 GHz, respectively. Open-ended hollow waveguides are also used as probes at higher frequencies, though the bandwidth of operation is limited due to the cut-off phenomenon at lower frequencies. Nevertheless, waveguide probes offer the advantage of providing better matching of the boundary conditions at the open end with test samples. Furthermore, rectangular waveguides are more feasible to perform test procedures in two different orthogonal directions of the sample orientation due to the presence of different linearly polarized modes. The property is useful in characterizing uniaxially anisotropic samples in parallel and perpendicular anisotropy axes [Baker-Jarvis et al., 2010].

The overall technique is well suited for measuring large permittivity values and higher loss

samples. The length or the thickness of the sample involved should be enough to absorb all the RF power within the sample and keep the radiation losses at minimal levels. In some arrangements, especially while measuring liquid samples, a termination or a back-short is provided at the end of the sample to create the short circuit [Gregory and Clarke, 2006]. Hollow waveguides in comparison to the coaxial probes exhibit better accuracy for relatively small permittivity values and low loss samples. Similar to the instance of guided methods, the air-gap problem persists at the interface between the sample and the open end of the probe. Parasitic effects and uncertainties in the measurement due to radiation losses tend to increase for higher permittivity values and low loss samples. The increased sensor size and frequency tend to cause the sensor to act as a self-radiating antenna, thus increasing the radiation losses. Moreover, larger sensors are also prone to resonances due to their proportionally large flange diameters.

### 1.2.2 Resonance Techniques

Resonance based microwave sensors involve the measurement of either a single frequency or multiple frequency points of discrete nature. Unlike propagating waves, the solution of Maxwell's equations yields standing waves in an enclosed and bounded structure. Alternatively, in terms of stored energy the oscillatory response is measured in the form of the resonance frequency $f_0$ and the 3 dB bandwidth of the resonance curve called the damping factor or inversely the quality factor, $Q_0 = \frac{f_0}{\Delta f_{3\,\mathrm{dB}}}$. Resonance frequency and quality factor parameters mainly specify the characteristics of a resonance condition. In the presence of a dielectric sample inside a resonator, the complex permittivity of the test sample can be directly derived from the overall change in the resonance frequency and the decrease of the quality factor.

Resonance methods are classified into two main groups of predominantly filled and perturbed cavity resonators. The distinction between these two groups is primarily based on the fractional volume of the sample introduced into the cavity and the distribution ratio of the stored electromagnetic energy between the sample and the cavity. The term filled resonance is used when either the sample occupies almost the complete volume of an empty cavity, or equally a bulk piece of a sample itself acts as a dielectric resonator shielded inside a conducting cage. On the other hand, perturbed cavity configurations have only a small volumetric fraction of the sample introduced at the location of the stored electric energy inside the cavity. Typically 90% of the resonating electromagnetic energy is stored inside the dielectric sample in filled resonance schemes, whereas mostly up to a proportion of 10% stored energy resides inside the sample in perturbation methods. The complex relative permittivity of the sample can then be directly extracted from the knowledge of the deviations in the resonance parameters. The real component of the permittivity is approximately proportional to the shift in frequency. Similarly, the loss tangent is evaluated from the damping measurement of the resonance curve. The validity of the approximation in the proportionality relation holds accurate for low to medium loss samples, i.e. $0.005 \leq \tan\delta \leq 0.1$ [Baker-Jarvis et al., 1998]. A general translation formula to extract the complex permittivity for the filled case is stated as [Venkatesh and Raghavan, 2005]

$$\epsilon' = \Big(\frac{f_0}{f_s}\Big)^2, \tag{1.18a}$$

$$\epsilon'' = \Big(\frac{1}{Q_s} - \frac{1}{Q_0}\sqrt{\frac{f_s}{f_0}}\Big)\epsilon', \tag{1.18b}$$

where

- $f_0$ resonance frequency before the sample filling or simply the reference resonance.
- $f_s$ resonance frequency after the sample filling.

- $Q_0$ quality factor before filling with sample.
- $Q_s$ quality frequency after the sample filling.

Similarly, in the perturbation technique only a small shift in the resonance frequency $\Delta f$, and a differential change in the quality factor $\Delta Q$ occur as a result of the sample insertion. The approximate relation between the complex permittivity of the sample and the shift in resonance parameters can be derived from the perturbation theory as [Kanpan et al., 2012]

$$\epsilon' = 2C\Big(\frac{\Delta f}{f_0}\Big)\Big(\frac{V_c}{V_s}\Big) + 1, \tag{1.19a}$$

$$\epsilon'' = C_p\Big(\frac{1}{\Delta Q}\Big)\Big(\frac{V_c}{V_s}\Big), \tag{1.19b}$$

where

- $\Delta f = \dfrac{f_s - f_0}{f_0}$ fractional difference in frequency due to the sample.
- $\dfrac{1}{\Delta Q} = \dfrac{1}{Q_s} - \dfrac{1}{Q_0}$ fractional change in quality factor.
- $V_c$ and $V_s$ are the volume of the cavity and sample, respectively.
- $C_p$ is the constant called the cavity shape factor that depends on the modal field distribution of the specific resonance mode.

Resonance methods offer the advantage of highest possible measurement accuracy and increased sensitivity for the purpose of material characterization. Both one-port and two-port configurations are employed depending on the material losses and measurement requirements. For loss characterization of materials in standalone resonating systems, the strength of external coupling has to be different in both configurations. Stronger coupling is established for one-port networks, whereas to avoid external loading effects weaker coupling is preferred for two-port networks [Bethe and Verweel, 1969].

#### 1.2.2.1 Filled Cavity Methods

Filled or dielectric resonance methods are usually workable for large sized samples, as the stored electromagnetic energy mainly resides inside the sample. The large volume or mass of the sample implies that the technique is fitting for large permittivity and low loss samples. Otherwise, the energy dissipation within higher loss samples causes the flatness of the resonance curve. Dielectric cavity methods of the sample can be realized in a number of configurations depending on the metal shield arrangement [Sheen, 2009]. Two widely known subcategories are the cylindrical TE mode based post resonance technique and the dielectric cavity technique.

**Post Resonance:**

Post or dielectric rod resonance methods are characterized by a sample in the form of a cylindrical dielectric rod placed axially in between two parallel metal plates, as depicted in Fig.1.6a. The parallel plate arrangement of the metal walls at top and bottom ensures confinement of the electromagnetic energy. The dielectric post between the plates is made to resonate in the $TE_{011}$ resonance mode, which is fed via an appropriate coupling probe arrangement from the sides [Krupka, 2006]. In order to extract the dielectric loss tangent, the accurate value of the surface resistance of the metal plates at the resonance frequency is required. It is achieved by performing measurements at two or more resonance frequencies with different $TE_{01n}$ modes [Gregory and Clarke, 2006]. The overall configuration of the post resonance method is rather simple with easy access for the placement and the removal of samples. In addition, the aspect ratio of the dielectric rod, i.e. diameter/height is a critical factor in minimizing the radiation losses.

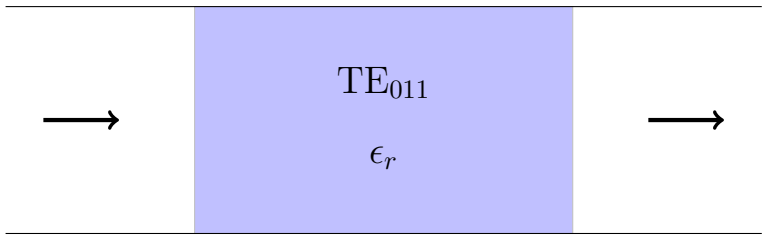


(a) Post Resonance: $TE_{011}$ mode

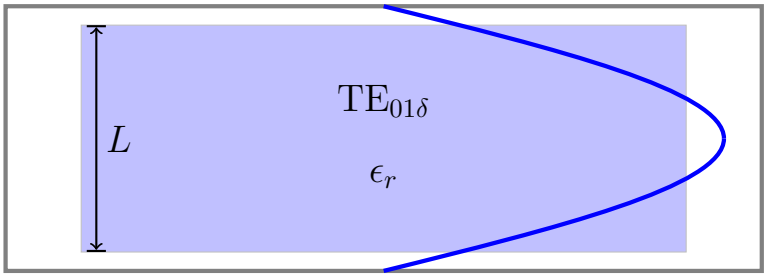


(b) Dielectric Resonance: $TE_{01\delta}$ mode

Figure 1.6: Filled Cavity Examples

The method provides reliable evaluation of the real permittivity, though the loss measurement is restricted due to the above mentioned critical issue of the surface resistance of the metal walls. Moreover, the setup belongs to the category of calculable geometries implying that there are well developed equations for the evaluation of the complex permittivity [Sheen, 2009].

**Dielectric Resonance:**
The method comprises a dielectric sample in the shape of a cylindrical disc enclosed inside a shielded metal case. Such electrically isolated disc samples are usually supported via some appropriate physical means and kept sufficiently away from the metal shield boundaries. The predominant resonance mode in this case is similar to the $TE_{011}$ mode, called the $TE_{01\delta}$ mode, where $\delta = 2L/\lambda_g < 1$ represents the longitudinal variation of the resonance mode in terms of the guide wavelength $\lambda_g$, as shown in Fig.1.6b. The resonance mode is established within the dielectric whereas it is evanescent outside in the air region around the dielectric. The absence of conductive paths between the dielectric and the metal walls overcomes the sheet resistance problem of the post resonance approach. The lack of the surface resistance makes this type of resonance ideal for characterizing loss tangents of various materials. Therefore, it is a widely used scheme for loss characterization of ceramics [Sheen, 2009]. However, due to the lack of any closed form solution the computation is rather complicated for real permittivities. In addition, while employing this technique care must be taken to avoid the coupling of undesired modes, formed within the metal shield, to the dielectric resonance mode.

#### 1.2.2.2 Perturbation Methods

Perturbation methods require a small piece of a sample inserted into a cavity resonating at either a single frequency or multiple resonance modes. Due to the significantly smaller volume of the test samples, the perturbation method can be employed for moderate to high loss samples, i.e. $0.005 \leq \tan\delta \leq 0.1$ [Baker-Jarvis et al., 1998]. Not only solid but liquid samples can also be characterized using low-loss sample holders like polyfoam or thin capillary tubes made from glass or quartz [Gregory and Clarke, 2006]. The perturbation technique can be realized in various types of cavity geometries that include split-cylindrical cavities, re-entrant cavities, the $TE_{01n}$ and $TM_{0n0}$ modes in cylindrical cavities, as well as the $TE_{10n}$ mode rectangular cavity resonators. The types of realization among the perturbation methods are essentially governed by the shape and dimensions of the sample. Another consideration is the ease of accessibility

of the sample regarding interaction with the cavity.

**$TE_{01n}$ modes:**
The $TE_{01n}$ based cavities are characterized by an axially symmetric circumferential electric field with a very high quality factor of 15 000 - 30 000 depending on the frequency of operation. It is practically realizable in the form of cylindrical geometries typically in the frequency range of 8 GHz − 40 GHz [Martinelli et al., 1985]. Dielectric samples with optimum thickness of a half wavelength and radius equal to that of the cavity are inserted at one end of the cavity. The circumferential electric field is tangential at the air-dielectric interface of the sample which leads to negligible influence of the air-gap problem. Additionally, due to the presence of circumferential currents and lack of the radial current components at the lateral surfaces of the cavity, the contact between cylindrical walls and lids is not critical. This property leads to the ability of the $TE_{01n}$ based cavities to be made tunable by moving the lateral surface using an appropriate plunger mechanism [Horner et al., 1946]. The overall geometry along with the dielectric disc-shaped sample is considered calculable with an exact solution available for the computation of the complex permittivity. The higher quality factor of the $TE_{01n}$ made it an ideal candidate for measuring loss factors in materials. For instance, in industrial processes it is employed to determine the moisture content in cotton yarn and wool fibres [Kumar and Smith, 1977; Meyer and Schilz, 1981].

**$TE_{10n}$ modes:**
The $TE_{10n}$ modes are characterized by an integer multiple of half wavelength variations of the linearly polarized electric field in the transverse plane along the width $a$ of a rectangular cavity. The subscript $n$ indicates the number of half wavelength resonances along the length of the rectangular cavity section. The sample to be tested is placed along the E-plane midway in the longitudinal dimension. The typical frequency range for the $TE_{10n}$ operation lies in the X-band (8 GHz − 12 GHz), though in some instances lower frequency measurements down to 2 GHz are also performed. The achievable quality factor for the $TE_{10n}$ modes is around 4000 - 10 000. The rectangular cavity methods are usually employed with $n$ multiple half wavelengths $TE_{10n}$ modes in order to characterize the sample at different frequencies, as demonstrated in a number of publications [Verma and Dube, 2005; Santra and Limaye, 2005; Sheen and Weng, 2016]. Odd multiples of the $TE_{10n}$ mode have the peak electric field midway along the width, whereas the even modes have the peak magnetic field. In a number of techniques, the $TE_{10n}$ family of modes have been employed to perform permittivity and conductivity measurements on dielectric and semiconductor samples. For semiconductor samples the dielectric losses are replaced by the conductivity term, i.e. $\sigma = \sigma_0/\omega\epsilon_0$, so the complex permittivity can be stated for conductive materials as, $\epsilon = \epsilon' - j\sigma$ [Chao, 1985]. The $TE_{10n}$ based cavities due to geometric similarity also offer a viable choice for evaluating thin long laminated samples, such as FR-4 epoxy glass substrate or other PCB-film materials [Thomas and Dube, 1997]. In addition to the standard waveguide structures employing $TE_{10n}$ modes some recent work has showed significance of utilizing double-ridged waveguide type applicators for material characterization [Kik, 2016].

**Re-entrant and $TM_{0n0}$ cavities:**
A re-entrant cavity is fundamentally a closed section of an approximately quarter wavelength long coaxial line, which is shorted at the bottom end but provided with a gap between the inner conductor and the top wall surface. The length of the inner conductor is slightly more than one-eights of the wavelength but less than a quarter wavelength of the operating resonance frequency. The gap region serves as the high electric field region, that creates an additional parallel capacitance due to the strong electric field in the gap region of the cavity. The material to be tested is usually placed in the gap volume with radial dimensions smaller than the inner conductor, as depicted in Fig.1.7a. A dielectric sample in the presence of the electric field effects the overall capacitance, consequently causing a proportional shift in the resonance frequency and the quality factor. Reentrant cavities are employed in the frequency range of typically 50 MHz − 2 GHz [Baker-Jarvis et al., 1998]. Reentrant cavities are usually made tunable by providing

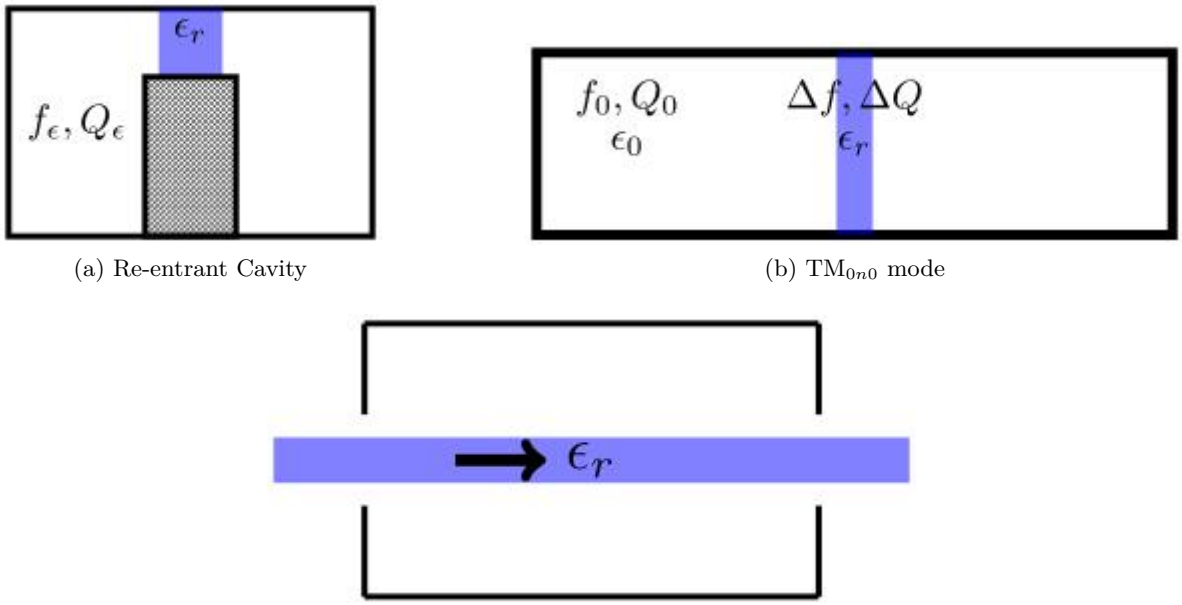


(a) Re-entrant Cavity

(b) $TM_{0n0}$ mode

(c) Split Cavity

Figure 1.7: Perturbation Techniques

tuning screws at the cavity head adding more flexibility to the design tolerances in dimensions.

Another family of resonance modes in cylindrical cavities termed as $TM_{0n0}$ also have an axial electric field component supported by a circumferential magnetic field around the periphery walls. As shown in Fig.1.7b, the field distribution inside a $TM_{0n0}$ based cavity is mostly suited for a concentric cylindrical rod shaped sample [Bethe and Verweel, 1969], nonetheless disc and other sample shapes are also utilized. Due to the presence of longitudinal currents on the circular boundaries and radial currents on the horizontal surface, the disassembly of the cavity is not a recommended procedure. The means for inserting a sample are usually provided by creating small insertion holes in the center of the top and/or bottom lids. In practice, thin samples with shapes conforming to the cylindrical cavity are longitudinally placed along the whole length of the resonator. Those samples which are either partially inserted or do not occupy the complete length of the cavity are required to be accounted for the depolarization effect [Parkash et al., 1979], which is a function of the shape of the sample and the field orientation at its boundary surfaces. In some instances, higher oder modes ($n = 2, 3, 4...$) are also utilized in order to have multiple measurement points [Kanpan et al., 2012]. The TM based cavities are also employed for the measurement of the conductivity [Wang et al., 1991]. $TM_{0n0}$ mode based cavities have relatively low quality factor typically between $2000 - 8000$, which results in limited loss characterization. Still the family of modes are a useful choice for the measurement of the real permittivity of long thin cylindrical samples.

In both types of cavity operation the air gap region between metal surfaces and sample causes significant computational errors in the complex permittivity evaluation. The air gap has a similar influence as stated for the guided wave structures causing additional capacitance usually due to the fringing effects of the electric field. The issue is more prominent for lower permittivity dielectric material with normal electric field at the air-dielectric interface.

Other resonance methods include split cavity resonators and open resonators. A split cavity as displayed in Fig.1.7c is useful for characterizing the thickness in material streams, particularly for determining different values of metal thickness [Hamid and Mostowy, 1974]. Split cavity resonators can be employed in any suitable mode, whether $TE_{01n}$ or $TM_{0n0}$, depending on the geometry of the cavity itself [Janezic and Baker-Jarvis, 1999; Janezic et al., 2004].

## 1.3 Motivation of the Work

A wide range of conventional methods in different categories with their operating principles and relevant applications have been discussed in the previous section. Nevertheless, in a variety of instances there are often requirements for custom modifications and extensions of the standard methods to address the nature of a specific problem. Following is a background discussion of some examples where modifications to standard techniques are carried out. Usually such modifications are aimed to extend the fundamental method to either perform differential measurements between two distinct parameters, or isolate and suppress undesired effects from a single parameter.

### 1.3.1 Modified Measurements

A simple example to illustrate the importance of differential measurements comprises a two-cavity scheme to measure the contamination in gases as continuous and differential output, based on the measurement and comparison to the reference simultaneously [Rouleau et al., 2001]. The setup consists of a 180° hybrid junction of two cavities, where one cavity detects the contamination while the other serves as a reference signal. The difference in the impedance between the two cavities because of the exposure to contamination results in a detectable threshold signal.

In another scheme realized as microstrip lines [Ocera et al., 2006], a four-port configuration was employed to detect the differential signal. The system comprised two 3 dB directional couplers connected to a pair of oppositely fabricated U-shaped microstrip sections having identical lengths. A teflon sample was placed as a superstate over one of the sections causing a change in the effective electrical length of the line, hence resulting in difference of the outputs between each pair of the two-ports.

Another planar transmission technique employed a pair of open-ended and out of phase coupled lines, which are covered by the dielectric under test [Piekarz et al., 2016b,a]. The measurement scheme is essentially a one-port configuration with an integrated Marchand balun to perform balance to unbalance impedance transformation. It has the advantage of short time analysis and high sensitivity for very thin materials placed between the coupled lines in contrast to some other comparable techniques [Narayanan, 2014; Shete et al., 2013]. When a sample is placed in between the coupled lines the odd mode gets strongly influenced, whereas the even mode capacitance exhibits negligible response.

A further example of an increased sensitivity measurement setup formed by a pair of identical waveguides connected through a narrow aperture at the junction of a 180° bend. The connecting junction is provided with metal wires or strips covering the dielectric specimen under test [Siddiqui and Ramahi, 2011]. The configuration results in two types of resonances that include the lowest order Fabry-Perot resonance and the wire resonance. The wire resonances which are sensitive to the wire length produce a response to slight changes in the permittivity of the thin film dielectric sample surrounding the wire. The aim of the technique is to characterize changes in the dielectric permittivity of materials, which are used as substrate for planar structures that include plexi-glass, FR-4 and Rogers materials. The metal strips over the dielectric were fabricated using etching before being placed inside the waveguide bend portion.

### 1.3.2 Background of the Problem

The methods discussed above share some relevance with the techniques employed during the course of the presented research and development work. Practically, these discussed techniques are based on geometrical modifications and additional material loading of an otherwise standard $TM_{010}$ cavity equipped with relatively large size insertion holes. The major objective behind these modifications is either to extract more information regarding the sample state, or alterna-

tively to suppress the undesired influence of deformities which are the source of uncertainties in the final measurement. Specifically, the two approaches adapted in the presented work comprise a scheme of shaped dielectric inserts and an extended solution based on the arrangement of a pair of mutually coupled cylindrical cavities. Both adapted schemes are meant to extend the application of cylindrical cavities with large insertion holes either by improved field uniformity or by appending an additional degree of flexibility to the measurement setup. Particularly, the approach of coupled cavities yields another resonance mode closely associated with the primary mode but exhibiting a different orientation, which proves useful in extracting offset errors in the axial flow of the sample.

In practice, the measurement of additional parameters while employing a single sensing structure is a challenging task. However, there are examples where size-independent and shape-independent measurements of the permittivity related parameters are achieved by using a single resonance curve [Kraszewski and Nelson, 1991b,a, 1992, 1994]. The two parameters of the frequency shift and the change in quality factor are combined into a single factor in order to suppress the undesired common parameter. For example, a volume or mass independent function is reached when the measure of frequency shifts and quality factors are divided by each other. Similarly, in a number of techniques the sample characteristics are extracted from the resonance curves belonging to the same family of modes, such as $TM_{0n0}$ or $TM_{10n}$ [Santra and Limaye, 2005]. Although, due to similar field distributions of a same family of curves, the additional information is rather redundant in nature. On the other hand, another practical approach for measuring multiple parameters is to utilize two independent sets of modes for the same sample as presented in the work of [Lakshminarayana et al., 1979; Meyer, 1977]. Two independent modes means two separate resonance curves which obviously yield more information about the sample. Another variant of this approach is to rather use two different orientations of the same sample for a single sensing cavity [Lakshminarayana et al., 1979]. In such cases, the interaction of tangential and normal electric fields at the sample interface cause a different polarization. The latter technique requires two separate resonators to perform simultaneous measurement with two non-identical electric field orientations, i.e. parallel and perpendicular polarizations. However, in resonance structures neighboring modes are dependent on the cavity geometry and are not largely tunable, which limits the flexibility of the design scheme of two or more cavities.

### 1.3.3 Computational Tool

In principle, electromagnetic problems are computed by solving Maxwell's equations. An exact solution of the equations for any electromagnetic problem also requires the knowledge of the associated boundary conditions. The boundary conditions allow for matching the solutions at interfaces of different media involved. While employing a microwave sensor for material characterization usually a mathematical model based on the solution is developed. The model connects the response of the sensing system to the permittivity characteristics of the material. As mentioned earlier, there exist only few cases of exact mathematical relations between the response of a microwave sensor and the properties of a material under test. Such cases of calculable geometries are generally confined to strictly simple structures of sensors and samples. For example, a thin long needle shaped dielectric sample placed at the center and along the whole length of a completely closed cylindrical cavity is one instance where a nearly exact solution can be obtained. When the sensing structure contains deformities which largely disturb the original field distributions, then the problem requires an approximate analysis based on some appropriate numerical technique. The idea behind using numerical approximations is to minimize the influence of non-ideal effects, either by computational adjustments of the design aspects or by appending error compensation terms in the original model. In the context of analyzing electromagnetic problems and implementing structural adjustments to the design, the use of 3D electromagnetic solvers has significant importance and utility. Such solver tools are usually equipped with a Graphical User Interface (GUI) to model the problem and later

compute solutions based on a variety of computational algorithms fitting the nature of the problem.

CST Microwave Studio (MWS) is one such well-known 3D electromagnetic solver with the computation schemes based on a number of algorithms that are utilized by different solvers available in the computational tool. These algorithms include the Finite Integration Technique (FIT), the Transmission Line Method (TLM), the Method of Moments (MoM) and the Finite Element Method (FEM). In addition, the two major meshing schemes are available in the CST tool to discretize the problem space into smaller elements, namely, the hexahedral mesh or the tetrahedral mesh. Furthermore, for objects that can be reduced to only boundaries there is an option of surface meshing available [Computer Simulation Technology, 2017].

The solver modules available in CST mainly comprise the Time Domain, the Frequency Domain, the Eigenmode and the Integral Equation solvers. The time domain or transient solver calculates the development of the field through time at discrete locations and at discrete time samples, based on the FIT and the TLM algorithms with hexahedral meshing. Time domain solvers are applicable to high frequency problems that include connectors, transmission lines, filters, antennas etc., to obtain the entire broadband frequency behaviour of the simulated device from a single calculation run. The frequency domain solver works with time harmonic dependence of the fields and excitations, so the process carries out frequency by frequency simulation to yield S-parameter results of structures. Since each frequency sample requires a new equation system to be set up and solved, the relationship between calculation time and frequency samples is linear. The integral equation solver is well suited for electrically large models. The discretization of the calculation area is reduced to the object boundaries and thus leads to a linear equation system with lesser unknowns than volume methods. For calculation efficiency the equation system can be solved by the Multi Level Fast Multipole Method (MLFMM) for electrically large models. The eigenmode solver utility calculates the frequencies and the corresponding electromagnetic field patterns of loss-less structures when no excitation is applied. The eigenmode solver works with both hexahedral and tetrahedral meshing schemes. The eigenmode solver is an efficient tool to calculate field distributions of the resonance modes inside closed cavities.

The Eigenmode Solver and the the Frequency-Domain Solver provided in CST Microwave Studio are frequently utilized in the course of the presented work. The field distributions and behaviour of the resonance modes under geometrical modifications of the structure are determined from the Eigenmode Solver. The utility of the Frequency-Domain Solver is mostly employed to systematically simulate the influence and dependence of the sample offset from the axial center on the shift or deviation in resonance frequency parameters. Consequently, the shaped dielectric insert solution and the coupled cavities solutions are also validated by producing prototypes based on the simulation results.

# 2 Cylindrical Cavity Sensor: Analysis and Computation

The chapter presents the full-wave analysis of a dielectric-loaded cylindrical waveguide in transverse magnetic mode, since analysing such a structure is fundamental to the application of material sensing in circular cavities. The wave propagation results are then extended to the standing wave solution which is limited to the case of transverse magnetic field distributions to arrive at the $TM_{010}$ mode cavity results with concentric dielectric loading. In addition, the perturbation method and the relevant set of approximations are also discussed for the sake of comparison with the full-wave approach. The mathematical analyses are followed by an account of major sources of deviations from the ideal assumptions undertaken in the full-wave and the perturbation analysis. The effects of one of the most significant sources of deviation, i.e. the insertion holes for samples placement or flow, are discussed in a separate section. The main objective of using such a presentation approach is to emphasize the differences in theory and practice which occur while implementing the cylindrical cavity as a sensor. Therefore, the later sections entail the description of an implementation problem that frequently occurs while realizing cylindrical cavity resonators to measure variations in thickness or mass of dielectric samples. Such problem types which are fundamentally concerned with mass measurements demand different criteria in design specifications of the applied sensor when compared to general permittivity measurement tasks. Hence, the accuracy in the measured value of the dielectric permittivity of the sample is not the primary concern, instead the emphasis is laid on the spatial distribution of the field quantity which interacts with the sample. More specifically, in such sensor implementations a uniform and homogeneous electric field is required in order to sense true changes in the sample mass. The significance of the problem is highlighted with the help of a relevant example of an industrial implementation. Following the problem description, the primary sensor design as well as computational details of the initial prototype are presented. The basic cavity sensor is actually a pill-box $TM_{010}$ cavity resonator operating within one of the ISM bands, i.e. 2.40 GHz-2.50 GHz, with provisions for sample insertion holes on the top and bottom walls. A computational study on the effects of the deformities caused by insertion holes in the basic pill-box design is presented in the ending section. The adverse effects of insertion holes on frequency shift measurements in the presence of dielectric samples are validated through numerical and computational analyses, which are carried out by using the Frequency Domain Solver in CST-Microwave Studio.

## 2.1 Full Wave Analysis

The electromagnetic field in cylindrical coordinates $(r, \phi, z)$ for circular guided structures is usually expressed in terms of two scalar potential wave functions, $\psi_e(r, \phi, z)$ and $\psi_m(r, \phi, z)$, which are the $z$-components of the electric and the magnetic vector potentials, respectively. The electric potential $\psi_e$ generates field solutions of purely transverse electric nature ($E_z = 0$), which are called transverse electric (TE) modes. Similarly, the magnetic potential $\psi_m$ solves for purely transverse components of the magnetic field ($H_z = 0$), known as transverse magnetic (TM) modes. In addition to the TE and the TM-mode propagation, the linear combination of the two orthogonal modes yields hybrid modes, denoted by the HE symbol. The hybrid modes are characterized by the simultaneous presence of non-zero axial electric and magnetic field

components. For purely $\mathrm{TM}_{nm}$ mode propagation in an axially uniform perfectly conducting metal cylinder, the reduced Helmholtz equation for the magnetic potential, i.e. $\psi_m(r,\phi,z)$, is stated as [Balanis, 2012]

$$\nabla^2\psi_m(r,\phi,z) + \beta^2\psi_m(r,\phi,z) = 0, \tag{2.1}$$

where

- $\nabla^2$ is the second order differential operator for the transverse cylindrical coordinates $(r,\phi,z)$,

$$\nabla^2 = \frac{\partial^2}{\partial^2 r} + \frac{1}{r}\frac{\partial}{\partial r} + \frac{1}{r^2}\frac{\partial^2}{\partial^2\phi} + \frac{\partial^2}{\partial^2 z}.$$

- $\beta$ is the imaginary component of the propagation coefficient derived from the definition of the complex propagation coefficient, $\gamma = \alpha + j\beta$. In view of uniform plane waves, $\beta$ is equal to the real part of the wave number $k = k' - jk''$ for loss-free dielectric filling inside the cylindrical waveguide, i.e. $\beta = k$.

In Eq.(2.1) $\psi_m(r,\phi,z) = \psi_m(r,\phi)e^{-j\beta z}$ can be assumed to establish absolute uniformity in the positive z-direction with no longitudinal variations. The assumption can be replaced in Eq.(2.1) to yield

$$\left(\frac{\partial^2}{\partial^2 r} + \frac{1}{r}\frac{\partial}{\partial r} + \frac{1}{r^2}\frac{\partial^2}{\partial^2\phi}\right)\psi_m(r,\phi) + \left(\beta^2 - \beta_z^2\right)\psi_m(r,\phi) = 0. \tag{2.2}$$

In the above equation $\beta_z$ is the longitudinal propagation coefficient in the guiding circular structure which is expressed through the relation

$$\beta_z^2 = \beta^2 - \beta_c^2, \tag{2.3}$$

with

- $\beta = \omega\sqrt{\mu_0\epsilon_0\epsilon_r} = k_0\sqrt{\epsilon_r}$ as the frequency dependent propagation coefficient of the medium inside the waveguide, which is equal to the free-space wavenumber $k_0$ of a uniform plane wave for purely air-filled waveguides ($\epsilon_r \approx 1$).

- $\beta_c = \beta_r = p_{nm}/b$ as the propagation cut-off for the transverse dimensions, which depends only on the radial variable due to the periodic nature of $\phi$ given by the $n$-index being treated as a constant. In bounded structures, the cut-off is defined by the discrete number of infinite $p_{nm}$ roots of the Bessel function for any given cylindrical radius $b$.

In order to obtain a general solutions of Eq.(2.2) in terms of the transverse dimensions $(r,\phi)$ the method of separation of variables is applied [Collin, 2001],

$$\psi^m(r,\phi) = \mathrm{R}(r)\mathrm{P}(\phi), \tag{2.4}$$

where

- $\mathrm{R}(r) = A\mathrm{J}_i(\beta_c r) + B\mathrm{N}_i(\beta_c r)$, represents the solution for radial variations as the sum of $i^{\text{th}}$-order cylindrical Bessel functions of first and second kind, respectively. The $\mathrm{N}_n(\beta_c r)$ term for homogeneously filled waveguides can be omitted from the solution by setting the coefficient $B = 0$, as the term yields a physically unrealistic value of $\mathrm{N}_n(0) = \infty$ for the argument $r = 0$.

- $\mathrm{P}(\phi) = C\cos(n\phi) + D\sin(n\phi)$, represents $n$-circumferential variations of the trigonometric functions, which are treated as integer multiples due to the periodic nature of the solution in the $rz$-plane.

Eventually, the complete wave solution for the guided propagation can be obtained by computing the constants and the cut-off wavenumbers under the boundary conditions of perfect conductor ($\sigma = \infty$) at $r = b$, given by $\psi = 0$ and $\partial\psi/\partial n = 0$ [Harrington, 2001]. The required electric and magnetic fields are obtained through direct differentiation of the scalar wave functions for the corresponding mode distribution. For example, the scalar wave function for the $TM_{0m}$ mode characterized by no circumferential but only radial variation is stated as [Harrington, 2001]

$$\psi^m = A_{01}\mathrm{J}_0(\frac{p_{0m}}{b})e^{-j\beta z}, \tag{2.5}$$

where $A_{01}$ is the constant dependent on the boundary conditions and the excitation levels of the energy, whereas $p_{0m}$ are the roots of the Bessel function. The fundamental transverse mode $TM_{01}$ has the root value of $p_{01} = 2.4048$. The non-zero electric and the magnetic field components for the dominant $TM_{0m}$ modes in an axially uniform circular waveguide are differentiated from the scalar wave function using the relations [Harrington, 2001]

$$E_z = \frac{1}{j\omega\epsilon}(\frac{\partial^2}{\partial z^2} + \beta^2)\psi_m = A_1\mathrm{J}_0(\frac{p_{0m}}{b}), \tag{2.6a}$$

$$E_r = \frac{1}{j\omega\epsilon}\frac{\partial^2\psi_m}{\partial r\partial z} = -\frac{\beta}{\beta_r}A_1\mathrm{J}_1(\frac{p_{0m}}{b}), \tag{2.6b}$$

$$H_\phi = -\frac{\partial\psi_m}{\partial r} = -\frac{j\omega\epsilon_0}{\beta_r}A_1\mathrm{J}_1(\frac{p_{0m}}{b}), \tag{2.6c}$$

where $\beta_r = \dfrac{p_{0n}}{b}$ and the constant $A_1 = A_{01}\dfrac{\beta_r^2}{\omega\epsilon}$ is replaced into another convenient form.

### 2.1.1 Coaxially Loaded Dielectric in Cylindrical Hollow Waveguides

The general problem of a dielectric material with a certain permittivity value partly filling either the outer or the inner radius of a cylindrical waveguide structure is of two-fold interest. The solution of the problem has applications as linear accelerator for electron density measurement and as cavity resonator for material characterization. The treatment of the problem specific to the application of cavity resonators can be performed by analysing the coaxial type geometry of the waveguide with centrally loaded dielectric. Fig.2.1 shows the cylindrical waveguide geometry comprising the bounded and air-filled outer section ($\epsilon_r \approx 1$) with radius $b$. The inner section is a coaxially confined arbitrary dielectric material of radius $a$ with relative permittivity $\epsilon_r > 1$. The geometry of the problem requires the solution of the Helmholtz equation identical to Eq.(2.1), with additional boundary condition at $r = a$, i.e. the confined dielectric interface. Scalar potential functions $\psi_i^m$, similar to Eq.(2.5), as the solutions of the reduced Helmholtz equation for the dominant $TM_{01}$ mode in the inner and outer regions are stated as [Banos et al., 1951]

$$\psi_1^m = A_1\mathrm{J}_0(\beta_{r1}a)e^{-j\beta z}, \tag{2.7a}$$

$$\psi_2^m = A_2\{\mathrm{J}_0(\beta_{r2}r)\mathrm{N}_0(\beta_{r2}b) - \mathrm{N}_0(\beta_{r2}r)\mathrm{J}_0(\beta_{r2}b)\}e^{-j\beta z}, \tag{2.7b}$$

where the subscript $i = 1, 2$, represents the inner and outer regions, respectively. Furthermore, the expression of the Bessel function of the second kind $\mathrm{N}_0(\beta_{r2}r)$ remains valid for the outer ring region due to the absence of the $r = 0$ argument value. Propagation exists only if the frequency dependent propagation coefficients $\beta_i$ of the two adjoining media, i.e. $i = 1$ and $i = 2$, are greater than their respective propagation cutt-offs $\beta_{ri}$. Moreover, the propagation also requires the longitudinal propagation coefficient $\beta_z$ to be matched at the dielectric interface, i.e. identical $\beta$ for both regions, as there exists no variation along the $z$-direction in both regions.

The overall relation between the wavenumbers for centrally loaded waveguide structures with axial uniformity for each region 1 and 2 can be separately stated as [Banos et al., 1951]

$$\beta_{r1}^2 = \beta_1^2 - \beta_z^2 = \omega^2\mu_0\epsilon_0\epsilon_r - \beta^2, \tag{2.8a}$$
$$\beta_{r2}^2 = \beta_2^2 - \beta_z^2 = \omega^2\mu_0\epsilon_0 - \beta^2, \tag{2.8b}$$

respectively. Due to the equality of the longitudinal propagation coefficeint $\beta_z$, both Eqs.(2.8) can be combined into a single equation to establish the relation between the cut-off dependent propagation coefficient on the frequency and the dielectric permittivity of the inner filling. The other equation is obtained by solving for the electric and magnetic fields of the $\mathrm{TM}_{01}$ mode for each region using the corresponding scalar functions of Eq.(2.7a) and Eq.(2.7b) for each region. The variables $A_1$ and $A_2$ in Eq.(2.6a) are then eliminated by applying the boundary condition for the continuity of the tangential fields of $E_z$ and $H_\phi$ at the dielectric interface $r = a$, as well as at the perfect electric boundary of $r = b$. The final outcome of the mathematical operations yields a transcendental equation, which is either solved graphically or numerically [Banos et al., 1951],

$$\frac{\beta_{r1}\mathrm{J}_0(\beta_{r1}a)}{\beta_1^2\mathrm{J}_1(\beta_{r1}a)} = \frac{\beta_{r2}[\mathrm{J}_0(\beta_{r2}a)\mathrm{N}_0(\beta_{r2}b) - \mathrm{N}_0(\beta_{r2}a)\mathrm{J}_0(\beta_{r2}b)]}{\beta_2^2[\mathrm{J}_1(\beta_{r2}a)\mathrm{N}_0(\beta_{r2}b) - \mathrm{N}_1(\beta_{r2}a)\mathrm{J}_0(\beta_{r2}b)]}. \tag{2.9}$$

The graphical solution was presented by Banos [Banos et al., 1951], where identifying the two dimensionless variables of $u$ and $v$ gives the relations

$$u = \beta_{r1}a, \tag{2.10}$$
$$v = \beta_{r2}a. \tag{2.11}$$

Furthermore, by using the ratio of both dielectric permittivity values, i.e. $\kappa = \epsilon_1/\epsilon_2 = \epsilon_r$, and radial dimensions, i.e. $\eta = b/a$, between both sections, Eq.(2.9) can be graphically solved by plotting the $F(u^2, \kappa)$ and $G(v^2, \eta)$ functions [Banos et al., 1951],

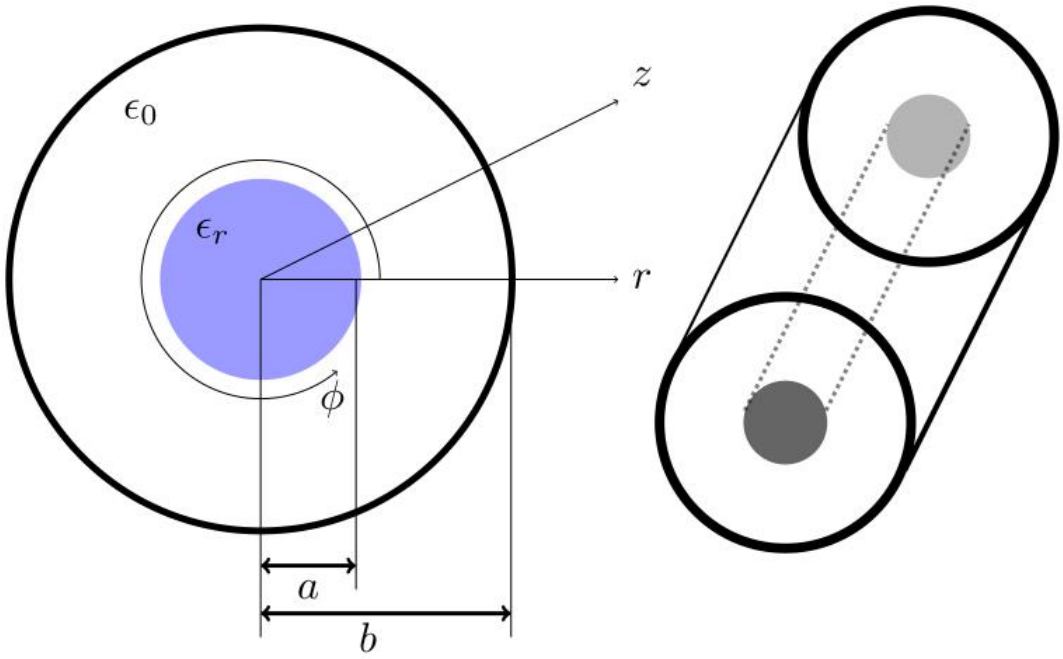


Figure 2.1: Centrally Loaded Circular Waveguide

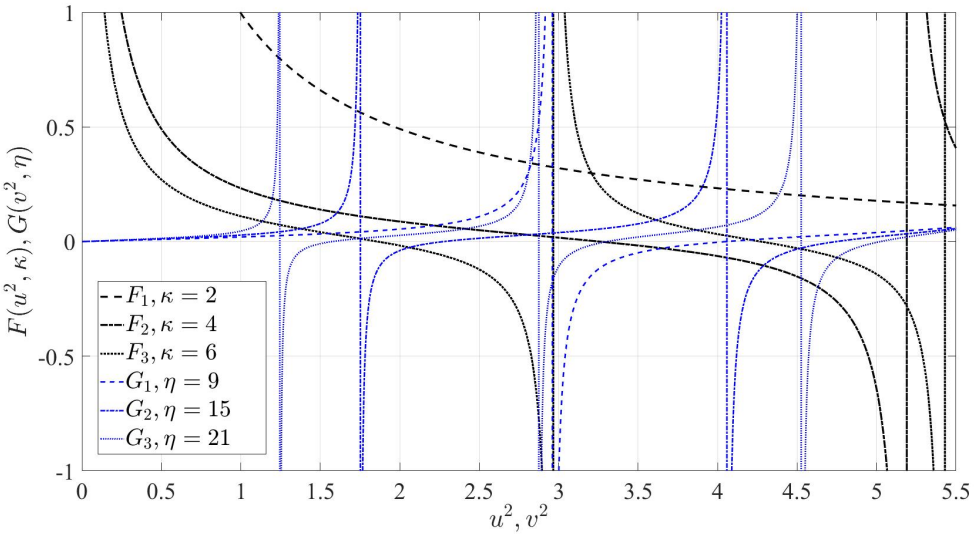


Figure 2.2: Graphical Solution of the Transcendental Equations

$$F(u^2,\kappa) = \frac{u\mathrm{J}_0(u)}{\kappa\mathrm{J}_1(u)}, \tag{2.12a}$$

$$G(v^2,\eta) = v\frac{\mathrm{J}_0(v)\mathrm{N}_0(\eta v) - \mathrm{N}_0(v)\mathrm{J}_0(\eta v)}{\mathrm{J}_1(v)\mathrm{N}_0(\eta v) - \mathrm{N}_1(v)\mathrm{J}_0(\eta v)}, \tag{2.12b}$$

against the combined $u^2, v^2$ axis. Eventually, a graphical solution, as depicted in Fig.2.2, for a centrally loaded cylindrical waveguide is obtained that is applicable to varying ratios of radial filling $\eta$ and dielectric permittivity $\kappa$ between concentric regions of 1 and 2. It is to be noted that for $\mathrm{TM}_{010}$ material measurement applications the radial ratio between the outer and the inner filling is usually a large number, i.e. $\eta >> 1$ and also $\kappa > 1$ is a valid proposition.
Regarding the material characterization application while employing cylindrical waveguides in the $\mathrm{TM}_{01}$ operating mode, there are some important observations, which can be deduced from the full wave analysis. Based on the graphical results of Eq.(2.9) the field distribution was computed in the inner filling with a large permittivity of $\epsilon_r = 100$ and $\eta = 3$ by Banos [Banos et al., 1951]. The plots of the field distribution reveal that inside the dielectric filling there exists a weak radial component of electric field $E_r$ with $\mathrm{J}_1(u)$ Bessel function dependence for the $\mathrm{TM}_{01}$ guided mode.

### 2.1.2 Empty $\mathrm{TM}_{010}$ Cavity

The $\mathrm{TM}_{010}$ mode is the characteristic or the fundamental operating mode inside a cylindrical cavity resonator with both axial ends closed. There is no axial variation of the inner resonating fields ($\beta_z = 0$), provided that the length of the cavity $d$ is less than the diameter $2b$ of the cavity, i.e. $d/b < 2$ [Pozar, 2011]. The longitudinal electric field $E_z$ and the circumferential magnetic field $H_\phi$, which are $90\,^\circ$ out-of-phase in time, are directly evaluated from the standing wave solution of the scalar potential function. The $E_z$ and the $H_\phi$ fields are derived in the form of a Bessel function for an air-filled cavity (ideally vacuum) from Eq.(2.6) with the condition that $\beta_r = \beta_c = p_{01}/b = \omega\sqrt{\epsilon_0\mu_0}$ from Eq.(2.3) [Horner et al., 1946],

$$E_z = \mathrm{J}_0(\beta_c r), \tag{2.13a}$$

$$H_\phi = j\sqrt{\frac{\epsilon_0}{\mu_0}}\mathrm{J}_1(\beta_c r), \tag{2.13b}$$

respectively. The resonance frequency of the $TM_{010}$ cavity mode can simply be obtained by applying the boundary condition for the tangential electric field $E_z = 0$ on the outer metal boundary plane at $r = b$ by setting $J_0(\beta_c b) = 0$. Using the root of the Bessel function, i.e. $p_{01} = \beta_r b = 2.4048$ and equating $\omega_0 = \beta_c c$, the relation for obtaining the resonance frequency for an empty cavity is given as [Carter, 2001]

$$f_0 = \frac{1.2024c}{\pi b}, \tag{2.14}$$

where $c \approxeq 3.0 \times 10^{-8}$ is the velocity of light in vacuum. From Eq.(2.14) it is evident that the resonance frequency is not a function of axial length. However, the quality factor of the $TM_{010}$ mode increases slightly in proportion to the axial length $d$. By definition the quality factor of a general cavity is expressed by the ratio of the total stored energy $W$ over the dissipated power $P_d$ over one frequency cycle [Pozar, 2011],

$$Q = \omega_0 \frac{W}{P_{loss}}, \tag{2.15}$$

where

- $W = W_e + W_m$ which can be equally stated at resonance as twice the stored electric energy $W_e$ or twice the stored magnetic energy $W_m$,

$$W_m = \iiint \frac{1}{2}\mu |\boldsymbol{H}|^2 dv \quad \text{or} \quad W_e = \iiint \frac{1}{2}\epsilon |\boldsymbol{E}|^2 dv. \tag{2.16}$$

- $P_{loss}$ is an all inclusive term for the sum of losses that include wall losses due to finite conductivity, dielectric losses of the medium present inside as well as losses due the external coupling. Usually, the power losses can be distinguished based on the contributions of the conduction and the displacement currents by using $P_w$ and $P_d$ terms separately [Pozar, 2011],

$$P_w = \iint \frac{1}{2} R |I|^2 dS \quad \text{and} \quad P_d = \iint \frac{1}{2}\omega\epsilon'' |\boldsymbol{E}|^2 dv, \tag{2.17}$$

  where $R$ represents the metal surface resistance of the walls, whereas the $\omega\epsilon''$ term represents the frequency dependent losses due to the dielectric medium.

The quality factor of an empty $TM_{010}$ cavity can be stated in terms of the dimensions, the resonance frequency and the metal conductivity $\sigma$ of the walls of the cavity as [Horner et al., 1946]

$$Q_0 = \frac{1}{2}\sqrt{\frac{\sigma}{\pi f_0 \epsilon_0}} \frac{2.4048}{b/d + 1}. \tag{2.18}$$

### 2.1.3 Dielectric Loaded $TM_{010}$ Cavity

When a $TM_{010}$ mode cylindrical cavity is partially filled by a coaxial insertion of a sample with the radius $a$ and permittivity $\epsilon_r$, then from Eq.(2.8) with $\beta_z = 0$ and $\beta_r = \sqrt{\epsilon_r}\beta$, the electric field distribution for the inner dielectric region 1 and the outer region 2 are stated as

$$E_z^1 = J_0(\sqrt{\epsilon_r}\beta r) \quad \text{for} \quad 0 \leq r \leq a, \tag{2.19a}$$

$$E_z^2 = A_1 J_0(\beta r) + A_2 N_0(\beta r) \quad \text{for} \quad a \leq r \leq b, \tag{2.19b}$$

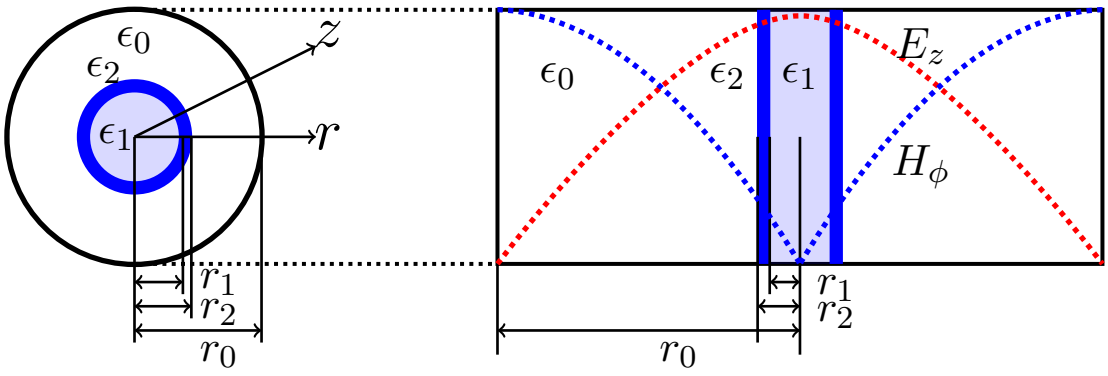


Figure 2.3: TM Cavity Resonance

where the constant for the equation of region 1 is taken as unity and $A_1$ and $A_2$ are the constants for region 2. Similarly the magnetic fields for region 1 and 2 are given as

$$H_\phi^1 = j\sqrt{\epsilon_r}\sqrt{\frac{\epsilon_0}{\mu_0}}\mathrm{J}_1(\sqrt{\epsilon_r}\beta r) \quad \text{for} \quad 0 \le r \le a, \tag{2.20a}$$

$$H_\phi^2 = j\sqrt{\epsilon_r}\sqrt{\frac{\epsilon_0}{\mu_0}}\Big[A_1\mathrm{J}_1(\beta r)] + A_2\mathrm{N}_1(\beta r)\Big] \quad \text{for} \quad a \le r \le b. \tag{2.20b}$$

The transcendental equation, identical to Eq.(2.8), can be obtained by eliminating the constants $A_1$ and $A_2$ in Eqs.(2.19) and (2.20) using at $r = a$ air-dielectric and at $r = b$ metal boundary conditions, then solving for the relative permittivity $\epsilon_r$ of the dielectric perturbation resulting in [Carter, 2001]

$$\sqrt{\epsilon_r} = \frac{\mathrm{J}_0(\sqrt{\epsilon_r}ka)}{\mathrm{J}_1(\sqrt{\epsilon_r}ka)}\left(\frac{\mathrm{J}_1(ka)\mathrm{N}_0(kb) - \mathrm{J}_0(kb)\mathrm{N}_1(ka)}{\mathrm{J}_0(ka)\mathrm{N}_0(kb) - \mathrm{J}_0(kb)\mathrm{J}_0(ka)}\right). \tag{2.21}$$

In some instances, a dielectric insert tube made of glass or quartz is used as a holder for the sample, particularly when the sample is liquid with no definite shape. The main advantage of an insert is to keep the resonating cavity physically isolated from the contamination of the sample material. Moreover, the insert material or the holder should be temperature and moisture resistant. In such an instance, there is an additional dielectric in the cavity, so the transcendental equation can be modified for two coaxially and concentric but non-overlapping material fillings. Fig.2.3 depicts the general case of a $\mathrm{TM}_{010}$ cavity filled with a sample of permittivity $\epsilon_1$ and radius $r_0$, inside a thin tube of a suitable material like quartz with permittivity $\epsilon_2$ and radius $r_2$. The outer section of the cavity is air-filled with radius $r_0$. The transcendental equation for this particular geometry is given as [Shihe et al., 1981]

$$\sqrt{\epsilon_1} = \frac{\mathrm{J}_0(\sqrt{\epsilon_1}kr_1)}{\mathrm{J}_1(\sqrt{\epsilon_1}kr_1)}\sqrt{\epsilon_2}k_0\frac{\mathrm{J}_{121}\mathrm{N}_{022} - \mathrm{N}_{121}\mathrm{J}_{022} - K(\mathrm{J}_{121}\mathrm{N}_{122} - \mathrm{N}_{121}\mathrm{J}_{122})}{\mathrm{J}_{021}\mathrm{N}_{022} - \mathrm{N}_{021}\mathrm{J}_{022} - K(\mathrm{J}_{021}\mathrm{N}_{122} - \mathrm{N}_{021}\mathrm{J}_{122})}, \tag{2.22}$$

with

$$K = \epsilon_2\frac{\mathrm{J}_{000}\mathrm{N}_{002} - \mathrm{J}_{002}\mathrm{N}_{000}}{\mathrm{J}_{000}\mathrm{N}_{102} - \mathrm{J}_{102}\mathrm{N}_{000}},$$

with Bessel functions of first and second kind $\mathrm{J}_{nml}$ and $\mathrm{N}_{nml}$, respectively, with subscripts indicating the order $\mathrm{Z}_{nml} = \mathrm{Z}_n(k_m r_l)$. The numerical solution of Eq.(2.21) has been presented in a number of publications [Horner et al., 1946; Shihe et al., 1981; Li and Bosisio, 1982]. The transcendental equation represents essentially the relation of resonance frequency of the cavity in terms of the dimensions and the dielectric properties of the dielectric sample and the empty

air-filled region. Usually, the form is not very convenient for practical purposes as $k_{r1}$ remains a function of the relative permittivity. Therefore, some rearrangement and simplifications in the full wave formulation are carried out to arrive at expressions for evaluating the real permittivity and the loss tangent in terms of the dimensions of the sample $a$ and the cavity $b$. These expressions are used to measure the small shift in the resonance frequency $\Delta f$ and the change in the quality factor $\frac{1}{\Delta Q} = \frac{1}{Q'} - \frac{1}{Q_0}$ as [Kanpan et al., 2012]

$$\epsilon'_r = 1 + 0.539\frac{b^2}{a^2}\Big(\frac{\Delta f}{f_0}\Big), \tag{2.23a}$$

$$\epsilon''_r = 0.269\frac{b^2}{a^2}\Big(\frac{1}{\Delta Q}\Big), \tag{2.23b}$$

where $Q_0$ is the quality factor of the empty cavity $Q_0$, as stated in Eq.(2.18), and $Q'$ is the quality factor after insertion of the sample.

## 2.2 Perturbation Analysis

The perturbation technique is usually employed to estimate the losses due to the finite conductivity in waveguide propagation, with the initial approximation that the inside field distributions are equal to that with perfect conducting walls. Similarly, in cavity resonators the perturbation method is a useful approach in estimating the influence of local deformations of volume, size, shape and similar material properties. The primary assumption in the perturbation technique states that the actual fields inside a resonating cavity are not largely disturbed in the perturbed state, i.e. under the influence of shape or material perturbation. The effect of shape deformation or change in material properties causes a differential yet proportional amount of shift in the resonance frequency alongside with a slight lowering of the unperturbed quality factor of the cavity. A general relation between the change in resonance parameters of the cavity and the material properties can be established from the outcome of the perturbation analysis.
If the electric and the magnetic fields are oscillating in the unperturbed state at the complex angular frequency variable $\omega$, then these fields can be stated by [Waldron, 1960]

$$\boldsymbol{E} = \boldsymbol{E_0}e^{j\omega t}, \tag{2.24a}$$

$$\boldsymbol{H} = \boldsymbol{H_0}e^{j\omega t}. \tag{2.24b}$$

The overall change in fields after introduction of a small material sample in the perturbed state causes additional elements of electric $\boldsymbol{E_1}$ and magnetic fields $\boldsymbol{H_1}$ [Waldron, 1960] ,

$$\boldsymbol{E'} = (\boldsymbol{E_0} + \boldsymbol{E_1})e^{j(\omega+\Delta\omega)t}, \tag{2.25a}$$

$$\boldsymbol{H'} = (\boldsymbol{H_0} + \boldsymbol{H_1})e^{j(\omega+\Delta\omega)t}, \tag{2.25b}$$

where $\Delta\omega = \omega_1 - \omega_0$ represents the complex change in the resonance frequency. The cavity perturbation formula in such an instance expresses the relation between the fractional change of the complex resonance frequency for a cavity with volume $V_0$ and the permittivity and permeability of the inserted sample with volume $V_s$ in the form of [Meng et al., 1995]

$$\frac{\Delta\omega}{\omega_0} = \frac{\iiint_{V_s}[(\boldsymbol{E_1}\cdot\boldsymbol{D_0} - \boldsymbol{E_0}\cdot\boldsymbol{D_1}) - (\boldsymbol{H_1}\cdot\boldsymbol{B_0} - \boldsymbol{H_0}\cdot\boldsymbol{B_1})]dV}{\iiint_{V_0}(\boldsymbol{E_0}\cdot\boldsymbol{D_0} - \boldsymbol{H_0}\cdot\boldsymbol{B_0})dV}, \tag{2.26}$$

where the subscript 0 indicates the field components in the unperturbed state and the subscript 1 denotes the perturbation caused by the sample. Usually the unperturbed field quantities $\boldsymbol{E_0}$ and $\boldsymbol{H_0}$ are known for all common types of cavity geometries that include $TE_{10n}$, $TM_{0n0}$ and $TE_{10n}$ modes. However, the additional field quantities $\boldsymbol{E_1}$ and $\boldsymbol{H_1}$ inside the sample or the perturbing object can be only calculated under specific circumstances to arrive at a closed form expression. The perturbation expression in Eq.(2.26) is formulated under the assumptions of perfect conducting cavity walls ($\sigma = \infty$) and small size perturbation objects causing a small shift in resonance frequency, i.e. $\Delta\omega << \omega_0$ [Meng et al., 1995]. The expression for the cavity perturbation can be further simplified by setting a number of approximations to derive a convenient closed form expression for extracting the dielectric permittivity. Following is a brief account of the approximations needed for the convenient transformation into a closed form expression:

- If the perturbation objects are assumed homogeneous, isotropic and linear then the flux density vectors of $\boldsymbol{D}$ and $\boldsymbol{B}$ terms are stated in terms of $\boldsymbol{E}$ and $\boldsymbol{H}$, via the well known constitutive relations. Under this condition, Eq.(2.26) transforms to the form [Carter, 2001]

$$\frac{\Delta\omega}{\omega_0} = \frac{\iiint_{V_s} \left[(\epsilon_0(1-\hat{\epsilon_r})\boldsymbol{E_0}\cdot\boldsymbol{E_1}) - (\mu_0(1-\hat{\mu_r})\boldsymbol{H_0}\cdot\boldsymbol{H_1})\right]dV}{\iiint_{V_0}(\boldsymbol{E_0}\cdot\boldsymbol{D_0} - \boldsymbol{H_0}\cdot\boldsymbol{B_0})dV}. \tag{2.27}$$

- For non-magnetic objects ($\mu_r = 1$) the second term in the numerator can be neglected, which is usually the case of dielectric samples with complex relative permittivity $\hat{\epsilon_r} = \epsilon_r' - j\epsilon_r''$, hence [Carter, 2001]

$$\frac{\Delta\omega}{\omega_0} = \frac{\iiint_{V_s} \epsilon_0(1-\hat{\epsilon_r})\boldsymbol{E_0}\cdot\boldsymbol{E_1}dV}{\iiint_{V_0}(\boldsymbol{E_0}\cdot\boldsymbol{D_0} - \boldsymbol{H_0}\cdot\boldsymbol{B_0})dV}. \tag{2.28}$$

- The fields in the cavity prior to the insertion of the perturbing object and after the insertion are assumed to be similar and reasonably identical. Therefore the denominator can be stated in terms of two times the total energy using Eq.(2.16),

$$\frac{\Delta\omega}{\omega_0} = \frac{\iiint_{V_s} \epsilon_0(1-\hat{\epsilon_r})\boldsymbol{E_0}\cdot\boldsymbol{E_1}dV}{2\iiint_{V_0}\epsilon_0|\boldsymbol{E_0}|^2dV}. \tag{2.29}$$

Equation(2.29) can be conveniently expressed by expanding the complex frequency expression into real and imaginary frequency components that are related separately to the real and imaginary part of the permittivity while replacing the complex angular frequency term $\omega_0$ by a complex $f_0$ resulting in

$$\frac{\hat{\Delta f}}{f} \approxeq \frac{\Delta f}{f_0} - j\frac{1}{2}\left(\frac{1}{Q'} - \frac{1}{Q_0}\right) = -\frac{\iiint_{V_s}(\epsilon'-1)\boldsymbol{E_0}\cdot\boldsymbol{E_1}dV}{2\iiint_{V_0}|\boldsymbol{E_0}|^2dV} + j\frac{\iiint_{V_s}\epsilon''\boldsymbol{E_0}\cdot\boldsymbol{E_1}dV}{2\iiint_{V_0}|\boldsymbol{E_0}|^2dV}. \tag{2.30}$$

From Eq.(2.30) the approximate expression for determining the real and imaginary permittivity can be written as [Meng et al., 1995]

$$\epsilon' \approx 1 + 2C_p \frac{\Delta f}{f_0}, \tag{2.31a}$$

$$\epsilon'' \approx C_p \left(\frac{1}{Q'} - \frac{1}{Q_0}\right), \tag{2.31b}$$

respectively. $C_p$ denotes the overall filling factor in perturbation methods which is defined as

$$C_p = \frac{\iiint_{V_0} |\boldsymbol{E_0}|^2 dV}{\iiint_{V_s} \boldsymbol{E_0} \cdot \boldsymbol{E_1} dV}. \tag{2.32}$$

The overall filling factor $C_p$ in the perturbation analysis is essentially a combination of the so-called cavity shape factor and the sample filling factor. The $\boldsymbol{E_0}$ term in the expression of Eq.(2.32) corresponds to the cavity factor, which depends on the shape of the cavity and the mode of resonance. From Eqs.(2.24) and (2.25) it is evident that the $\boldsymbol{E_0}$ is the actual field of the cavity, which is usually assumed identical before and after the perturbation for small volume perturbing objects. On the other hand, the $\boldsymbol{E_1}$ term in the $C_p$ expression represents the additional field, as per Eq.(2.25), inside the perturbing object. The distribution and orientation of the field inside the sample is actually the measure of the sample filling factor.

### 2.2.1 Sample Filling Factor

The $\boldsymbol{E_1}$ field component is critical in the accurate approximation of the sample filling factor and ultimately the $C_p$ value. The additional $\boldsymbol{E_1}$ field inside the sample has a dependence on whether the sample is fully or partially inserted into the cavity. In addition, the shape of the dielectric sample such as sphere, cylinder or disc is also a critical factor in the evaluation of the $\boldsymbol{E_1}$ component. Both these major contributions of the insertion characteristics and the shape of the sample are summed up in the expression for the depolarization factor $N$. The internal additional field of a dielectric sample can be stated in terms of the polarization vector $\boldsymbol{P}$ as [Parkash et al., 1979]

$$\boldsymbol{E_1} = N\boldsymbol{P}, \tag{2.33}$$

where $N$ is the depolarization factor which depends on the axial ratio of the sample. Depolarization is defined for a perturbing object in the shape of a prolate ellipsoid with three semi axes $h$, $a1$ and $a2$ under the condition $h > a1 = a2$ with axial ratio $m = h/a1$ [Parkash et al., 1979],

$$N = \frac{1}{m^2 - 1}\left[\frac{m}{2\sqrt{m^2 - 1}} \log \frac{m + (\sqrt{m^2 - 1})}{m - (\sqrt{m^2 - 1}} - 1\right]. \tag{2.34}$$

Detailed work on the depolarization factor and its dependence on the sample insertion characteristics is available in a number of articles and publications [Peng et al., 2014; Subramanian et al., 1996; Lin and Afsar, 2006]. For complete insertion, i.e. $m = h/b = 1$, the value of the depolarization factor becomes an integer. Furthermore, for disc samples the value is unity and for spheres it is approximated by $N = 1/3$. When the sample is a concentric thin cylindrical rod inside a cylindrical cavity then the value of $N$ is considered 0. The field inside the sample in such an instance can be approximated by equivalence to the field of the cavity before the insertion of the sample, provided the applied field is tangential to the cylindrical interface, which yields $\boldsymbol{E'} = \boldsymbol{E_0}$ using Eq.(2.25). Additionally, if the field is considered uniform within the sample then the integration terms in Eq.(2.32) are replaced with multiplication resulting in

$$C_p = \frac{|\boldsymbol{E_0}|^2 V_0}{|\boldsymbol{E_0}|^2 V_s}, \tag{2.35}$$

where the $C_p$ term is simplified due to a sample filling factor of unity into the ratio of the respective energy and volumes of the cavity and the sample.
In several perturbation applications, the sample size is too large that the field inside the sample is not uniform. However, the field in such cases can be approximated with the known field distribution of the actual cavity bounded by the sample volume. Whether the applied field is oriented parallel or perpendicular to the sample interface also influences the $\boldsymbol{E_1}$ distribution. For a field oriented normal to the dielectric interface, the $\boldsymbol{E_1}$ field has a dependence on the $\boldsymbol{E_0}$ field proportional to the permittivity value according to [Harrington, 2001; Kumar and Smith, 1977]

$$\boldsymbol{E_1} = \frac{2}{1+\epsilon_r}\boldsymbol{E_0}. \tag{2.36}$$

An electric field normally applied to the interface of the dielectric sample is usually a case that occurs in $TE_{10n}$ types of rectangular cavities with a sample in the form of a thin sheet flowing or placed inside the cavity. In a $TM_{010}$ cavity, the lengthwise placement of a sample conformal to the geometry of the cavity in the shape of a thin rod means a sample filling factor of unity.

### 2.2.2 Cavity Filling Factor

Considering the relevant example of a cylindrical cavity resonator in the $TM_{0n0}$ mode of operation, the cavity shape factor can be simply derived from the relevant Bessel functions, using the relation $E_0 = \mathrm{J}_0(k_c r)$. For a rod shaped thin sample with radius $a$ inside a cylindrical cavity of radius $b$ under uniform applied field assumption the cavity factor can be deduced using the relation for the tangential field at the interface, i.e. $\boldsymbol{E_1} = \boldsymbol{E_0}$,

$$C_p = \frac{\int_b \mathrm{J}_0^2(k_c r) r dr}{\int_a \mathrm{J}_0^2(k_c r)^2 r dr} = \frac{b^2}{a^2}\frac{\mathrm{J}_0^2(k_c b) + \mathrm{J}_1^2(k_c b)}{\mathrm{J}_0^2(k_c a) + \mathrm{J}_1^2(k_c a)} = G\frac{b^2}{a^2}, \tag{2.37}$$

where the values for the shape factor $G$ for $TM_{0n0}$ modes with $k_c = p_{0n}/b$ are listed in Table(2.1).

| $TM_{010}$ | $TM_{020}$ | $TM_{030}$ |
|---|---|---|
| 0.2694 | 0.1157 | 0.0736 |

Table 2.1: Shape factor $G$ values for cylindrical $TM_{010}$ modes

It can be easily verified that using the sample filling factor of unity for thin needle like rods and the cavity filling factor value for the $TM_{010}$ mode cavity, the perturbation formulation of Eq.(2.31) yields identical expressions of Eq.(2.23).

## 2.3 Insertion Holes

The assumptions undertaken during the full wave analysis as well as in the perturbation approach are generally sufficient to determine the dielectric permittivity value within some predicted error range. Regarding the application of the $TM_{0m0}$ cavity, it is established in the previous section that the overall accuracy improves with lengthwise placement of the rod like sample equal to the height of the cavity. The accuracy of the closed form expressions in Eq.(2.23) and Eq.(2.35) also depends on the radial index $m$ and the uniformity of the applied field tangentially

oriented at the sample interface and its neighbourhood. The validity of the assumption that the field is uniform and tangential to the interface improves with smaller radius $a$ of the sample relative to the cavity radius $b$. Furthermore, the presence of deformities such as one-sided or through passage insertion holes also influence the validity of the uniform field approximation during the analysis.
Insertion holes are inevitable design features while employing the cylindrical cavity to continuously measure the change in radius of the sample flowing through the cavity. Although in some designs the insertion holes are replaced by shorting-plugs after placing the sample in the sensing column, but such designs are for performing static measurement. For applications where continuous measurements are needed, the insertions holes are a permanent design feature. Therefore, the effects of insertions holes are required to be accounted for in measurement procedures. Fundamentally, insertion holes are deformities in the ideal cavity shape whose influence is a complicated phenomenon which is difficult to express in a closed form [Ikeda et al., 2003]. Approximate perturbation or variational methods are utilized to estimate the influence of openings in the cavity. In a number of publications, the focus has been on evaluating an accurate error compensation term in the permittivity formulation to account for the insertion holes while employing the cavity for permittivity measurements [Estin and Bussey, 1960; Meyer and Schilz, 1981; Shihe et al., 1981; Li and Bosisio, 1982; Gauthier et al., 1989; Penaranda-Foix et al., 2007].

### 2.3.1 Influence on Frequency Deviations

The radial dimension of the insertion holes relative to the cavity radius has received most attention in various publications. In comparison to the perfectly shielded cavity the cavity with openings exhibits an increase in the resonance frequency that can be experimentally verified for the $TM_{010}$ mode cavity. The increment or frequency deviation is proportional to the radius of the insertion holes created on the cavity end-plates or lids. Conventionally, the amount of frequency increment caused by insertion holes is numerically evaluated by accounting for the so-called frequency pulling effect. The phenomenon of frequency pulling is based on the Adiabatic Invariance theorem, which states that the relative change in frequency is equal to the relative energy change of the system caused due to the change in configuration of the system [Estin and Bussey, 1960]. Here the change in configuration of the system refers to deformities such as the insertion holes. Regarding the permittivity formulation, Estin and Meyer developed an error compensation term for the real permittivity expression in Eq.(2.31a) to account for the increment of the measured resonance frequency due to the insertion holes [Estin and Bussey, 1960; Meyer, 1977]. In the extended work from Li and Gauthier [Shihe et al., 1981; Gauthier et al., 1989], the error corrections due to the insertion holes were included for both the real and the imaginary part in the permittivity formulation. In accordance with the perturbation theory, the compensation is generally valid for small changes in energy, i.e. small radius of insertion holes $s$ with upper limit stated as

$$\frac{b^2}{m^2} >> s^2\epsilon_{ri},$$

where $m$ is the mode number and $\epsilon_{ri} \approx 1$ for the usual air-filled insertion hole without the sample.

### 2.3.2 Error Compensation Terms

The influence of the sample insertion holes on end-plates of the cavity is analysed by considering these circular holes as the openings of long cylindrical tubes attached to the cavity lids. Smaller radius of the tubes $s << b$ asserts the condition which ensures that the waves at the opening are of evanescent nature or simply below cut-off in terms of propagation. The evanescent fields

eventually decay inside the long tube within a short length. However, the evanescent fields contribute additional field components in the vicinity of the openings, similar to the additional $\boldsymbol{E_1}$ field contribution stated in Eq.(2.25). Consequently, the filling factor term given in Eq.(2.32) is modified proportional to the contribution of the additional fields. The general sum of the contribution of electric field components inside the circularly symmetric tube of arbitrary length $L$ with permittivity $\epsilon_{ri}$ is stated as [Gauthier et al., 1989]

$$E_z = \sum_{m=1}^{\infty} \frac{A_L}{j\omega_1 \epsilon_0 \epsilon_{ri}} \left(\frac{p_{0m}}{s}\right)^2 \mathrm{J}_0\left(\frac{p_{0m}}{s} r\right) e^{-j\gamma L}, \tag{2.38a}$$

$$E_r = \sum_{m=1}^{\infty} \frac{A_L}{\omega_1 \epsilon_0 \epsilon_{ri}} \left(\frac{p_{0m}}{s}\right)^2 \mathrm{J}_1\left(\frac{p_{0m}}{s} r\right) e^{-j\gamma L}, \tag{2.38b}$$

where

- the coefficient $A_L$ is of the form

$$A_L = A_m \frac{s^2 \epsilon}{2b^2 \mathrm{J}_1(p_{0m})}.$$

- $p_{0m}$ are the roots of the Bessel function $\mathrm{J}_0$.
- $\gamma \approx -jp_{0m}/s$ are the evanescent wave numbers at the opening of the long insertion tube.

While deriving the correction term, Estin and Meyer considered only the $\mathrm{TM}_{01}$ mode to be significant enough for excitation inside the tube, since the higher order modes decay exponentially, which can be verified from Eq.(2.38). Later, Li and Akyel included higher order terms of $\mathrm{TM}_{0m}$ modes for excitation inside the insertion tube, while specifically treating the influence of a one-sided insertion tube. The simplified empirical expression accounting for the frequency pulling effect in terms of the normalized frequency shift $\delta f$ is stated as [Estin and Bussey, 1960]

$$\frac{\delta f}{f_0} = K_n \frac{s^3 \epsilon_r^{1+\Delta}}{b^2 d}, \tag{2.39}$$

with

$$K_m = \sum_{m=1}^{\infty} \frac{A_m^2 \mathrm{J}_1^2(p_{0m})}{p_{0m}},$$

where

- $K_m = 0.386$ and $0.87$ for $n = 1, 2$, respectively. $n$ represents the number of circular symmetric modes under consideration inside the insertion hole.
- $s$ is the hole radius, $b$ is the cavity radius and $d$ is the cavity height.
- $\Delta = 0.16$ is an empirical constant term.

In Li's work [Li and Bosisio, 1982], the exact solution is derived specifically for a lossy dielectric sample inside a $\mathrm{TM}_{010}$ cavity provided with insertion holes. The field solution states that for highly lossy dielectric samples the real part of the permittivity is the function of both the frequency shift as well the change in the loaded quality factor, i.e. $\dfrac{\Delta f}{f_0} = \dfrac{1}{2\Delta Q}$, whereas the imaginary part is just proportional to the change in the loaded quality factor as stated in Eq.(2.31b). Thus, the presence of insertion holes additionally lowers the quality factor by a factor $Q_i$, so the Eq.(2.31b) can be modified as

$$\frac{1}{\Delta Q} = \left(\frac{1}{Q'} + \frac{1}{Q_i}\right) - \frac{1}{Q_0}, \tag{2.40}$$

which directly influences the imaginary component of the permittivity and indirectly the real component of the permittivity in accordance with Li's work. However, the results were limited to the case of twenty times smaller sample radius relative to the cavity radius. Overall the approximate relative errors in the permittivity formulation of Eq.(2.31) are reported as [Li and Bosisio, 1982; Gauthier et al., 1989]

$$\frac{\delta\epsilon_r' - 1}{\epsilon_r' - 1} \approx \frac{M_i s}{2p_{01}d}, \tag{2.41a}$$

$$\frac{\delta\epsilon_r''}{\epsilon_r''} \approx \frac{N_i s}{2p_{01}d}, \tag{2.41b}$$

where $M_i$ and $N_i$ terms are numerically evaluated by considering a sufficient number of modes from Eq.(2.39). It is apparent from the expressions of the relative errors in Eq.(2.41) that the error reduces with reduced insertion hole size $s$ as well as with increasing cavity length or height $d$.

Another important parameter is the influence of depth or thickness of the insertion holes on the increment of the frequency shift during resonance measurements. In Fig.2.4 a sketch of a cavity is depicted with different variables assigned to its various dimensions. The tube effect due to the thickness $g$ of the insertion hole has been specifically computed through numerical evaluation via a number of parametric simulations in the work of Kawabata [Kawabata et al., 2004; Kawabata and Kobayashi, 2005]. For tube lengths, which are below a few tenths of the operating wavelength an increase in the resonance frequency occurs due to the increased stored energy within the openings which decreases the effective capacitance of the cavity. However, the frequency shift becomes constant and does not change beyond a certain thickness of the insertion tube, as the evanescent modes are diminished rapidly with increasing thickness. Generally, a few millimeters of insertion hole depth are sufficient for wavelengths of operation above 100 mm to reach a stable frequency deviation due to the openings.

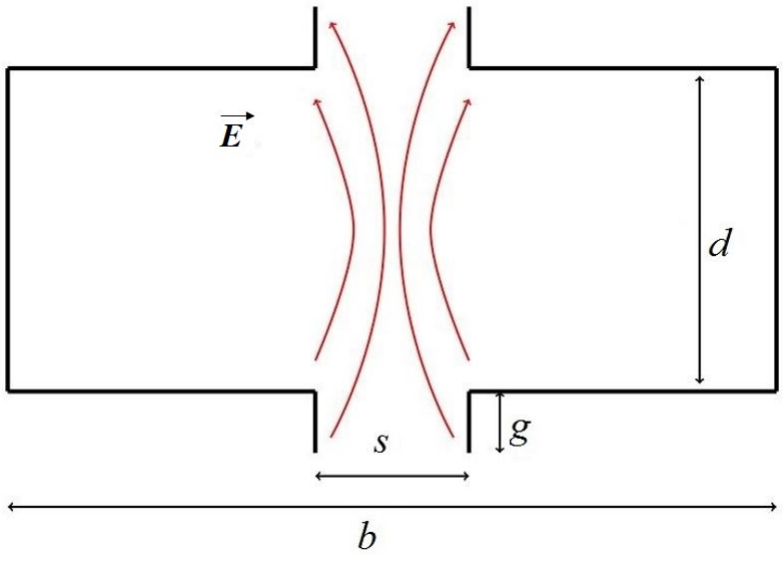


Figure 2.4: Approximate Electric Field Distribution due to the Insertion Holes

### 2.3.3 Capacitive Column Treatment

The increment in frequency shift indications can also be explained by analyzing the capacitance of the length of the sensing column in between the top and bottom insertion holes. The reason for the increment in frequency can be traced primarily to the loss in the capacitance of the concentric sensing column in the cylindrical cavity. Thomassen presented the quantitative analysis for the capacitive column regarding linear accelerator applications of $TM_{0n0}$ mode cavities [Thomassen, 1965]. The insertion hole causes fringing field effects in the vicinity of the opening, hence decreasing the overall capacitance of the column and eventually causing an increase in the resonance frequency. The change in static capacitance of the column around the axis of the cavity of length $d$ under the circular periphery of insertion hole with radius $s$ is stated as [Thomassen, 1965]

$$C_{open} = \epsilon_0 \epsilon_{ri} \pi \frac{s^2}{d} (\alpha - \beta), \tag{2.42}$$

where

- the term $\alpha$ refers to the reduction in the static capacitance, with values between $0 < \alpha < 1$. It is stated as
$$\alpha = \frac{2b\mathrm{J}_1(p_{01}a/b)}{p_{01}a\mathrm{J}_0(p_{01}a/b)}.$$
- the term $\beta$ accounts for the effect of the fringing capacitance as per the expression proportional to the term $\frac{4a}{d}$.

In the limiting case of a very small insertion hole, i.e. $s \approxeq 0$, $\alpha$ approaches 1 and $\beta$ is approximated by replacing it with 0. The $\alpha$ term can also be interpreted as the change in the longitudinal component $E_z$, whereas $\beta$ is the origin of the radial component $E_r$ due to te fringing effects in the vicinity of the insertion hole, as illustrated in Fig.2.4. The nature of the $E_z$ and $E_r$ field components is stated in Eq.(2.38).
A very common way to compensate the insertion hole effect on the overall resonance measurement is discussed in detail by Ikeda [Ikeda et al., 2003]. The approach is essentially based on increasing the aspect ratio, i.e. $s/d$ between the insertion hole radius $s$ and the cavity height $d$ [Ikeda et al., 2003]. A number of experiments are performed to establish that by decreasing the aspect ratio or by increasing the height of the cavity, the influence of the opening reduces. Consequently, for aspect ratio values much below one-tenth the non-uniformity of the field is confined only in the vicinity of the opening but the overall longitudinal components stay tangential with minimal fringing effect of the electric field.

## 2.4 Problem Description

In the previous sections, the full wave as well the perturbation approach has been discussed in detail regarding propagation and standing wave solutions in cylindrical structures. In addition, to determine the resonance frequency shifts and impedance changes another approach called variational methods are often employed. However, rather the behaviour of the dielectric insertion on the resonance or impedance characteristics, the interest is on the electric field distribution of the cavity, particularly under non-ideal perturbations like insertion holes. More elaborately, in the presented work rather than on numerically accurate determination of the dielectric permittivity, the interest is directed towards the behaviour of the electric field due to the presence of the insertion holes. While measuring small changes in the radius of the sample continuously flowing through the sensing column, the non-uniformity due to the additional electric field contributes to frequency shift indications even for offset movements of the sample away from the axis of the cavity. Therefore, the focus of the work is to seek solutions to compensate

the additional electric field present in the sensing column marked by the insertion holes during resonance frequency measurements.
A variety of material characteristics such as size, mass, density, etc., require real-time and continuous monitoring and control during mass production in an industrial environment. Often the materials in such a process are in a continuous state of motion or flow in a certain predefined direction. The monitoring and control of a production flow demand for quick and efficient means of performing the run-time measurement by employing some appropriate sensor technique. The outcome of the applied sensor can be either used as a performance indicator of the process, or alternatively utilized to control the critical factors of the processing efficiency in an open or a closed feedback loop.
The presented work is an attempt to develop a frequency-domain microwave sensor technique for measuring the physical characteristics of low-loss materials, which are in a state of motion in elongated cylindrical shapes. The goal is to develop a microwave sensor that exhibits the high accuracy feature of cavity resonators and combines it with the level of flexibility associated with free-space techniques to provide run-time or continuous sensing. More specifically, the aim is to design and develop a sensing structure that can perform continuous measurement of differential changes in the radius of rod-shaped samples under flow. Additionally, the sensor must also be able to accommodate a variety of sample sizes within a certain limit.

### 2.4.1 Sensor Specifications

The foremost requirement for the potential sensor entails the provision to guide the contact-less flow of the material through the sensor. The so-called fixed passage should comprise sufficient volumetric space to allow for different reference samples with different mean values of thickness. Moreover, the sensing structure should ideally have high spatial resolution along the length of the sample. It can be practically attained by smallest possible lengthwise interaction of the applicator and the sample with respect to the operating wavelength. Furthermore, the limitation on the length of interaction is also preferred from the aspects of dimensional constraints of sensor installation on the host machine.
A short pill-box shaped $TM_{010}$ mode cavity resonator potentially serves as an appropriate geometry that fulfills the necessary requirements of generating a measurable response in terms of the frequency shift $\Delta f$ and a drop in the quality factor $\Delta Q$, as illustrated in Fig.2.5. In addition, the proposed cavity also has the ability to fit to the dimensional constraint of a limited length, because the resonance frequency of the $TM_{010}$ mode is not a function of the length of the cavity. The characteristics of a $TM_{010}$ mode cavity resonator relevant to the problem are summarized below:

- The cavity has an axial electric field in the middle of the cavity volume. The central volumetric region around the axis acts similar to a parallel disc capacitor. The central column is highly sensitive to changes in dielectric properties of the material, due to the presence of a strong axial electric field.

- The provision for the through-passage of the material flow is relatively simple to implement by creating circular insertion holes of the required dimensions in the top and bottom cavity walls. Moreover, the current distributions on the inner walls of the cavity are not largely disturbed if the insertion holes are created in the middle of the lids of the cavity. The overall cylindrical volume created in this manner acts as a sensing column for the sample flow.

- The magnetic field is circumferential with maximum strength away from the axis of rotation. Therefore, the provision for the dielectric insertion does not largely influence the magnetic field distribution. In addition, the cavity can be magnetically coupled via

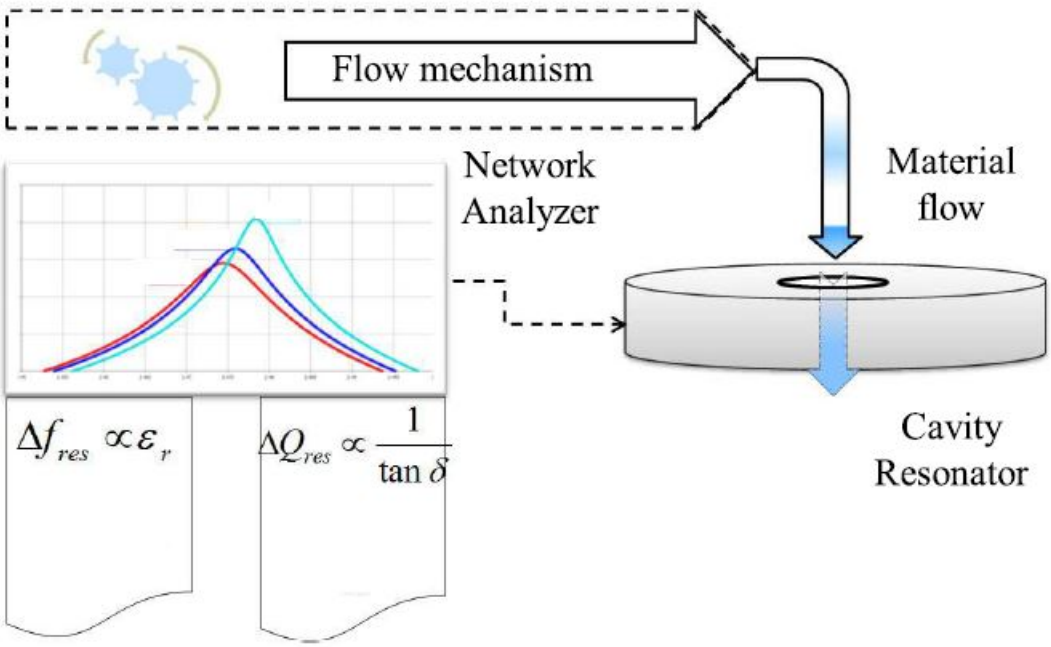


Figure 2.5: Schematic Illustration of the Sensor Application

loops in the outer walls keeping the excitation strength predominantly independent of the dielectric interaction.

The primary solution to the problem is proposed in the work by [Hermann et al., 2008]. The presented work is an extension of the solution with advancements and improvements of the primary design to reduce and minimize the measurement errors. The major source of error are undesired frequency shift indications due to axial offset of the samples concentrically flowing through the cavity. Such type of axial offsets are usually caused by the occurrence of ever-existing vibrations from the moving machine parts upon which the sensor is supposed to be installed.

### 2.4.2 Sensing Column Model

In order to model the problem a fixed dimensioned sensing region can be defined around the reference sample of varying thickness. The sensing region accommodates the radial variations of the sample, so the two entities comprising the sample and the sensing column can be combined into one entity. To further elaborate the problem an analogy using the effective permittivity definition can be drawn to measure such a single entity.
A geometrical scheme of two concentric cylinders is assumed to achieve the desired model. The outer cylinder with larger yet fixed diameter represents the air-filled sensing columns, whereas the inner cylinder serves as an approximation for the dielectric sample, whose differential changes in thickness or radius are required to be measured. Based on this model, the change in radius or effectively the volume of the dielectric sample can be translated as alteration in the fractional volume of the air-dielectric mixture. The effective permittivity of the mixture varies in proportion to the variation in the fractional volume. For a uniform applied field the expression for the effective permittivity is the ratio of the sum of the volume based weighted permittivity of individual materials divided by the total volume of the mixture. However, it is to be noted that the expression for the effective permittivity of the air-dielectric mixture also depends on the orientation of the applied electric field inside the whole cylinder. Wiener derived the mixing formula for laminated dielectric solids stacked between two different field orientations or

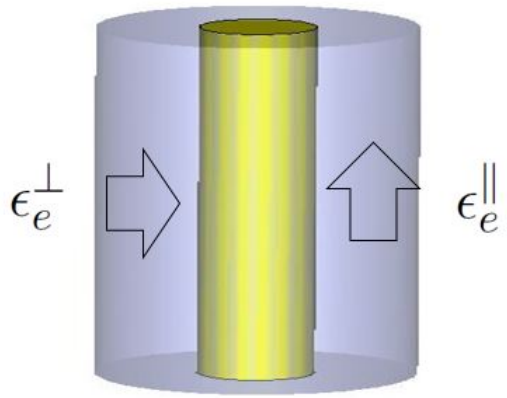


Figure 2.6: Effective Permittivity under Orthogonal Field Orientations

phases [Bal and Kothari, 2010]. The field orientation corresponds to the direction of the field in the whole surrounding of the air-dielectric mixture in relation to the surface normal vector of the laminated dielectric surface. An identical formula can be applied to a thin rod concentrically placed along the full length of the cylinder. When the inner cylindrical volume is surrounded by a uniform electric field parallel or tangent to the air-dielectric interface at the sample walls then the effective permittivity, represented by $\epsilon_e^{\parallel}$, can be stated as [Bal and Kothari, 2010]

$$\epsilon_e^{\parallel} = \frac{\epsilon_r^a V_a + \epsilon_r^s V_s}{V_a + V_s}, \tag{2.43}$$

where $\epsilon_r^a$ and $\epsilon_r^s$ are the permittivity values and $V_a$ and $V_s$ are the volume occupancies for air and the dielectric, respectively. On the other hand, when the applied field is oriented normal to the air-dielectric interface then the effective permittivity, denoted by the symbol $\epsilon_e^{\perp}$, is stated as [Bal and Kothari, 2010]

$$\epsilon_e^{\perp} = \frac{\epsilon_r^a \epsilon_r^s (V_a + V_s)}{\epsilon_r^a V_s + \epsilon_r^s V_a}. \tag{2.44}$$

Figure 2.6 depicts the concentric cylinders and the orthogonal field orientations for the evaluation of the effective permittivity. In essence, the two orthogonal effective permittivity expressions refer to the measurement of series and parallel capacitive effects. Equation(2.43) corresponds to the case of two parallel-connected capacitors which yields a maximum value, whereas Eq.(2.44) corresponds to the pair of series-connected capacitances resulting in a minimum sum capacitance. The actual value of the effective permittivity of a dielectric rod inside the air-filled cylinder under the influence of a random sum of parallel and perpendicular components of the applied electric field lies in between the two extremes of $\epsilon_e^{\perp} \leq \epsilon_e \leq \epsilon_e^{\parallel}$. The true proportion depends on the contribution of each field component, which is an unknown quantity in a variety of instances.

Since both the effective permittivity expressions are based on the proportions of volume occupancies of respective air and dielectric cylinders, these values are invariant to the dielectric position within the larger air-filled cylinder. For example, if the dielectric sample is displaced or undergoes a position offset from the concentric axis within the air cylinder, the effective permittivity value of the combined measuring entity as per the mixture formulas remains unchanged. The reason for the position insensitivity in the mixing formula can be attributed to the primary assumption that there exists a completely uniform and unidirectional electric field distribution around the whole volume of the air-dielectric mixture.


Figure 2.7: Draw Frame Machine [Rieter GmbH, 2017]

In the above context, the problem under study deals with measurement errors in the differential changes of the radius of a sample under the influence of a non-uniform electric field in the surroundings. The non-uniform field is predominantly due to the presence of additional field components apart from the axial component of the electric field. In general, the absolute sum of the electric field within the whole sensing column in between the openings of insertion holes of cylindrical cavities is difficult to express in a closed form expression.

### 2.4.3 Application Example

A relevant practical example which is specifically applicable to the concerned measurement problem can be given by the spinning phase in the production cycle of yarns in the textile industry. One of the key stages in the formation of the yarn is called drawing, which is carried out using draw frame machines, as pictured in Fig.2.7. The quality of the yarn, which influences the worth of the final yield, is determined by the sliver or fiber of the textile material produced at the drawing and combing stage [Rieter GmbH, 2017]. The delivery speed of the drawing process is a critical factor that influences the evenness of the sliver. The evenness of the sliver is ensured by using the auto-leveller with the drawing machine in an open or closed feedback loop [Rieter GmbH, 2017]. The ability to maintain the evenness of the sliver via controlling the delivery speed can be achieved by employing a suitable microwave sensing technique for high speed continuous processing. The sensor should also have the ability to be easily integrated into the draw frame machine to perform the levelling function at the input and/or output stages of sliver formations.
The associated parameter of measure in this specific case is the change in the linear mass density, usually stated in the unit of $1\,\mathrm{kTex} = 1\,{}^{\mathrm{gm}}/_{\mathrm{m}}$. In order to draw a constant kTex value in a process cycle, a sensor can be employed to detect and measure the variations in the linear mass density. Generally, a draw frame machine can accommodate 2.5 -7.0 kTex of varying linear density slivers. Therefore, the sensor should also have the ability to be calibrated to various kTex references. While the sensor is mounted on the draw frame, it also undergoes some vibrations caused by the machine. Irrespective of the vibration effects on the sensor and the sliver, the microwave sensor

should provide the necessary output for a regulated delivery speed to maintain a uniform mass density. The pill-box cavity along with its design features as elaborated in Sec.2.4.1 serves as a practically fitting sensor solution for such measurements. It is now evident that the effective permittivity analogy drawn in Sec.2.4.2 is similar to the problem of ensuring a constant kTex flow through the cavity without the influence of lateral position offsets in the concentric flow on the measurements.

## 2.5 Cavity Computations

### 2.5.1 Cavity Design and Dimensions

The earliest prototype developed during the course of the work consisted of a standard $TM_{010}$ mode pill-box cavity resonator. The three dimensional image of the design is depicted in Fig.2.8, which shows both the inner and the outer view of the cavity equipped with insertion holes and shown with a rod shaped sample passing through the sensing column. A detailed account on the dimensional specification with comments on the cavity features is as follows:

**Resonator Diameter:** The main resonator body is a short cylinder with the inner diameter ranging from 90 mm to 95 mm. As per Eq.(2.14), the resonance frequency of the fundamental $TM_{010}$ mode for the specified diameter range lies within the 2.40 GHz − 2.50 GHz ISM band.

**Sensing Column:** The sensing channel or column provided for the flow of the sample comprises the concentric inner cylindrical region with circular opening of 11 mm diameter on the top and bottom walls of the cavity. These fixed openings have the ability to accommodate different reference samples of diameters up to 11 mm.

**Resonator Height/Length:** The internal height or length of the cavity is kept in the range from 14 mm minimum to 18 mm maximum. In general, the reason for the height limitation is related to space constraints while installing the device on host machines. Additionally, the cavity should have minimum possible axial length for the smallest spatial resolution along the linear path of the sample flow. The limitation results in two significant drawbacks in the design, which include the loss of overall quality factor and a strong influence of the cavity openings on the orientation and strength of the electric field distribution in the sensing column.

**External Coupling:** The cavity is coupled with the external source and measurement equipment via a pair of magnetic loops around the periphery of the cavity. The loop length is critical in determining the coupling coefficient. The cavity is coupled to attain the return loss of 14 dB and the insertion loss under 3 dB. The pair of loops can be either directly placed close to each other or fitted at the angular difference of 180 ° around the circumferential path.

### 2.5.2 Computations

A number of constraints on the design specifications and resulting dimensions of the cavity prototype have adverse effects on the ideal resonance response. Predominantly, the electric field distribution of the cavity resonator is no longer ideal and the approximations made in cavity analysis are not largely valid. The most significant factor contributing to the deviations is the relative size of the insertion holes in comparison to the overall height of the cavity. The provision of insertion holes made for the passage of concentric material causes non-uniform electric fields over and inside the sensing channel region. Numerical computations are carried out to evaluate the phenomenon of these deformities leading to an influence on the resonance frequency measurement. These numerical evaluation are performed by carrying out simulations in CST-Microwave Studio [Computer Simulation Technology, 2017].

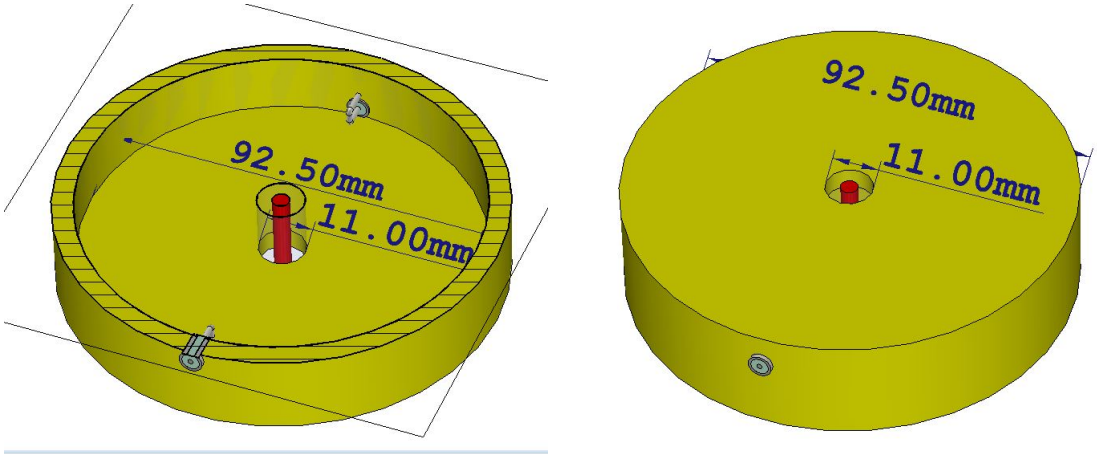


(a) Inner 3D View of the Cavity Model (b) Outer 3D View of the Cavity Model

Figure 2.8: Pill-Box Cavity with Insertion Holes

#### 2.5.2.1 Effect of Insertion Hole on Sample Offset

A comparison of two cavities of identical dimensions but with and without insertion holes is made to demonstrate the effect of sample offsets on resonance frequency deviations. In order to model the sample cylindrical rods of three varying radii 1.0 mm, 1.2 mm, and 1.4 mm are chosen for simulations. The samples are modelled as lossless material with two different permittivity values of $\epsilon_r = 1.5$ and 2.1. During the computation the samples are moved away from the axial center with a step size of 1 mm, i.e. from 0 mm to 4 mm point along the radial line measured from the center in $N = 5$ number of steps.

The computational results for the closed cavity resonator are depicted in Fig.2.9. In Fig.2.9a the measure of absolute frequency shift in tens of kHz is shown. Similarly, Fig.2.9b depicts the percentage shift parameter deduced from normalizing the frequency shift due to the sample offset by the resonance value when the sample is at the axial center. The magnitude of the electric field drops as per the Bessel function curve, i.e. $J_0(r)$, away from the axis. The slight decrement in frequency shift for sample offsets is clearly due to the gradually decreasing azimuthal electric field component along the radius. In terms of percentage shift, the frequency drops approximately to 2.5 % when compared to the null offset frequency. Moreover, the percentage shift is highest for the lowest permittivity ($\epsilon_r = 1.5$) with the largest radius (1.40 mm). This result validates the concept that the tangential electric field component at the sample interface is less excluded for the sample with lower permittivity as compared to the higher permittivity sample.

In comparison, the cavity with 5.5 mm radial insertion hole shows opposite nature of the frequency shift variations due to the sample offset positioning, as illustrated in Fig.2.10. When compared to the closed cavity case, the computation results show relatively large variations in the resonance frequency shift due to the axial offset of the sample. However, unlike the closed cavity case these variations are in the form of a slight increase in the resonance shift. The observed effects are attributed to the presence of the radial electric field component around the insertion hole region. Another factor is the deformation or bending of the azimuthal electric field due to the absence of the top and bottom conductors in the sensing column. Absolute variations illustrated in Fig.2.10a for the similar sample dimensions and permittivity values as the closed cavity is the order of hundreds of kHz. Accordingly, the percentage shift also results in almost 20 % normalized shift as compared to the zero offset at the axial center. Moreover, these frequency deviations are maximum for the sample with higher permittivity and larger radius. For this reason, it can be deduced that there is a strong presence of the radial electric field component with orientation normal to the sample interface. Hence, the frequency deviations

are larger for higher permittivity in contrast to the closed cavity that can be attributed to an increased drop in radial field strength normal to the interface for the high permittivity samples.

#### 2.5.2.2 Effect of Aspect Ratio on Sample Offset

The deviations of frequency shift while moving the sample away from the axis can be mitigated by increasing the aspect ratio, i.e. the ratio of height of the cavity to the diameter of the insertion hole. Increasing the height of the cavity also improves the quality factor of the $TM_{010}$, as per Eq.(2.3). More importantly, the significant influence of increased height is the confinement of the effects of the openings to relatively smaller volume, thus limiting the radial component

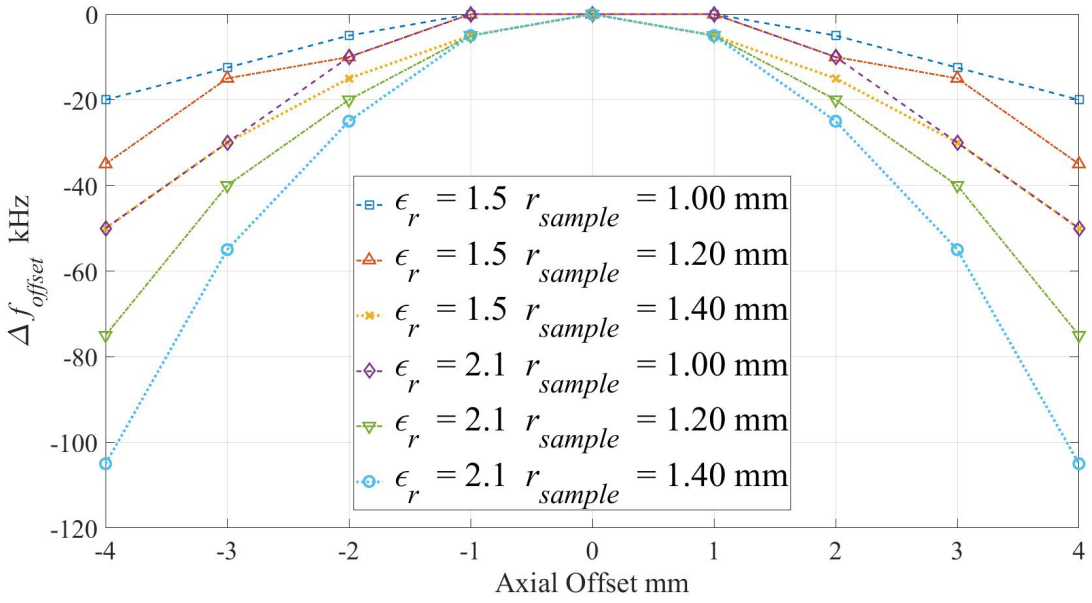


(a) Absolute Frequency Deviation

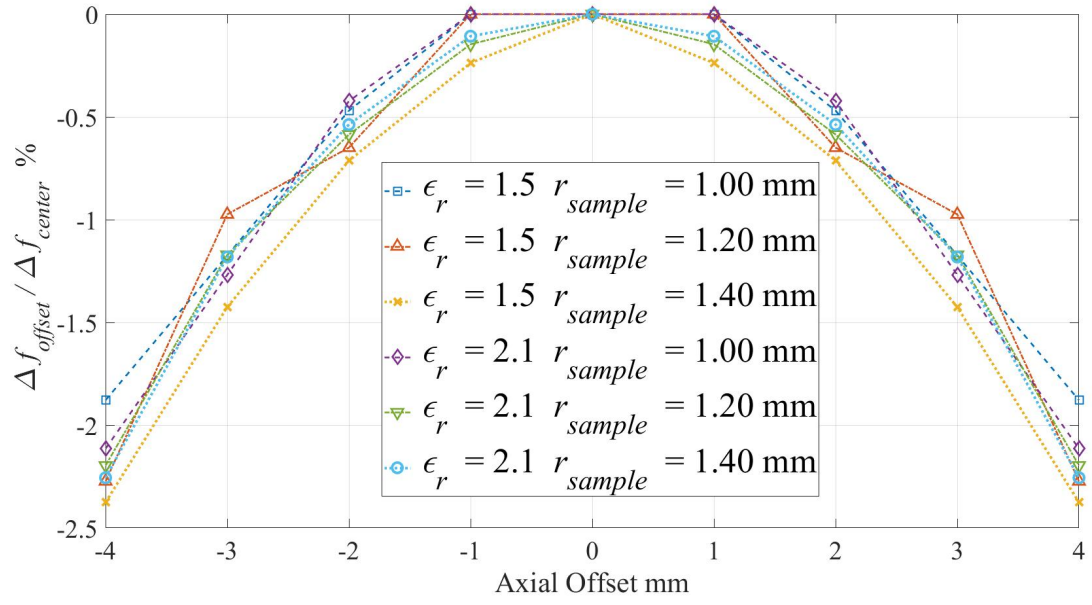


(b) Relative Frequency Deviation

Figure 2.9: Effect of Sample Offset in a Closed Cavity

effect. In addition, the bending of the azimuthal electric field occurring due to the absence of the top and bottom conductor tends to reduce with the increased height.
The validation of the conclusion drawn above is demonstrated by the computation results illustrated in Figs.2.11 and 2.12. Two different cavity height or lengths of 30 mm and 60 mm were utilized for computation with identical insertion hole of 5.5 mm radius. The amount of percentage deviation reduced for the sample offset to 10 % and further down to 2 % for the 30 mm and 60 mm cavity heights, respectively.

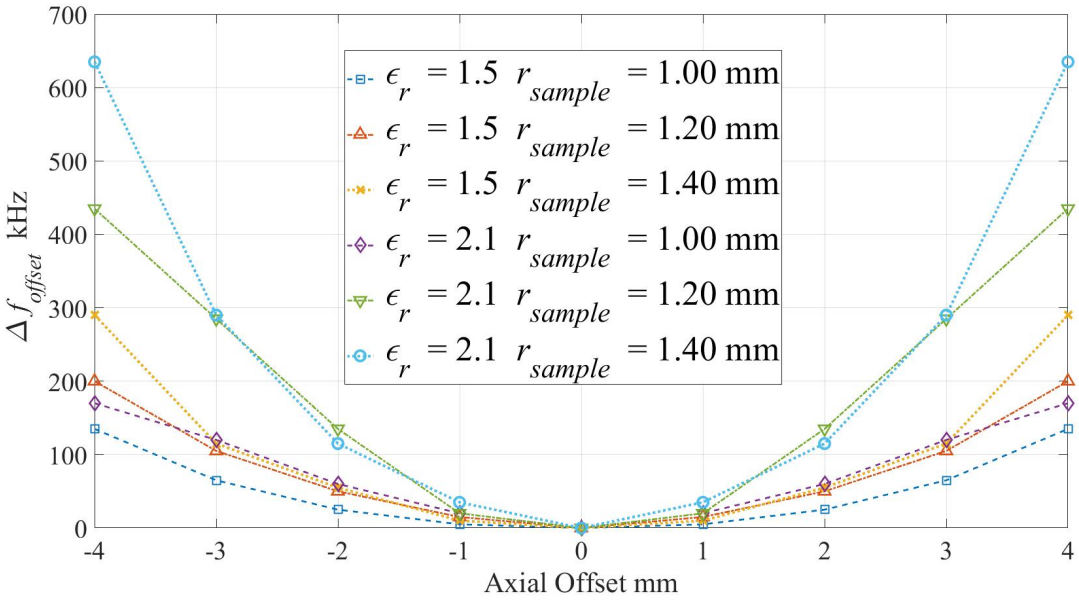


(a) Absolute Frequency Deviation

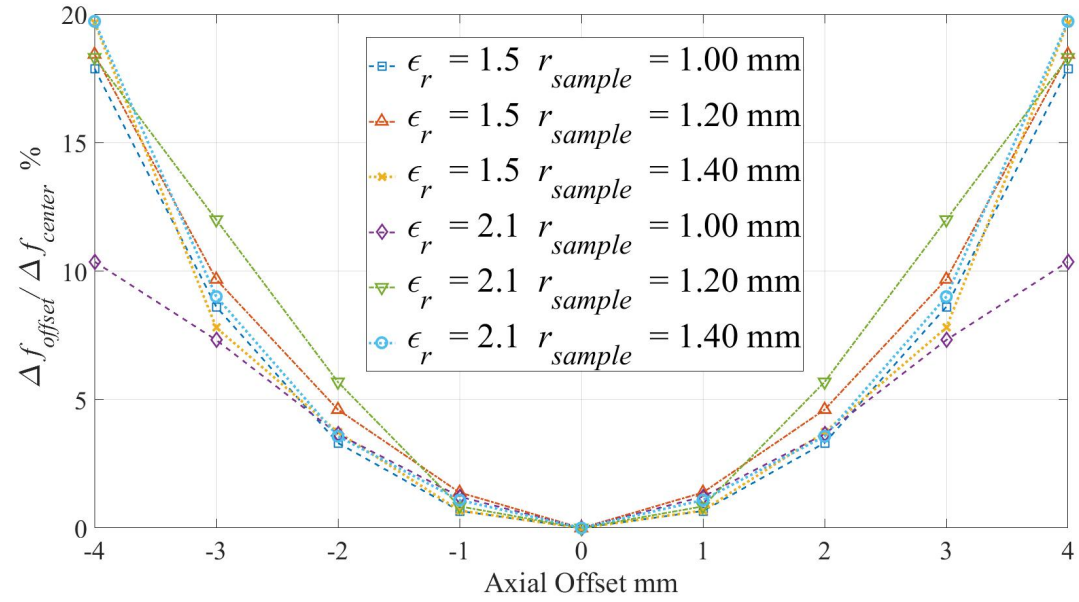


(b) Relative Frequency Deviation

Figure 2.10: Effect of Sample Offset in a Cavity with 5.5 mm Openings

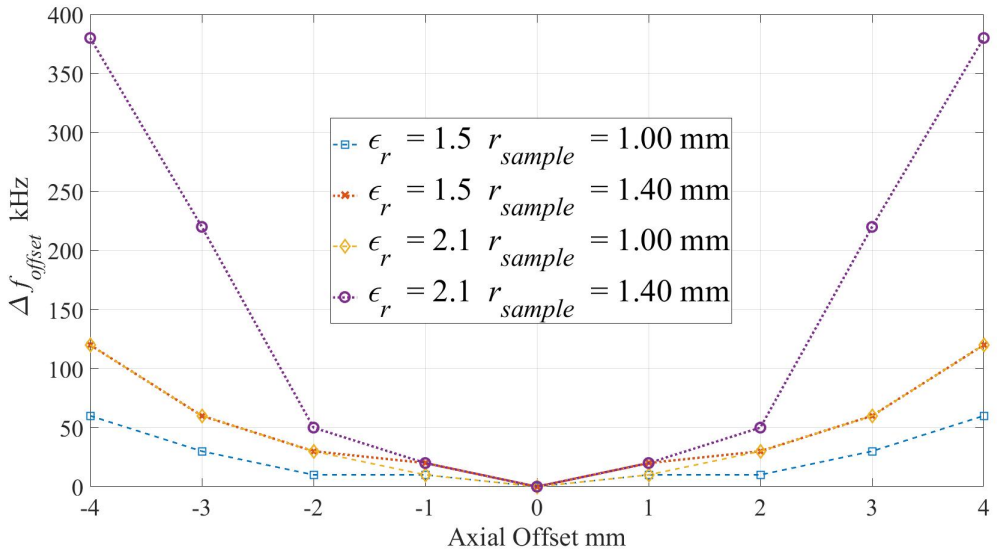


(a) Absolute Frequency Deviation

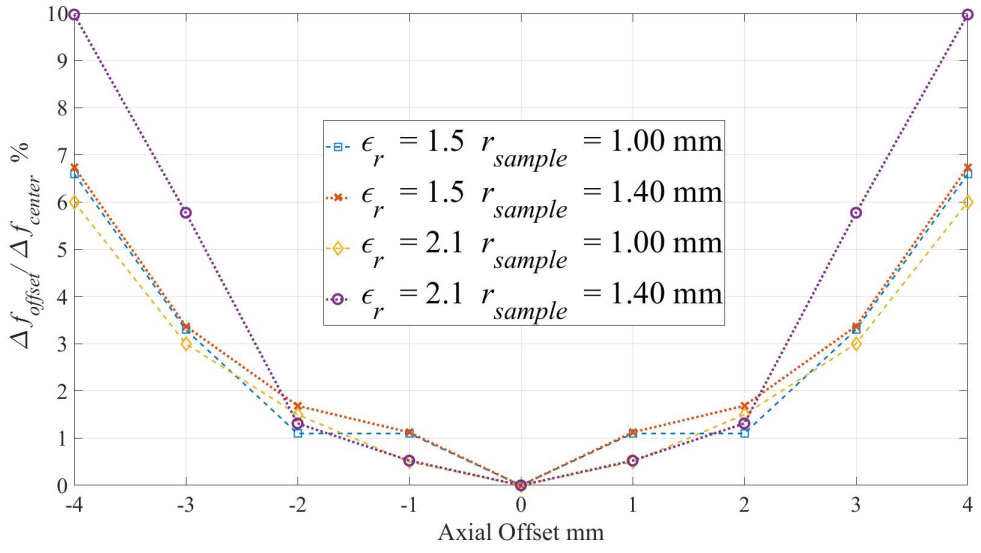


(b) Relative Frequency Deviation

Figure 2.11: Effect of Sample Offset for 30 mm Cavity Height

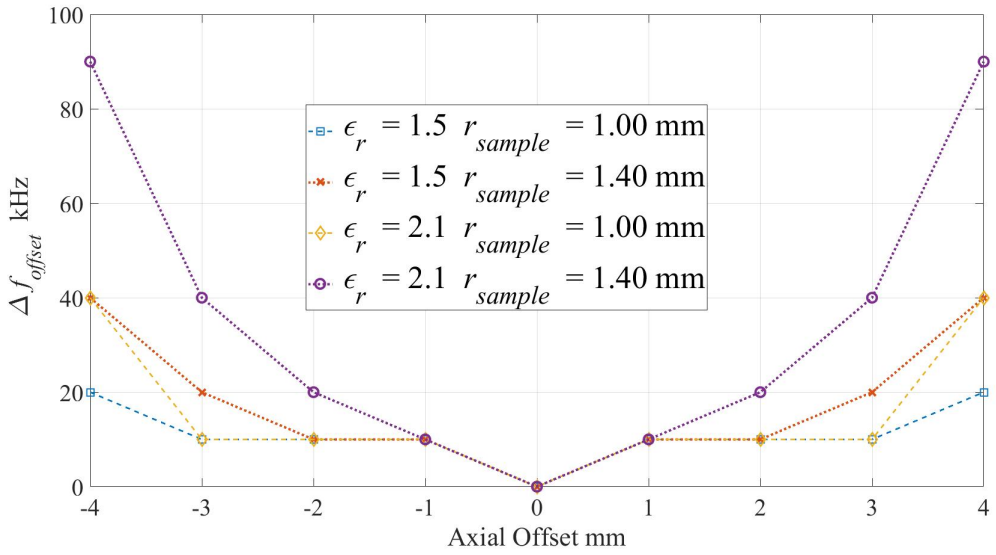


(a) Absolute Frequency Deviation

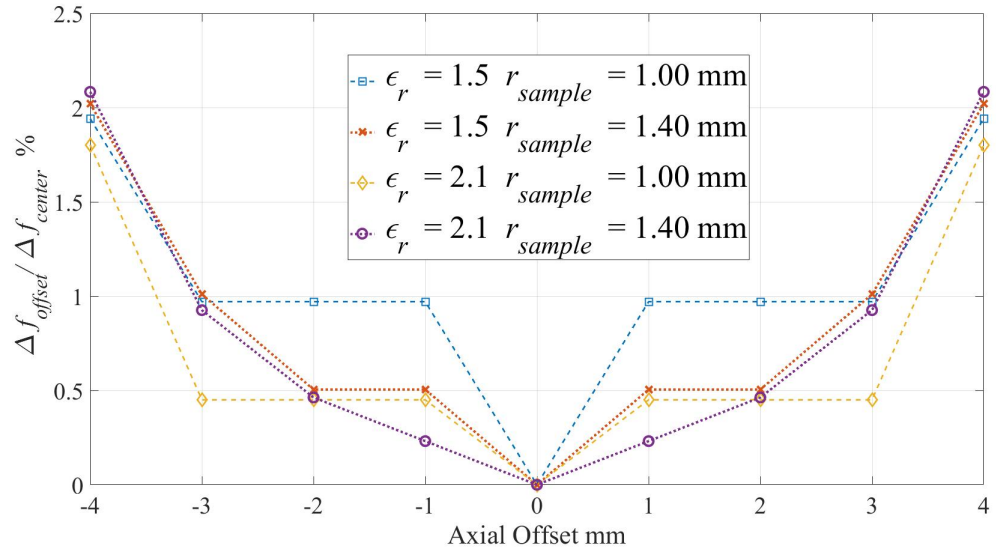


(b) Relative Frequency Deviation

Figure 2.12: Effect of Sample Offset for 60 mm Cavity Height

# 3 Solution I: Shaped Dielectric Inserts for Improved Field Homogeneity

This chapter provides a series of numerical simulations employed to improve the undesired detuning problem of the $TM_{010}$ mode cavity caused by sample position offsets during measurements. The objective of the proposed method of solution is to improve the average electric field homogeneity inside the sensing column without modifying the dimensions of the cavity resonator. As concluded in the preceding chapter, the relatively large and permanent openings of the sensing column on the top and bottom lids result in disturbing an otherwise predominately uniform electric field distribution. The field inhomogeneity can be attributed to the bending of the longitudinal electric field component, caused by the insertion holes, along the length or height of the cavity. Additionally, the presence of a relatively strong radial electric field component along the circumferential inner walls of the insertions holes increases the sensitivity of the resonance structure to sample movement away from the concentric axis. The effects of insertion holes in $TM_{0n0}$ cavity structures on the dielectric permittivity measure are discussed at length in a number of publications [Estin and Bussey, 1960; Meyer, 1977; Li and Bosisio, 1982; Gauthier et al., 1989]. The error terms for estimating the true dielectric permittivity of the sample are evaluated based on variational techniques involving summation of evanescent modes inside the openings. The error term compensates for the detuned frequency value caused by the insertion holes and improves the estimation for the measured dielectric permittivity value of the sample. However, while employing the cavity for measuring the thickness or the mass of the sample such error estimations are insufficient. The primary motive for sensing the thickness or mass of the dielectric sample using cavity techniques is to establish a space or volume wherein ideally the sample regardless of its localized placement exhibits exactly the same change in the resonance frequency, as elaborated in the problem definition of Sec.2.4.2.
In the context of the presented study related to the $TM_{010}$ cylindrical cavity, the measure of the electric field homogeneity refers to the overall strength and variations in magnitude of the longitudinal and the radial electric field components inside the sensing column. In addition, the ratio between the two orthogonal fields at various sub-volumes within the sensing column also serves as a measure of homogeneity. The so-called sub-volumes can be defined as unity radius columns which are employed as computation models for cylindrical samples. The unity columns simulate the effect of step-wise displacements of any cylindrical sample within the sensing column along the radial axis of the cavity. The solution approach to improve the homogeneity and reduce variations in magnitude is based on modifying the shape or more precisely the contour of the dielectric insert tube. An insert tube is primarily a protection tube usually employed to physically isolate the sensing column and the inner cavity region. The effects on the field concentration around and along the length of the insert tube are evaluated for a series of trials which comprise various contours of the dielectric insert. Instead of the commonly employed cylindrical tube insert, bi-conical tubes with contours of changing slopes are computed in the proposed approach. Each contour comprises an axially symmetric bi-conical insert tube with changing thickness values along the length of the tube.
The chapter presents the perspective of radial transmission lines to elaborate various underlying characteristics of the pill-box cavity. The discussion on radial lines provides the prime motivation for seeking a numerically computed fitting solution to address the inhomogeneity problem of the electric field. A detailed account on the significance of dielectric inserts follows the introductory section. It is followed by a discussion on various applied configurations of the inner and

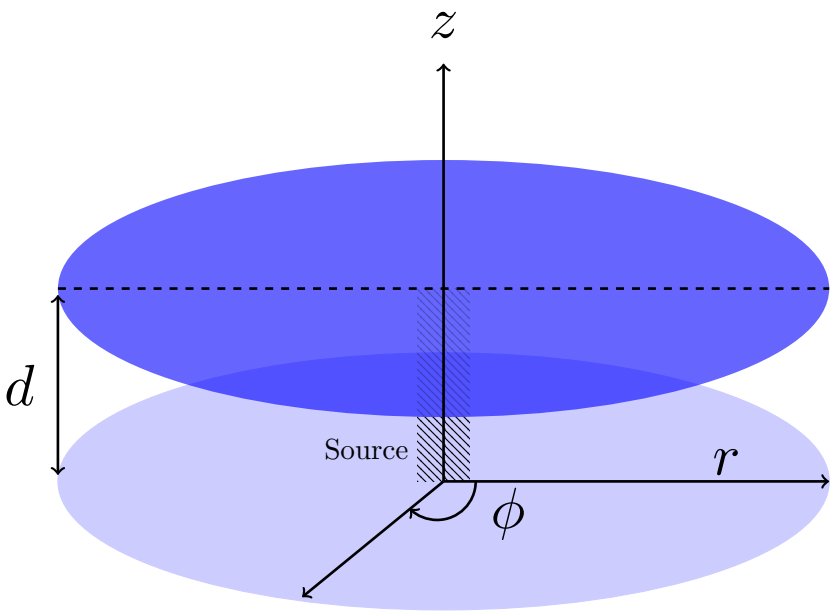


Figure 3.1: Radial Propagation

outer surfaces of the insert. These contours are simulated using the full wave simulation tool of CST [Computer Simulation Technology, 2017] to compute the effect of shaped insert tubes on the electric field homogeneity. Later sections present the computation mechanism of the sub-volume approach which is adopted to evaluate the electric field homogeneity for all the trial contour types of the insert. In the concluding section, one of the shaped insert tubes is shown to be chosen for fabrication and to perform measurements based on the simulated results. The measurements are undertaken for the shaped insert and compared to the commonly employed cylindrical tube in order to conclude the effectiveness of the proposed shaped dielectric insert solution.

## 3.1 Radial Waveguides

The pill-box $TM_{010}$ cavity so far discussed can also be viewed from the perspective of radial waveguides. In contrast to the planar equiphase surfaces in plane wave propagation, the radial waves are characterized by cylindrical surfaces of varying radii along the propagation path. These equiphase surfaces are given by $r$=constant planes as the wave travels inwards and outwards along the radial direction. In principle, a structure comprising two parallel conducting plates has the ability to support the phenomenon of radial propagation, as depicted in Fig.3.1, with a source illustrated at the axis for outward wave propagation. Radial waveguides belong to the category of so-called non-uniform transmission lines, where the nomenclature refers to the non-uniformity of cross sections which are transverse to the direction of energy propagation [Marcuvitz, 1986]. The cylindrical equiphase surfaces are similar yet not identical along the radial direction, although for large arguments of $r$ these values are identical to the plane wave functions. Therefore, far field radial waves can be approximated by uniform plane waves with a reduced amplitude along the path. In the context of the presented work the emphasis is rather laid on analysing the small argument approximations for the radial waveguides. Considering only transverse magnetic propagation with respect to the radial direction, the scalar mode potential function for the $TM^r_{nm}$ propagation in a parallel plate radial line, with $d$ as the separation distance between the plates, can be stated as

$$\psi^r_{nm}(z,\phi) = \mathrm{Z}(z)\mathrm{P}(\phi)\mathrm{R}(r), \tag{3.1}$$

where

- $\mathrm{Z}(z) = C_1 \cos(\frac{m\pi z}{d}) + D_1 \sin(\frac{m\pi z}{d})$ represents variations of the fields along the longitudinal direction, with $k_z = m\pi/d$.
- $\mathrm{P}(\phi) = C_2 \cos(n\phi) + D_2 \sin(n\phi)$ represents variations of the fields in azimuth, where $n$ are integer values due to the periodic nature of the solution in $\phi$.
- $\mathrm{R}(r) = A_1 \mathrm{J}_i(k_r r) + jB_1 \mathrm{N}_i(k_r r)$ represents the solution for radial variations as the complex sum of $i^{\text{th}}$-order cylindrical Bessel functions of first and second kind, respectively. The radial wave number $k_r$ for the parallel plate, with frequency dependent $k = \omega\sqrt{\mu\epsilon}$, can be expressed as

$$k_r = \pm\sqrt{k^2 - \Big(\frac{m\pi}{d}\Big)^2}, \tag{3.2}$$

where the sign will be chosen based on the condition that the real part stays positive, i.e. $\mathrm{Re}(k_r)>0$. Considering only $\mathrm{TM}_{0m}$ modes, the scalar mode potential can be simplified as

$$\psi^r_{0m} = C_1 \cos\Big(\frac{m\pi z}{d}\Big)\Big(A_1 \mathrm{J}_i(k_r r) + jB_1 \mathrm{N}_i(k_r r)\Big). \tag{3.3}$$

Limiting the case to the fundamental $\mathrm{TM}_{00}$ mode of the guide by setting $m = 0$, the longitudinal electric and the circumferential magnetic field distribution from the scalar mode potential in Eq.(3.3) can be deduced, while keeping $E_r = 0$ and $E_\phi = 0$ [Harrington, 2001],

$$E_z = \frac{1}{j\omega\epsilon}(\frac{\partial^2}{\partial z^2} + k^2)\psi^r_{00} = \frac{k^2}{j\omega\epsilon}\Big(\mathrm{J}_0(kr) + j\mathrm{N}_0(kr)\Big), \tag{3.4a}$$

$$H_\phi = -\frac{\partial\psi^r_{00}}{\partial r} = -k\Big(\mathrm{J}_1(kr) + j\mathrm{N}_1(kr)\Big). \tag{3.4b}$$

The $\mathrm{TM}_{00}$ mode is also referred to as the transmission line mode, as it can propagate energy due to a real mode impedance for the smallest possible radius values when compared to the wavelength. However, specifically for radial propagation the change of direction means a change in the impedance characteristics of the waveguide along the path. From Eq.(3.4) the impedance $Z^{00}_{+r}$ and $Z^{00}_{-r}$ of the $\mathrm{TM}_{00}$ mode along the radial line in outward and inward direction can be defined as [Harrington, 2001]

$$Z^{00}_{+r} = \frac{k}{j\omega\epsilon}\left(\frac{\mathrm{J}_0(kr) + j\mathrm{N}_0(kr)}{\mathrm{J}_1(kr) + j\mathrm{N}_1(kr)}\right), \tag{3.5a}$$

$$Z^{00}_{-r} = -\frac{k}{j\omega\epsilon}\left(\frac{\mathrm{J}_0(kr) - j\mathrm{N}_0(kr)}{\mathrm{J}_1(kr) - j\mathrm{N}_1(kr)}\right), \tag{3.5b}$$

respectively. It is to be noted that both the impedances at any specific radius looking forward and backward are complex conjugate of each other, i.e. $Z^{00}_{+r} = Z^{00*}_{-r}$. With longitudinal $E_z$ and circumferential magnetic field $H_\phi$, the $\mathrm{TM}_{00}$ or the so called parallel plate transmission mode is actually a TEM mode with reference to the radial $r$-axis. Therefore, it can be characterized by unique voltages and currents as a function of $r$ along the line [Marcuvitz, 1986],

$$\frac{dV}{dr} = jkZ_0 I, \tag{3.6a}$$

$$\frac{dI}{dr} = jkY_0 I, \tag{3.6b}$$

where the characteristic impedance and admittance for the $TM_{00}$ mode are defined as

$$Z_0 = \frac{1}{Y_0} = \sqrt{\frac{\mu}{\epsilon}} \frac{d}{2\pi r}. \tag{3.7}$$

In addition, similar to the classical transmission line model the radial line can also be expressed in terms of inductance and capacitance parameters, i.e. $L$ and $C$, as functions of the radial component $r$ for a given separation between the plates,

$$L = \frac{\mu d}{2\pi r}, \tag{3.8a}$$

$$C = \frac{2\pi r \epsilon}{d}. \tag{3.8b}$$

Due to the identical nature the $TM_{00}$ mode based transmission line section can be treated like a TEM waveguide. Nevertheless, there exists still the need to elaborate the discontinuity effects in such transmission lines, in view of the cavity resonator application.

### 3.1.1 $TM_{00}$ Cavity Resonator

The approach of radial transmission lines provides useful insight regarding the behaviour of the electric field distribution inside the opening region or the so-called sensing column of the cavity. A pill-box cavity formed by two parallel circular discs with opening in the center belongs to the category of structures which can also be analysed as a radial resonator, where the $TM_{00}$ mode is the dominant mode as depicted in Fig.3.2. The far end away from the axis of the cavity is identical to a short-circuited transmission line, whereas the near the axis end can be considered open-circuited. The open-circuit analogy can be drawn for both cases of with or without the insertion holes due to the exponentially high characteristic impedance of the radial line near the axis, as per Eq.(3.7). In view of Fig.3.2 which depicts the $TM_{00}$ radial cavity and Eq.(3.3), there are standing waves of different nature in both regions of the cavity marked by the lengths $a$ and $b$. Inside the cavity region, the radial wave number is real and equal to the frequency dependent wave number, i.e. $k_r = k = 2\pi/\lambda_g$, where $\lambda_g$ depends on the radial length of the short-circuited radial transmission line, explained in terms of impedance/admittance description in the next section (Sec.3.1.2). The discrete-valued transverse wave number with respect to the radial propagation is set to zero, i.e. $k_z = 0$, that is valid for a plate separation much less than the resonant wavelength $\lambda_g$ inside the radial guide. However, at the opening the radial waveguide representation loses its validity since there are no more parallel plates in that region. Moreover, the wave number $k_z$ is no longer discrete but tends to be continuous and imaginary. Similarly, $k_r$ also turns imaginary, resulting in evanescent fields in the sensing column. Neglecting the tube effects of the sensing column and considering only the inner core region of the column with the plate separation $d$, the transverse electric field $E_z$ has a radial dependence of a zero order Bessel function between the circular discs. Inside the sensing column region the electric field is defined using the modified Bessel function due to the imaginary argument values. The transverse dependence of the electric field is cosine trigonometric in the cavity and cosine hyperbolic due to an imaginary argument value of $k_z$, resulting in $E_z$ as function of $r$ and $z$, i.e.

$$E_z(a \leq r \leq b) \Rightarrow \mathrm{J}_0(k_r r)\cos(k_z z), \tag{3.9a}$$

$$E_z(0 \leq r \leq a) \Rightarrow \mathrm{I}_0(k_r r)\cosh(k_z z), \tag{3.9b}$$

which are applicable for the cavity description limited to only $TM_{00}$ mode excitation. For a completely closed radial cavity only Eq.(3.9a) is valid with $k_z = 0$, i.e. the transverse component with respect to the $r$ coordinate.
The boundary junction of $a$ and $b$ can be modeled as a connection of the radial waveguide and bounded free space region, i.e. similar to waveguides bounded in the H-plane but open at the

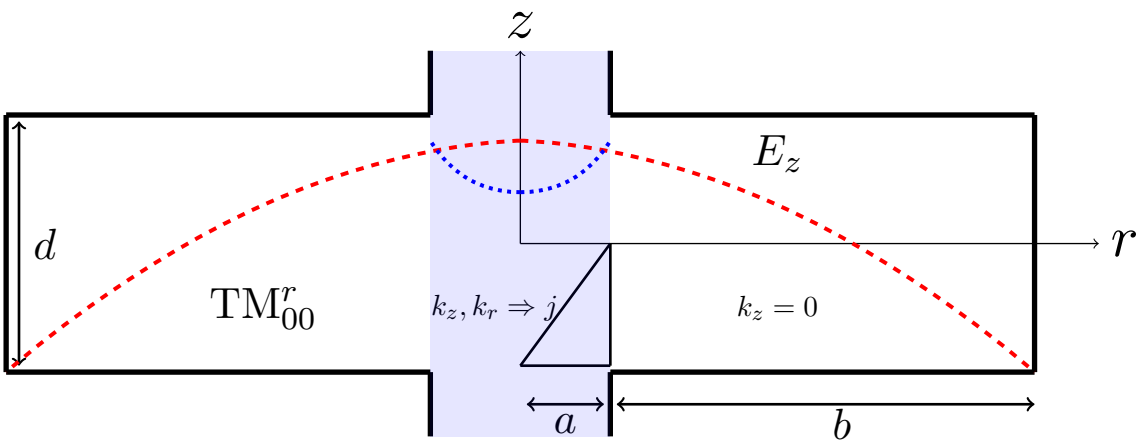


Figure 3.2: $TM_{00}$ Radial Cavity

E-plane (See Sec.4.6a Page 179) [Dicke and Purcell, 1948]. The estimation for the variations of the electric field along the $z$ direction inside the sensing column can be made with the help of the launching angle $\theta$, as depicted in Fig.3.3. The angle $\theta$ can be defined as the launching angle normal to the plane of the free space opening measured from the middle of the radial guide. The measure of $\alpha$ depends on half the opening length $a$ and half the radial cavity height $d/2$ forming a right-angled triangle, i.e. $\tan\theta = \frac{2a}{d}$. The value of $\theta$ estimates the variations along the cavity length due to the imaginary $k_z$ component with dependence on $\lambda_z = \lambda/\sin\theta$. It shows that the transverse variations along $z$ of a decaying electric field decreases for a greater plate separation or height of the cavity as well as for smaller insertion holes or openings inside the sensing column region, since the angle normal to the opening approaches zero for both cases of smaller opening and larger plate separation. Therefore, cavities with increased plate separation $d$ tend to suffer less from the electric field inhomogeneity in the channel. Hence, the estimation based on the right angled triangle explains the electric field distribution with its dependence on the spatial wave number $k_z$ inside the sensing region by using the radial waveguide approach in conjunction with the computational results of Sec.2.5.2.2. However, more qualitative insight is required regarding the solution to improve the electric field homogeneity. One key to understanding the problem and in finding a relevant solution lies in the impedance or admittance description of the radial lines.

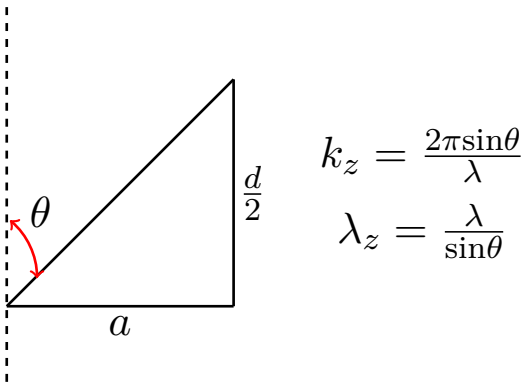


Figure 3.3: Estimation of $k_z$

### 3.1.2 Impedance or Admittance Description

The impedance description is a useful approach while treating transmission lines with discontinuities, as the concepts of uniform short and open circuited transmission lines can be employed to analyse the problem. The impedance/admittance description helps to analyse the behaviour of the radial lines and its effect on the resonance condition, stated as $Y_r = Y_l$, i.e. the impedance/admittance looking right and left at a certain reference plane on the line are equal. The admittance relation of a radial line can be stated in terms of the relative admittance which is the ratio of the admittance at a radius $r$ and the characteristic admittance $Y_0$ of the line, stated as $Y'(r) = Y(r)/Y_0(r)$). The relative admittance relation refers to the impedance at a radius $r$ from the perspective of another radius $r_0$. The relative admittance formula for a non-uniform radial transmission line can be expressed in terms of arguments $x = kr$ and $y = kr_0$ [Marcuvitz, 1986]

$$Y'(r) = \frac{j + Y'(r_0)\zeta(x,y)\mathrm{ct}(x,y)}{\mathrm{Ct}(x,y) + jY'(r_0)\zeta(x,y)}, \tag{3.10}$$

where

- $$\mathrm{ct}(x,y) = \frac{\mathrm{J}_1(x)\mathrm{N}_0(y) - \mathrm{N}_1(x)\mathrm{J}_0(y)}{\mathrm{J}_0(x)\mathrm{N}_0(y) - \mathrm{N}_0(x)\mathrm{J}_0(y)}$$
- $$\mathrm{Ct}(x,y) = \frac{\mathrm{J}_1(y)\mathrm{N}_0(x) - \mathrm{N}_1(y)\mathrm{J}_0(x)}{\mathrm{J}_1(x)\mathrm{N}_1(y) - \mathrm{N}_1(x)\mathrm{J}_1(y)}$$
- $$\zeta(x,y) = \frac{\mathrm{J}_0(x)\mathrm{N}_0(y) - \mathrm{N}_0(x)\mathrm{J}_0(y)}{\mathrm{J}_1(x)\mathrm{N}_1(y) - \mathrm{N}_1(x)\mathrm{J}_1(y)}$$

In order to model the cavity the short circuit placed at $r_0$ yields the relative admittance given by $Y'(r_0) = \infty$, as depicted in the Fig.(3.4). The input admittance of the short circuited line viewed from another radius smaller than $r_0$ can be derived from Eq.(3.10) by setting $Y'(r_0) = \infty$,

$$Y'(r) = -j\mathrm{ct}(x,y). \tag{3.11}$$

Similarly, the input admittance of the open circuited line viewed from any radial point larger than $r$ can be derived from Eq.(3.10) by setting $Y'(r_0) = 0$,

$$Y'(r) = j\mathrm{Tn}(x,y). \tag{3.12}$$

In comparison, the input admittance of a short circuited uniform transmission line of length $L$ is $Y_{sc} = -j\cot\theta$, whereas the open-circuited admittance is stated as $Y_{oc} = j\tan\theta$, with $\theta = kL$.

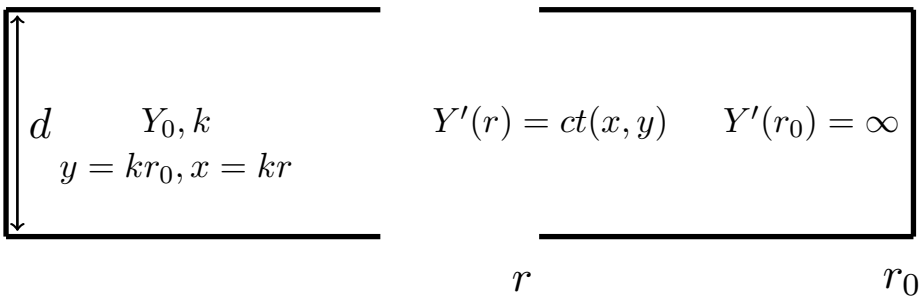


Figure 3.4: $TM_{00}$ Cavity Model

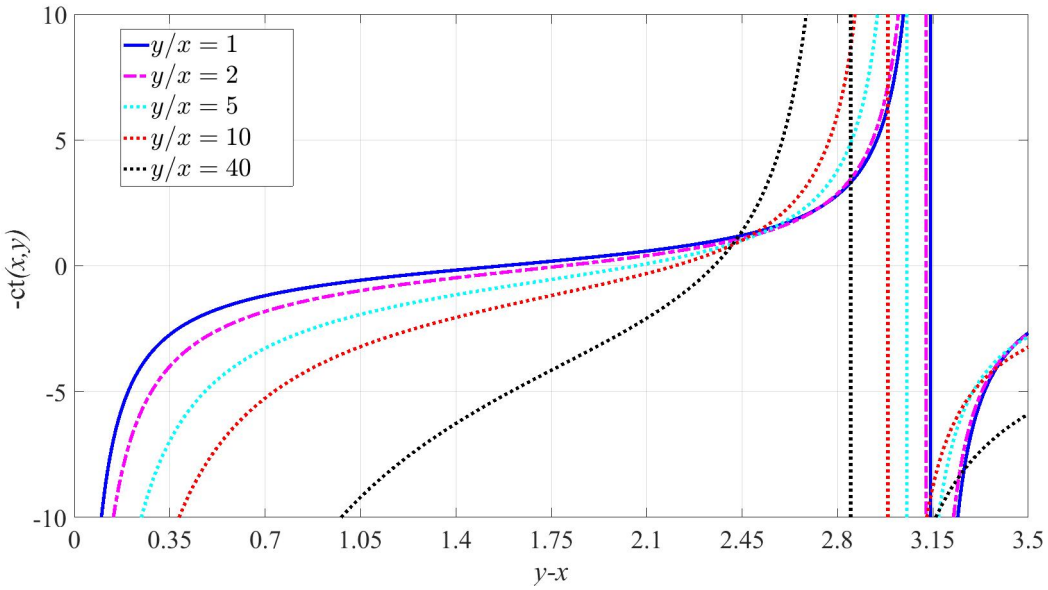


Figure 3.5: Relative Admittance of a Short-Circuited Radial Line $y/x > 1$

The plots of $\mathrm{ct}(x, y)$ and $\mathrm{Tn}(x, y)$ are shown in Fig.(3.5) and Fig.(3.6) which are plotted for $y - x = kr_0 - kr = 2\pi(r_0 - r)/\lambda_g$ and varying $y/x$ ratios. From the plots it is evident that the radial transmission line or the so called non-uniform transmission line has compressed cotangent and tangent functions for $kr << 1$. For larger values of $kr >> 1$ the behaviour of the radial line approaches that of the the uniform transmission line. The property of compression of the radial line at small radial distances can be employed to improve the electric field homogeneity by qualitative testing of dielectrics of various shapes and contours placed adjacent to the sensing column or the opening.

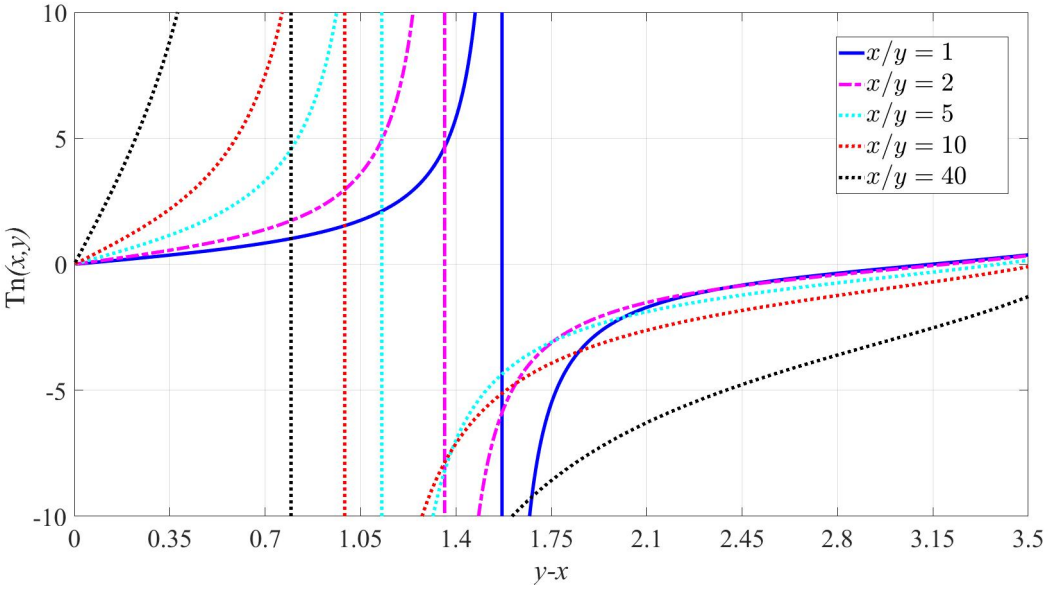


Figure 3.6: Relative Admittance of an Open-Circuited Radial Line $y/x < 1$

## 3.2 Dielectric Inserts

It is a well-established practice that in $TM_{010}$ mode operated cylindrical cavities the central concentric sensing column provides the interaction space for the placement or passage of samples under test. In most cases, the external surroundings to the cavity resonator are contaminated due to the presence of varying degrees of humidity, dirt and dust particles. Exposure of the inner cavity volume to such contaminated environments causes unaccounted detuning of the cavity sensor. Additionally, the material under test may not necessarily be a bulk and hardened solid. For example, the material composition can also consist of mild or softer tissues like textile fibres of cotton or wool threads. Such softer materials undergo loss of particles particularly while passing through the sensing region. As a consequence, the accumulation of stray particles from the sample can occur inside the resonator body over a longer period of time. Therefore, additional design features in the form of a protection boundary or a cylindrical ring shaped enclosed periphery wall are usually essential in such cases. In terms of application, such type of problem is similar to the characterization of liquids where the sample has to be filled inside a glass or a quartz capillary tube. In order to physically isolate and hermetically seal the inner cavity volume, low loss dielectric tubes are fixed around the sensing column, similar to the idea of a capillary tube holder for liquid samples. In practice, a thin dielectric insert is mounted inside with the help of an adhesive element such as epoxy resin to the upper and bottom lid portions of the cavity.
In view of the admittance behaviour of the radial cavity, two admittance models for the dielectric insert are illustrated in Fig.3.7. The abrupt height change in cavity plates separation $d'$ due to a cylindrical dielectric insert of relative permittivity $\epsilon_r$ adjacent to the opening against the gradual change $d''$ due to shaped insert of identical permittivity are depicted in Fig.3.7a and Fig.3.7b, respectively. It is noteworthy that the illustrated change in the plate separation is effectively due to the change in relative permittivity of the dielectric insert. The effective change in plate separation $d'$ for the cylindrical insert is directly related to the change in $\epsilon_r$. On the other hand, the effective change in height $d''$ is a function of the radial length $\Delta r$ measured from the point $r$ towards $r'$ in case of the shaped dielectric. Furthermore, the change in relative characteristic admittance is effectively a function of the change in plate separation due to the increased permittivity $\epsilon_r$ of the radial cavity as per Eq.(3.7), this can be stated as [Marcuvitz, 1986]

$$\frac{Y_0'}{Y_0} = \frac{d}{d'}, \tag{3.13a}$$

$$\frac{Y_0'}{Y_0} = \frac{d}{d''}, \tag{3.13b}$$

for cylindrical and shaped inserts, respectively. The effect of gradual variation of plate separation instead of the abrupt reduction due to the placement of the insert is numerically investigated by simulating different shapes and contours of dielectric inserts. Figure 3.8 depicts perspective as well as cross-section views of a cylindrically symmetrical insert tube isolating the sensing column from the inner cavity volume. Furthermore, Fig.3.9 illustrates some other examples of shaped insert tubes whose influence on the electric field homogeneity is computed during the course of the presented work.

### 3.2.1 Material Selection

The material of the insert tube should possess certain mechanical, chemical, electrical and thermal properties while being employed in sensing and measurement applications. Mechanical attributes such as a specific measure of hardness, density and tensile strength are required for fabrication into various axially symmetric thin tubes. Chemical properties like higher degrees of purity, resistance against corrosion and low absorption of water molecules are equally necessary.

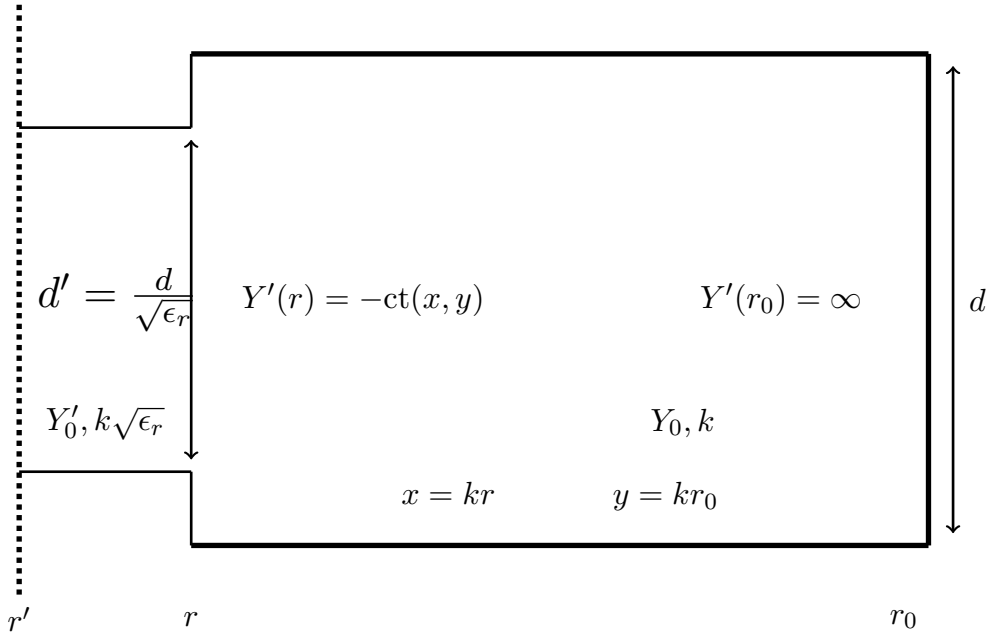


(a) Cylindrical Dielectric Insert Model in Radial Cavity

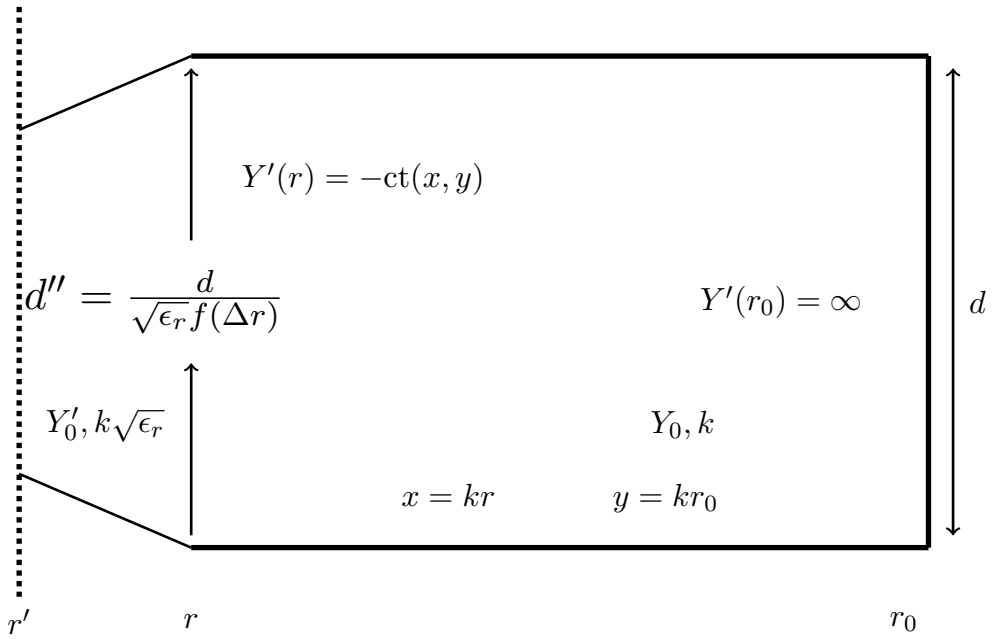


(b) Shaped Dielectric Insert Model in Radial Cavity

Figure 3.7: Admittance Models for Dielectric Inserts Adjacent to the Opening

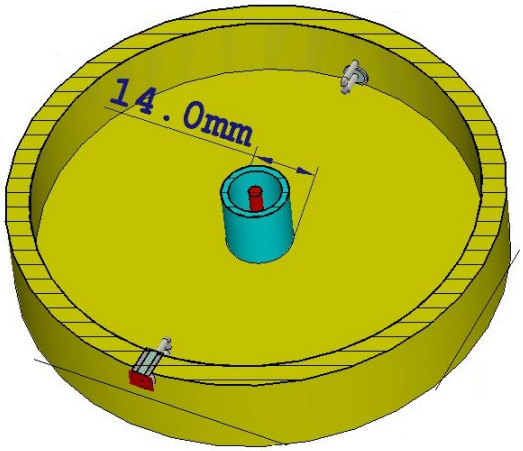


(a) Perspective View

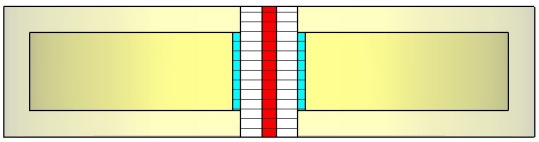

(b) Crossection View

Figure 3.8: Cavity with 1.5 mm thick Insert Tube and Sample

Moreover, the insert material should be electrically low loss in order to have a reduced dissipation and minimal drop in the overall quality factor of the cavity. In addition, a low coefficient of thermal expansion and high abrasive resistance are also desired attributes of the material used for insert tubes. Mostly, the insert tubes are made from Quartz, owing to its fitting characteristics. Nevertheless, plastics like Teflon as well as other ceramic inserts are also utilized, whenever necessary for the application.

The computation scheme presented here evaluates the effects of two different insert materials, namely, Quartz glass and Alumina ceramic. Both material types differ in their permittivity values, where the latter has a real permittivity value of three times the value of the former. The choice of two different materials is made to simultaneously compute the impact of the shape of the insert in conjunction with the influence of permittivity variations on the homogeneity of the electric field inside the sensing column. Following is a brief summary of the most significant properties which aided the selection criteria of both Quartz and Alumina:

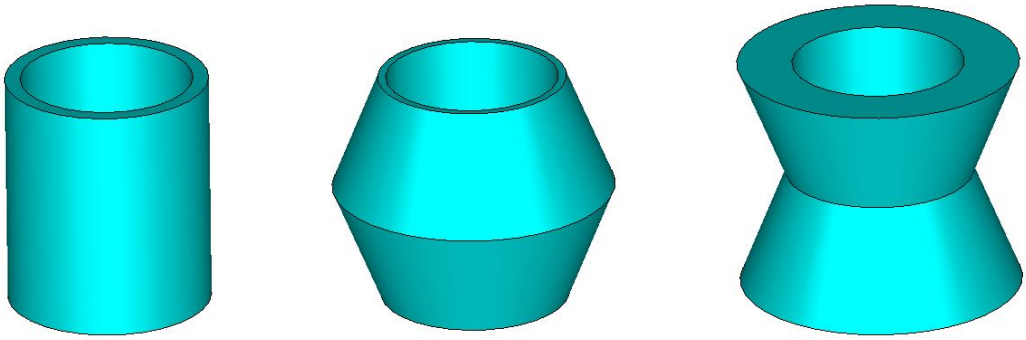

(a) Cylindrical (b) Bi-conical Type A (c) Bi-conical Type B

Figure 3.9: Three-Dimensional View of Insert Shapes

1. Quartz is commercially available in a number of grades depending on the impurity levels and the specific process undertaken for its industrial production [GE Data, 2017]. Due to its purity and suitability to microwave and millimeter wave applications, it is widely used in semi-conductor wafer processing and production of fiber optic cables. The source of the material is Silica sand which can be chemically melted and processed into either crystalline or non-crystalline structures depending on the method of treatment. The crystal structure yields translucent appearance called the fused Quartz, whereas the other synthetically derived opaque material is termed fused Silica. Both the traditional flame and the modern electric fusion methods are used for manufacturing at industrial scale [Helios Quartz, 2017]. A batch process is carried out by placing the raw material in vacuum chambers to be heated into molten form, which is a suitable method for high yield and larger shapes. In a high purity electric fusion method, Quartz sand is filled in a metal crucible and subsequently heated using electrical filaments. The melted glass is collected from the bottom of the crucible and shaped into tubes, rods or plates. Generally, a translucent end product is obtained through this process. Another method called sintering, that requires heating under high compression without liquefaction, is also used to convert powdered Quartz into white non-transparent appearance solid shapes [Heraeus Quarzglas, 2017].

   Quartz exhibits excellent electric insulation and microwave transmission properties over a wide range of frequencies. In addition, it can withstand extended working temperatures due to its temperature stability and a high melting point (approximately 1200° C). Moreover, the resistance against abrasion and corrosion is also superior which makes it an ideal choice for the use as a dielectric insert in cavity resonators. Special care must be taken while cleaning translucent tubes because the water and acid solutions may penetrate into the capillaries of the translucent material. However, under ambient surroundings it has low moisture absorption capabilities. Consequently, fused Quartz is chosen for its extremely low dielectric losses with moderate permittivity, i.e. $\tan\delta = 4 \times 10^{-4}$ and $\epsilon_r = 3.75$.

2. Aluminium oxide ($Al_2O_3$) or simply Alumina is one of the ceramic materials found in abundance. It is equally a fitting choice in various engineering applications due to its chemical and thermal stability, relatively good mechanical strength, as well as electrical insulation characteristics. It also is available in various grades depending upon the amount of impurities and some deliberate alloying agents such as sintering aids. Above 80% purity are usable grades of Alumina for microwave applications, though the 99% is the purest and highest grade Alumina.

   In terms of dielectric properties, Alumina has a loss tangent similar to that of Quartz material, whereas the electric permittivity of $\tan\delta = 4 \times 10^{-4}$ and $\epsilon_r = 9.1$. It is an extremely non-porous material with very low moisture absorption tendency. The strength of Alumina is a function of the manufactured size volume or surface area. The smaller the volume, the lesser is the stress it can withstand. It is to be noted that the primary motivation for the selection of Alumina as the alternate to Quartz was to provide a reference for comparison regarding influence of higher dielectric permittivity during the computation.

### 3.2.2 Shape Modifications

Introducing a dielectric tube or a sample holder inside the cavity resonator results in additional boundary surfaces, as discussed in Sec.2.1.3. The solution for the electric field inside the cavity resonator should match at the surface of the dielectric interface. Consequently, the overall electric field concentration inside and outside the dielectric insert modifies as a function of the surface orientation and its dielectric properties. In order to take advantage of this concept of

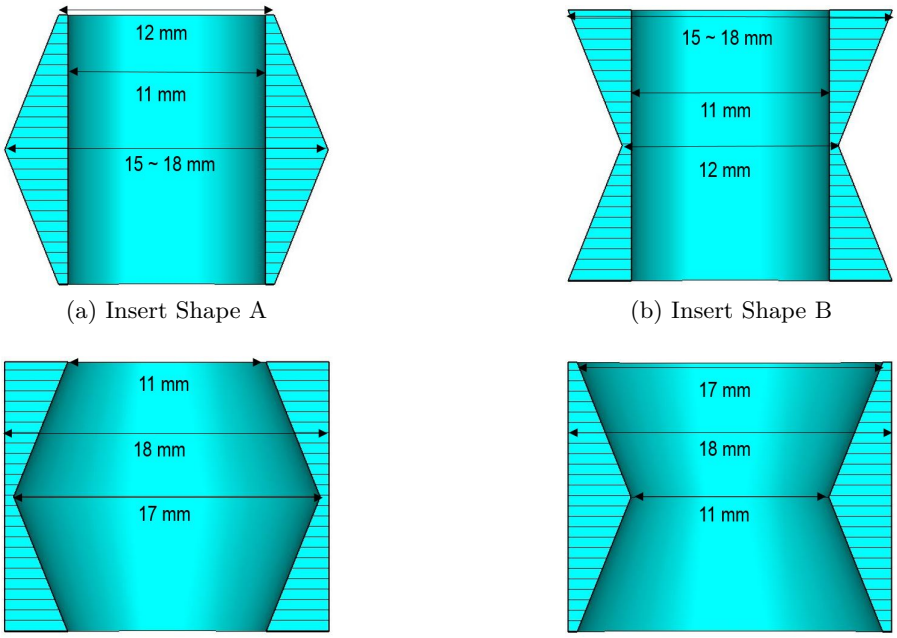


(a) Insert Shape A

(b) Insert Shape B

(c) Insert Shape C

(d) Insert Shape D

Figure 3.10: Cross-sections of Employed Insert Shapes

changing radial impedance along the radius and the subsequent influence on the electric field homogeneity a scheme of varying shape inserts is employed. It comprises a combination of bi-conical shaped dielectric inserts with varying degrees of steepness forming contour surfaces. For a cylindrical tube the variations along the whole length of the tube are uniform. Bi-conical refers to the variations in the thickness of the tube along the length of the sensing column with reference to the axial center. A set of certain geometries are chosen for shapes of the insert tube that have a different tube thickness values at the center and at the opening joint. The idea is to compute the extent to which the electric field behaviour responds to variations in changing thickness values of the insert tube along the length of the sensing column. The shape and symmetry of the dielectric insert were optimized while attempting to keep the Q-factor intact for the given operation frequency range. Hence, a thicker dielectric insert was avoided as it causes relatively reduced quality factor and as a consequence reduced capability to sense/measure actual mass changes particularly in low permittivity samples. Figure 3.10 demonstrates the types of profiles employed as candidates for a dielectric insert which are all bi-conical in shape. Type A and B shapes have a conical profile on the outer surface of the tube, whereas the other two types termed the Type C and D have variations on the inner surface of the tube.
Table 4.1 provides detailed account about the variations in the thickness of all the simulated insert tubes. Alpha-numeric nomenclature is used in the table, where the alphabetical characters relate to the type of contour modification on the inner or outer surface. In addition, the numeric characters represent the thickness of the insert tube corresponding to each type of contour. All the shaped tube inserts are computed and compared with the cylindrical insert tube.

## 3.3 Computation Results

### 3.3.1 Computational Scheme

The evaluation of the electric field distribution is performed with the help of horizontal computational lines available in the CST-Microwave Studio model creation environment [Computer

Table 3.1: Dielectric Insert Profiles and Dimensions

| Shape | Center Dimensions mm | | Opening Dimensions mm | |
|---|---|---|---|---|
| - | Inner Radius | Outer Radius | Inner Radius | Outer Radius |
| Reference | 5.5 | 6.5 | 5.5 | 6.5 |
| Type A1 | 5.5 | 7.5 | 5.5 | 6.5 |
| Type A2 | 5.5 | 8.0 | 5.5 | 6.0 |
| Type A3 | 5.5 | 9.0 | 5.5 | 6.0 |
| Type A4 | 5.5 | 15.0 | 5.5 | 6.5 |
| Type B1 | 5.5 | 6.5 | 5.5 | 7.5 |
| Type B2 | 5.5 | 6.0 | 5.5 | 8.0 |
| Type B3 | 5.5 | 6.0 | 5.5 | 9.0 |
| Type B4 | 5.5 | 6.5 | 5.5 | 15.0 |
| Type C1 | 8.5 | 9.0 | 5.5 | 9.0 |
| Type C2 | 10.5 | 11.0 | 5.5 | 11.0 |
| Type D1 | 5.5 | 9.0 | 5.5 | 8.5 |
| Type D2 | 5.5 | 11.0 | 5.5 | 10.5 |

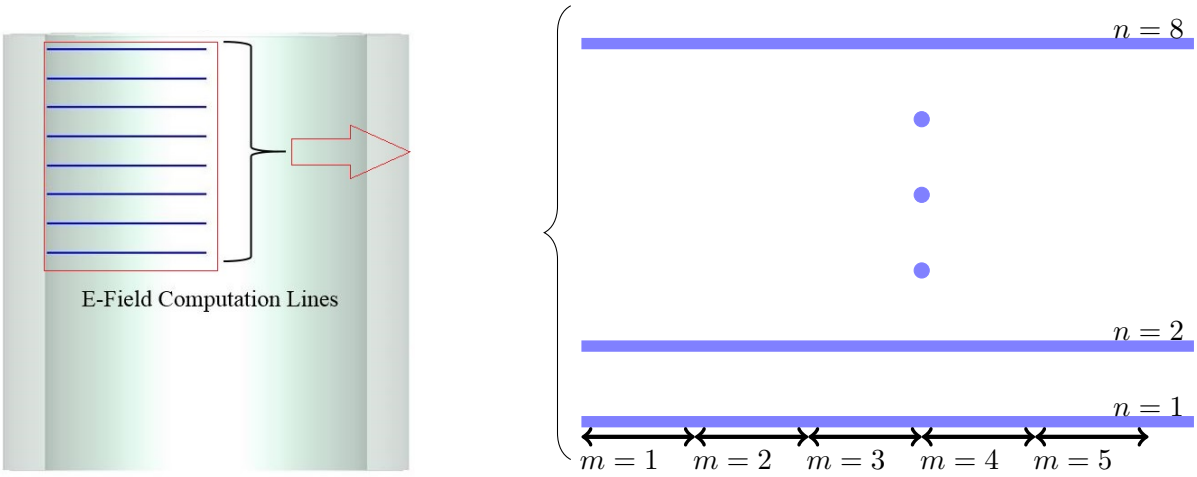


Figure 3.11: Computation lines along the Sensing Column

Simulation Technology, 2017]. The lines are placed in a vertical arrangement 1 mm apart from the center of the cavity towards the opening covering half the length of the symmetric sensing column, as depicted in Fig.3.11. Each line computes the electric field in a linear stepwise manner by dividing each line into five segments, hence modeling a cylindrical sample of 1 mm radius moving away in steps of 1 mm from the center. Electric field components of longitudinal and radial nature are evaluated along each line for all combinations of the dielectric insert given in the Table 3.1. Since the sensing column has an axial and lateral symmetry only one quarter space, representing the cross section area of the sensing column, is sufficient to estimate the variations in the value of the electric field components. The value of the electric field is computed across each line denoted by $n$ that are numbered vertically from 1 to 8, with a step of 1 mm. Each computational line is further divided into five equal sections denoted by $m$, that are numbered from 1 to 5. All field points within each $m$ segment on each $n$ horizontal line are summed into a root mean square term along the whole line length across the sensing column. Subsequently, the electric field for each column of all the five adjacent unity columns is numerically estimated by adding the contribution from eight lines segmented into five steps each representing a specific column position.

In this scheme of field summation and averaging, the value across the column radius are root

mean squared whereas the average sum is taken along the column height. The root mean squared summation values along the $n$ horizontal computational lines are stated as

$$(|E_{ij}|_k)_{RMS} = \left[\frac{1}{N_{samples}} \sum^{\Delta r} (|E_{mj}|_k)^2\right]^{\frac{1}{2}}, \tag{3.14}$$

where $i = 1$ to 5 and $j = 1$ to 8, i.e. eight computation lines along the length of the sensing column, with each line divided equally into five sections of $\Delta r = 1\,\text{mm}$ length. Each section length represents the placement column or the place holder for the sample. The RMS value obtained for each section length on each computation line yields a $8 \times 5$ matrix. Similarly, for taking the average sum of the electric field the following scheme of addition was used

$$(|E_k|^{ij})_{RMS} = \begin{bmatrix} E_{11} & E_{12} & E_{13} & \dots & E_{15} \\ E_{21} & E_{22} & E_{23} & \dots & E_{25} \\ & \dots\dots\dots\dots & & & \\ E_{81} & E_{82} & E_{83} & \dots & E_{85} \end{bmatrix} \Rightarrow \sum_{j=1}^{j=8} \Rightarrow \begin{bmatrix} E_{00} & E_{01} & E_{02} & E_{03} & E_{04} \end{bmatrix}. \tag{3.15}$$

The overall normalized electric field quantity for the longitudinal as well as the radial component can be expressed as

$$(|E_k|_{1\times 5})_{Normalized} = \frac{\begin{bmatrix} E_{00} & E_{01} & E_{02} & E_{03} & E_{04} \end{bmatrix}.}{E_{00}} \tag{3.16}$$

It is validated from the computations that the electric field inhomogeneity can be attributed to the presence of two major components of the electric field, namely, the radial $E_r$ and the axial or longitudinal electric field $E_z$. The normalized magnitude of each of the electric field components is shown to be dependent to a certain degree on the contour and shape profile of the dielectric insert. Figure 3.13 depicts the cases of the column-wise electric field distribution of a totally enclosed $\text{TM}_{010}$ cavity along the cavity with insertion holes of radius 5.5 mm, by implementing the above elaborated computational lines scheme. The results for the closed cavity in Fig.3.13a show the normalized longitudinal electric field slightly reducing in strength in accordance with the zero order Bessel function $\text{J}_0(k_r r)$ along the radius. In contrast, the open cavity in Fig.3.13b shows the incremental longitudinal electric field away from the axis under the openings. The increment is a result of the column opening causing a localized standing wave of the longitudinal electric field decreasing towards the center as per the modified Bessel function $\text{I}_0(k_r r)$. In addition, the increment of the normalized radial component of the electric field away from the axis is also evident in the illustration caused by the presence of $E_r$ with dependence on modified Bessel function of the first order, i.e. $\text{I}_1(k_r r)$. It is to noteworthy to mention that the radial field is largely influenced by the distance to the inner walls of the insertion holes.

### 3.3.2 Field Homogeneity and its Effects on Frequency Detuning

The comparison in terms of normalized field distribution is shown for the types of contours of the tube inserts, as outlined in the Tab.3.1, are provided in Figs.3.14, 3.15, 3.16, 3.17. The cylindrical tube references are presented in each graph with each pair of complementary tubes, i.e. the pairs with similar slope variations of the conical surface along the length. As an outcome of the numerical measure of normalized electric field components in the sensing column, the A1 type quartz bi-conical structure was found to be most suited for a relatively homogeneous electric field distribution. Figure 3.18 shows the effect of variations on the longitudinal electric field components for both cylinder and bi-conical insert labelled as type A1. The latter insert type shows relatively flat field distribution across the sensing column besides reduced variations

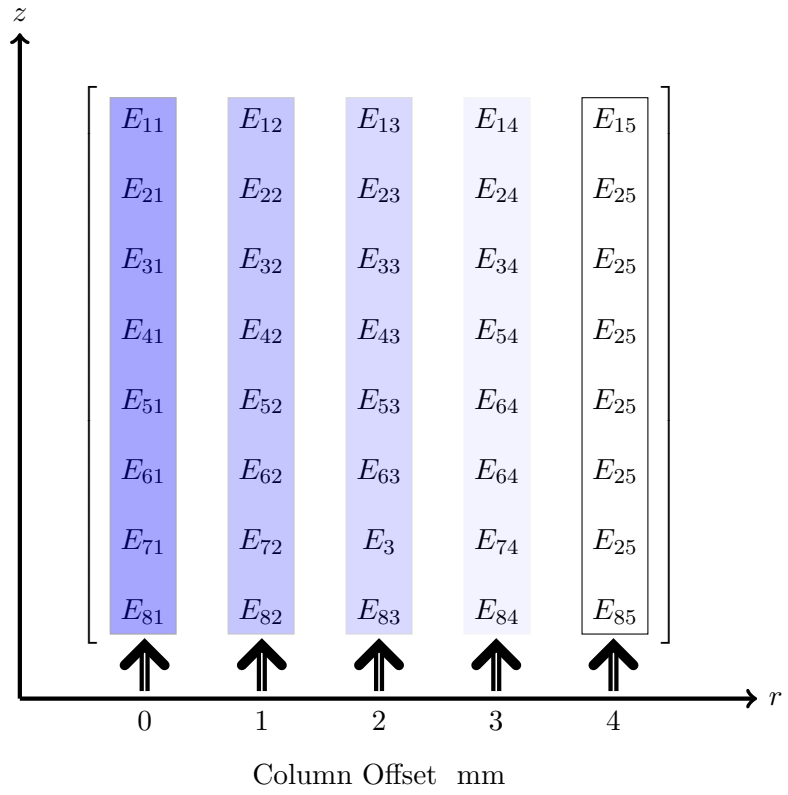


Figure 3.12: Average Summation of the Electric Field along Column Height

along the column length. The improvement can be attributed to the outer contour or slope of the bi-conical insert. The thicker in the middle and thinner at the opening profile of the insert tube ensures a reduction of the electric field in the center of the cavity in comparison to the top and bottom of the cavity. Hence, the effect of the insert tube on the field distribution is opposite to that due to the openings of the insertion hole.

## 3.4 Measurement Prototype

In order to verify some of the most significant results from the number of computations illustrated in the previous section, there arises the requirement to built prototypes for the inserts. Among the computed shapes, one with an improved electric field homogeneity, the so-called A1 profile, was chosen for fabrication. The comparison of the selected insert shape was performed with the standard cylindrical insert, as pictured in Fig.3.19. The choice of the insert selected for the prototype was also governed by the ease of fabrication and the rapid availability of the material. In addition, both the cylindrical and the biconical inserts are made from Quartz material which provides a better measure for comparing only the effects of surface contours on the electric field homogeneity.

### 3.4.1 Measurement Setup

- The design specifications of the cylindrical cavity resonator are similar to those mentioned in Sec.2.5.1, which was milled using brass metal by utilizing two different blocks of the metal, which are later attached with screws along the periphery of the two cavities. This detachable structure helps the placements of dielectric fixtures inside the cavity. The provision for insertion holes in the middle of the cavity was also provided for the sample

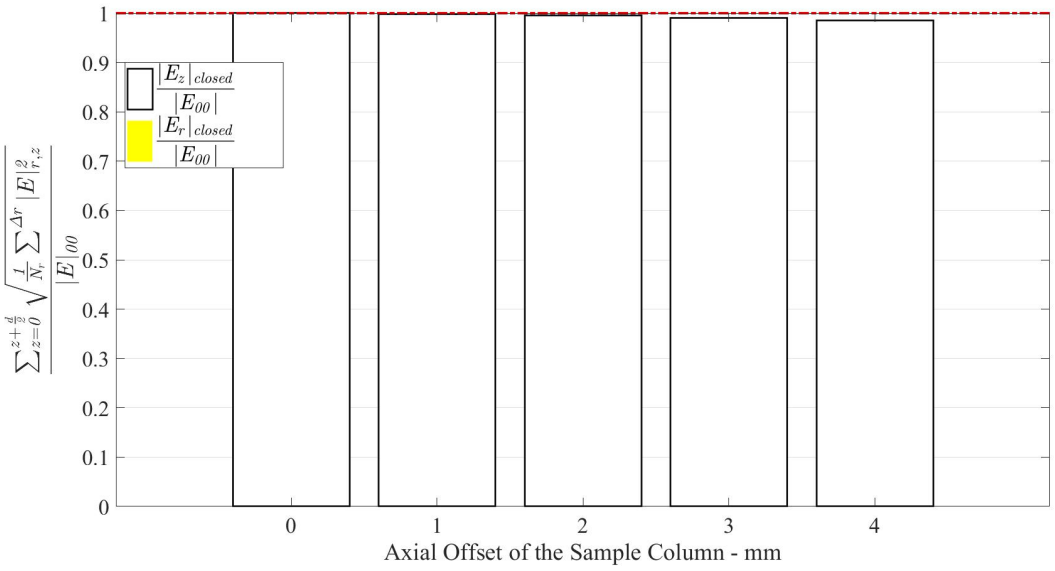


(a) Closed Cavity

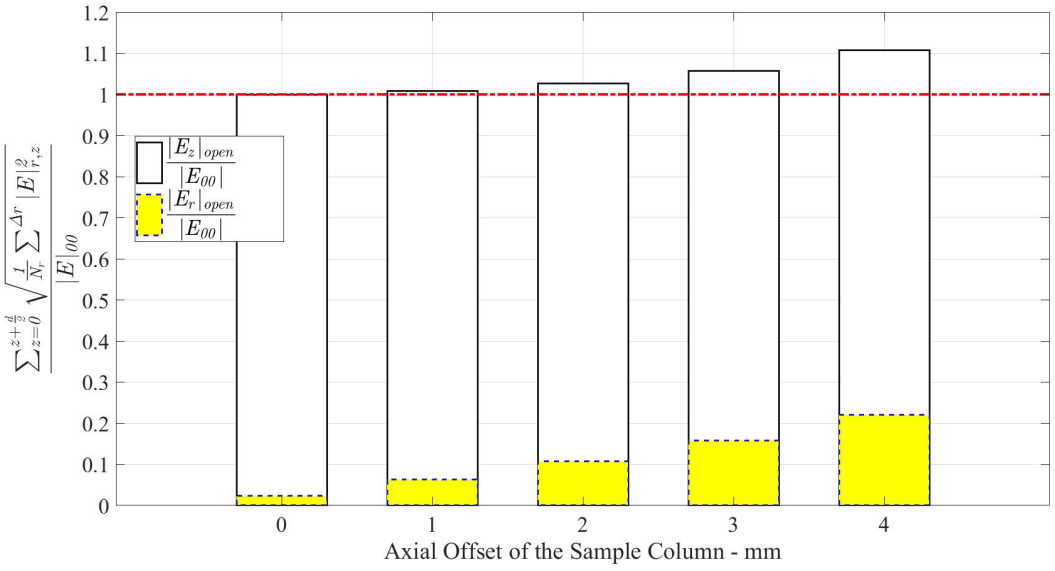


(b) Cavity with 5.5 mm Radius Insertion Holes

Figure 3.13: Normalized Normal and Tangential Field Variations along the Computation Lines inside the Sensing Column

flow.

- Dielectric insert tubes made of Quartz glass with both biconical and cylindrical shaped prototypes are employed for testing. The cylindrical tube has a uniform thickness of 1.5 mm, whereas the biconical tube is slimmer 1.0 mm toward the edges and gets thicker 2.0 mm thick at the center. Both shaped profiles were fitted in the cavity resonator turn by turn to perform the measurement of frequency detuning due to the sample offset movements.

- An important and significant part of the experiment comprised the mounting assembly provided with a platform for the cavity fixture and a spring loaded thin nylon thread to

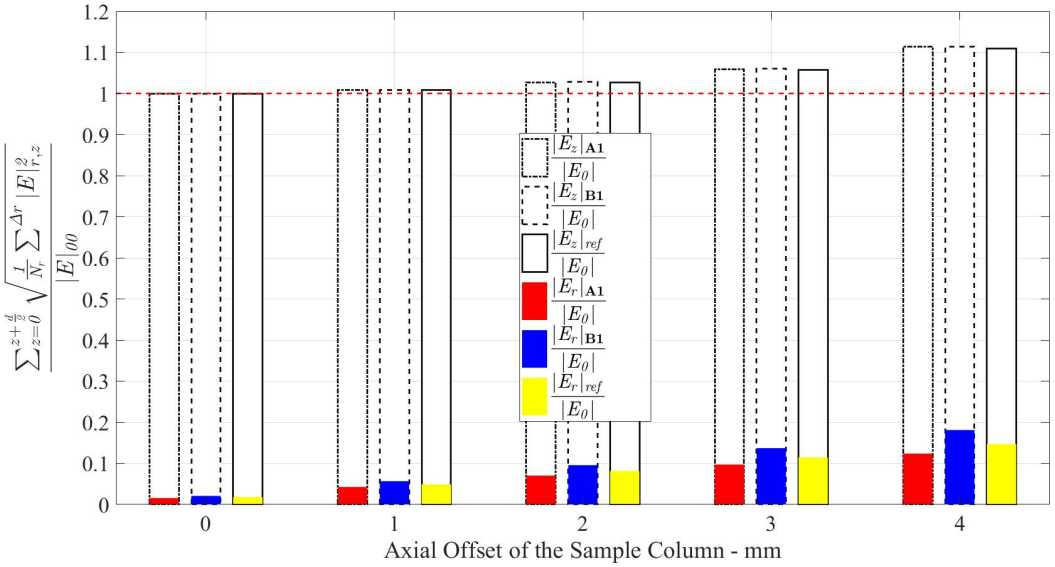


(a) Quartz Insert - A1 and B1 Profiles

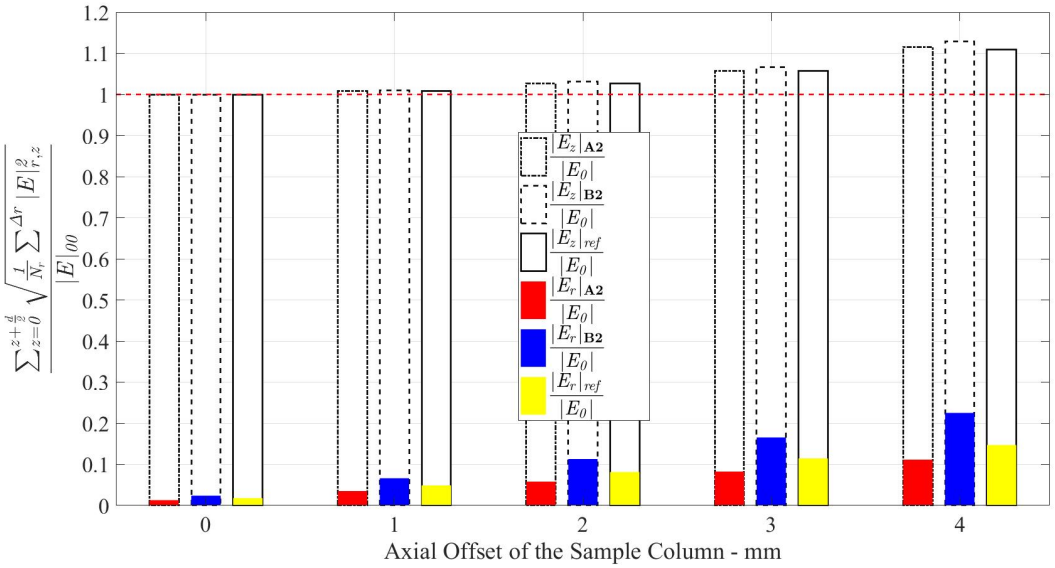


(b) Quartz Insert - A2 and B2 Profiles

Figure 3.14: Comparison of Normalized Normal and Tangential Field Variations along the Computation Lines inside the Sensing Column

hold the FEP (Fluorinated Ethylene Propylene) dielectric tubes as the common measurement sample for both types of inserts, as shown in Fig.3.20. The spring loaded nylon thread holding the concentric sample tube is attached to a micrometer assembly. When rotated, it causes the sample to move inside the sensing channel from the center toward the edges of hole, hence generating the case of sample lateral movement.

- The measurement setup consisted of a vector network analyzer to record the transmission coefficients of the two-port cavity. The cavity was mounted on a customized built structure of an assembly frame. The mounting frame provided a means to attach single or multiple textile fibers or threads through a spring loaded mechanism connected to a micrometer gauge. A single thread passing from top to bottom through the cavity can be aligned

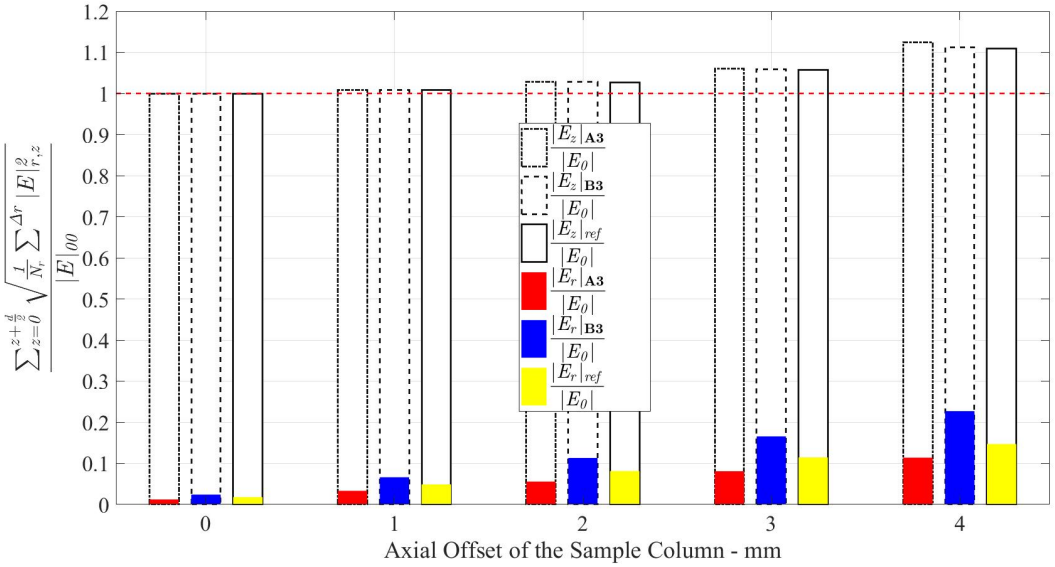


(a) Quartz Insert - A3 and B3 Profiles

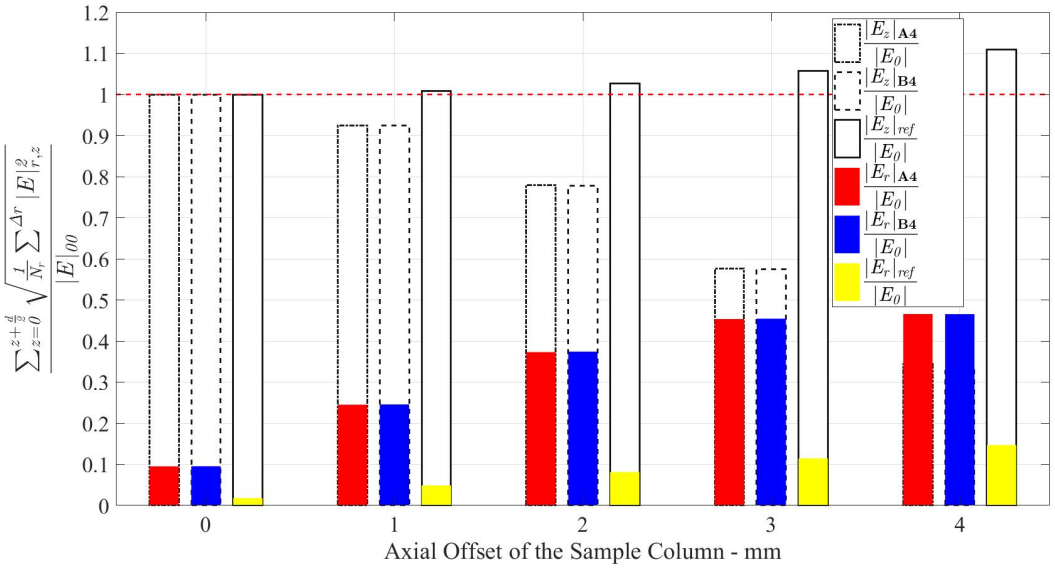


(b) Quart Insert - A4 and B4 Profiles

Figure 3.15: Comparison of Normalized Normal and Tangential Field Variations along the Computation Lines inside the Sensing Column

concentric to the sensing region using the micrometer and moved to emulate the effect of position offset from the center to the perimeter of the sensing region.

### 3.4.2 Measurement Procedure

Measurement results are provided to highlight the influence of two different insert profiles on the frequency detuning with the help of a Fluorinated-Ethylene-Propylene, or in short FEP, sample. The material is similar in characteristics to PTFE-Teflon with a real permittivity of 2, above 1 MHz. The results verify the simulation results regarding a measurable improvement in the overall electric field homogeneity inside the sensing column region.
The cavity resonator fitted with the Quartz dielectric inserts, one by one is attached to the

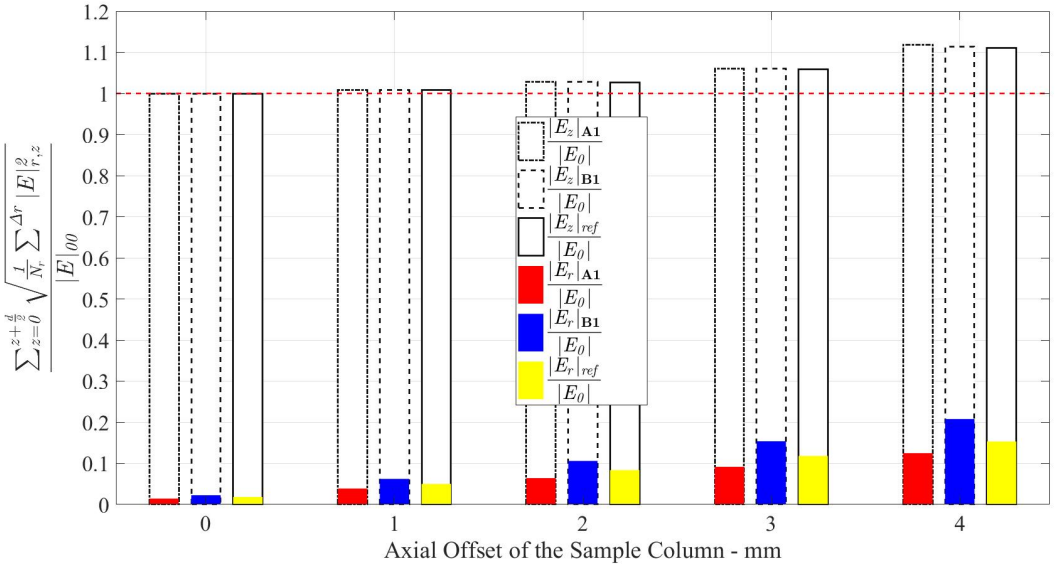


(a) Alumina - A1 and B1 Profiles

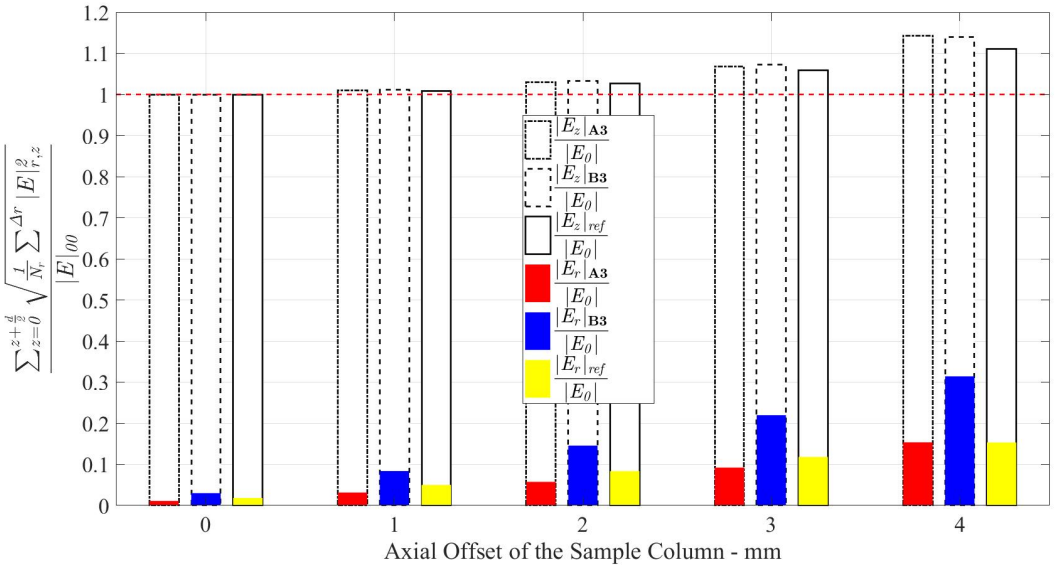


(b) Alumina Insert - A3 and B3 Profiles

Figure 3.16: Comparison of Normalized Normal and Tangential Field Variations along the Computation Lines inside the Sensing Column

mount of the fixture assembly and the measurements are performed for various sample positions inside the sensing column. The central position at zero radius serves as the reference position and then the sample is moved off center with a step size of 0.5 mm. For each sample position from the transmission curve, i.e. the $S_{21}$ magnitude in decibels (dB) is measured and recorded. The measurement is performed in the lab with a controlled 20 degree room temperature. The measurement is performed repeatedly and then an aggregate of the detuned frequency values is post processed for compiling the eccentricity chart. The eccentricity refers to the measure of the sample movement away from the sample. The eccentricity variable is defined as a pointer to the sample position inside the sensing channel, with the center position of the cylindrically shaped channel marked at 0 mm. As the sample is moved toward the edges in the cross-sectional plane of the sensing channel, the eccentricity gradually increases to 3.5 mm. A number of readings

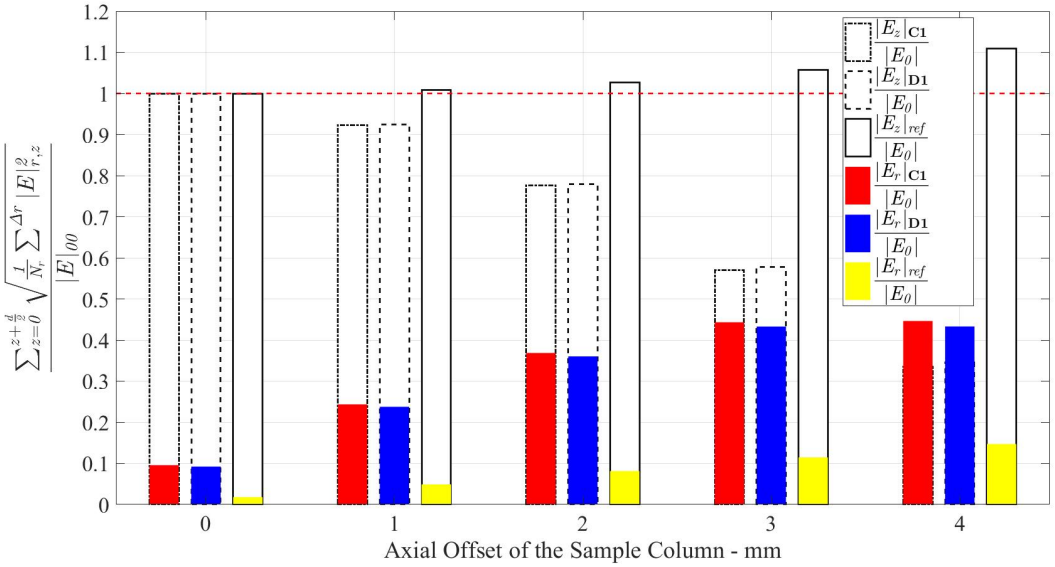


(a) Quartz Insert C1 and D1

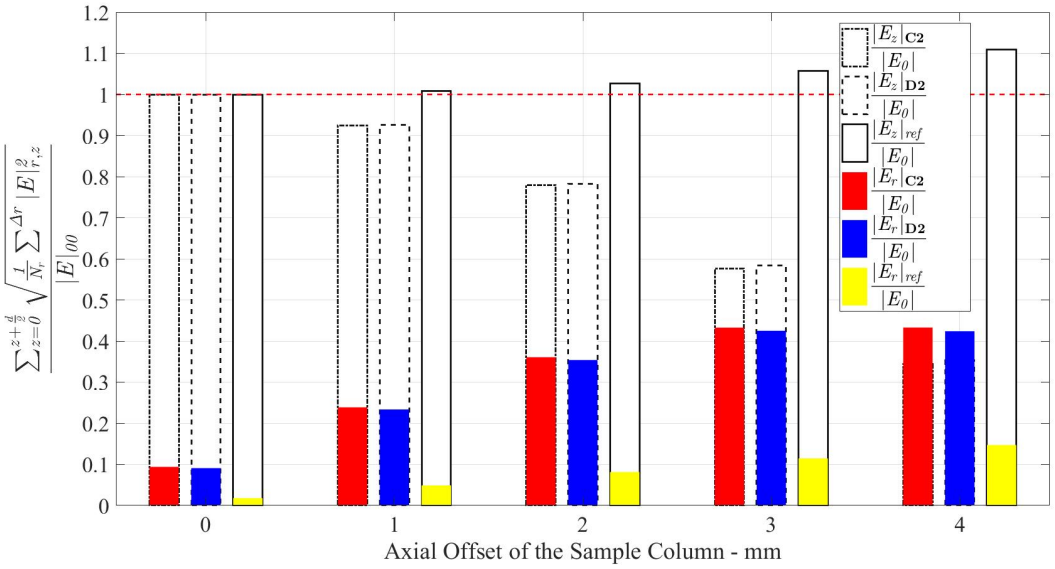


(b) Quartz Insert C2 and D2

Figure 3.17: Comparison of Normalized Normal and Tangential Field Variations along the Computation Lines inside the Sensing Column

are taken for the sample movement from the axial center of the sensing channel, i.e., offset 0 mm, toward the edge of the channel, i.e., offset 3.5 mm position, with step sizes of 0.5 mm The movement of the sample for the cylindrical insert caused a shift of 350 kHz from the center toward the edge point of off-center 3.0 mm. In comparison, the amount of total shift in resonance frequency for the conical insert resulted in 180 kHz. The results normalized to the resonance frequency value are shown in Fig.3.21.

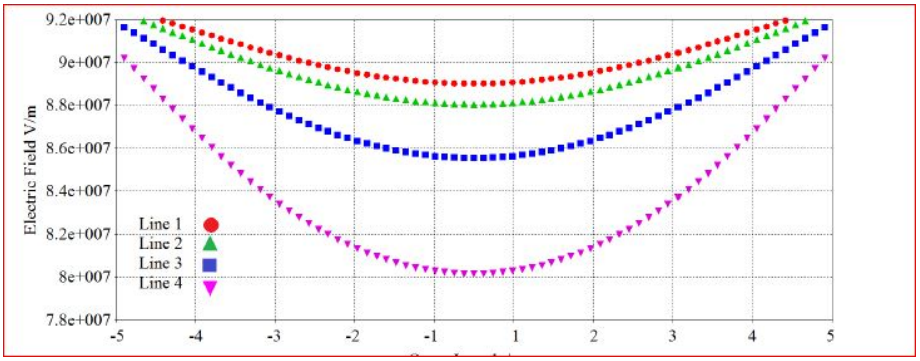


(a) Cylindrical Insert- Quartz

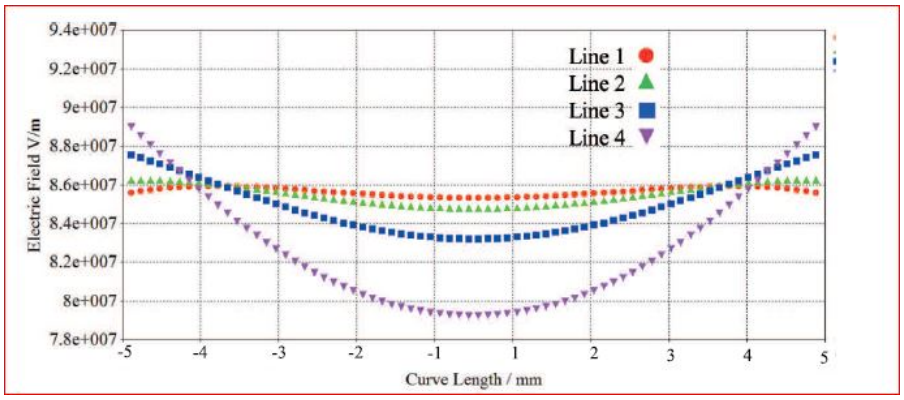


(b) Conical Insert- Quartz

Figure 3.18: Numerically Computed Electric Field Across the Sensing Column Along the Vertically Stacked Evaluation Lines

(a) Cavity along Inserts

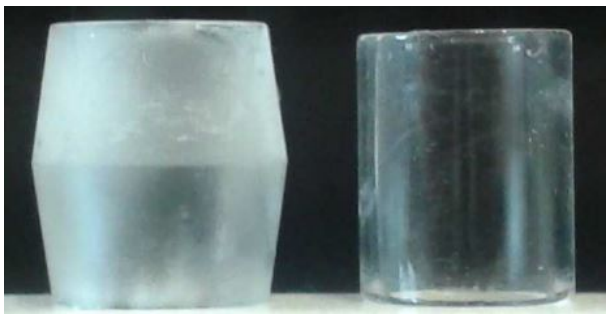

(b) Selected Insert Shapes

Figure 3.19: Prototype with Inserts

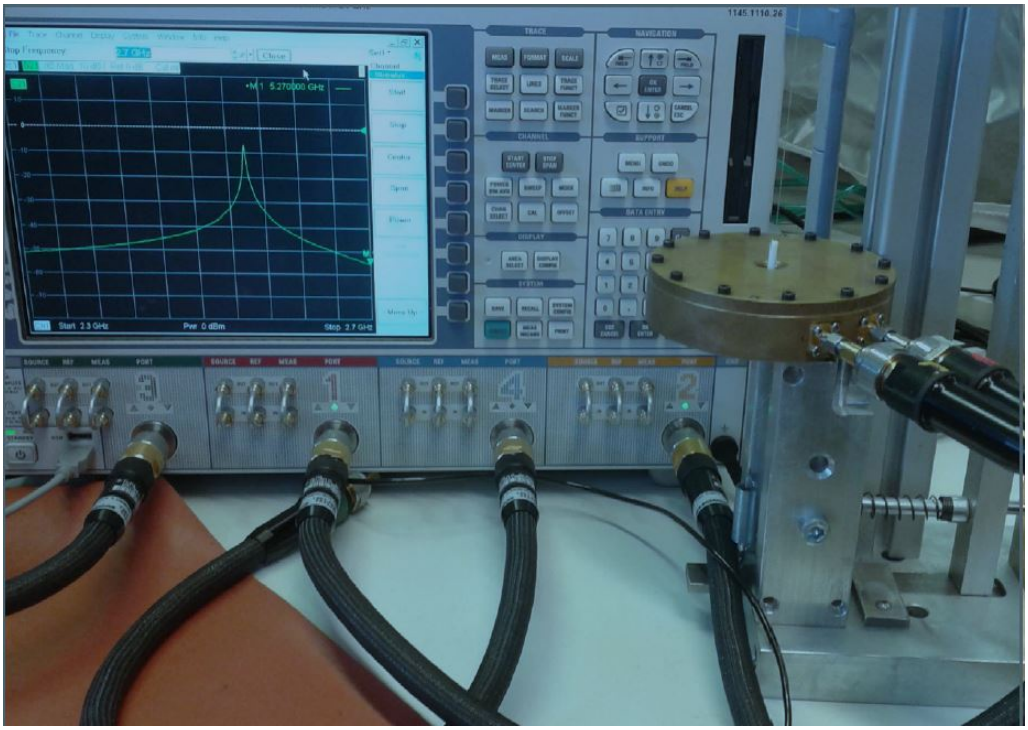

(a) Measurement Setup with Vector Network Analyzer

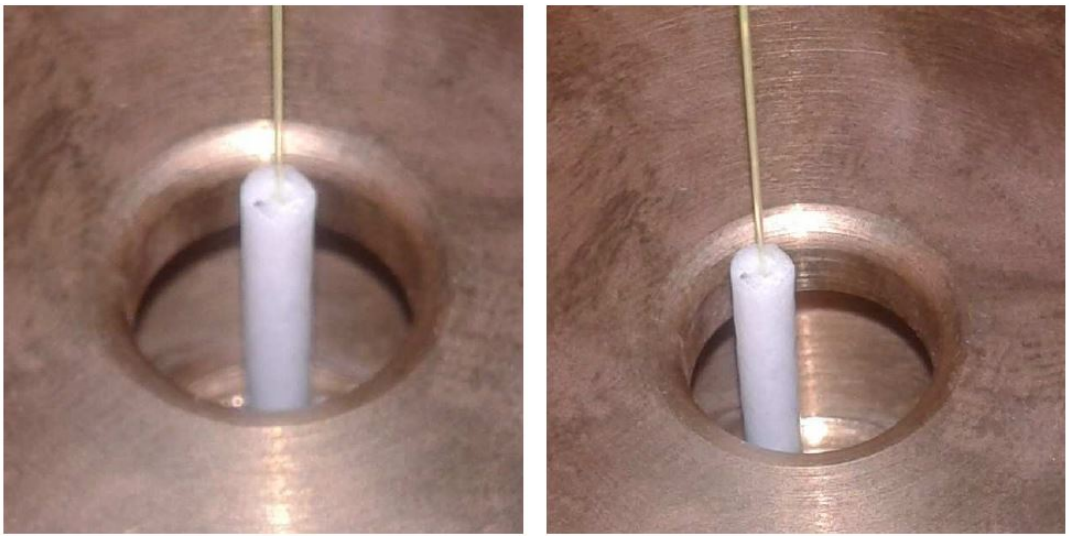

(b) Illustration of Sample Offset

Figure 3.20: Effect of Sample Offset in a Closed Cavity

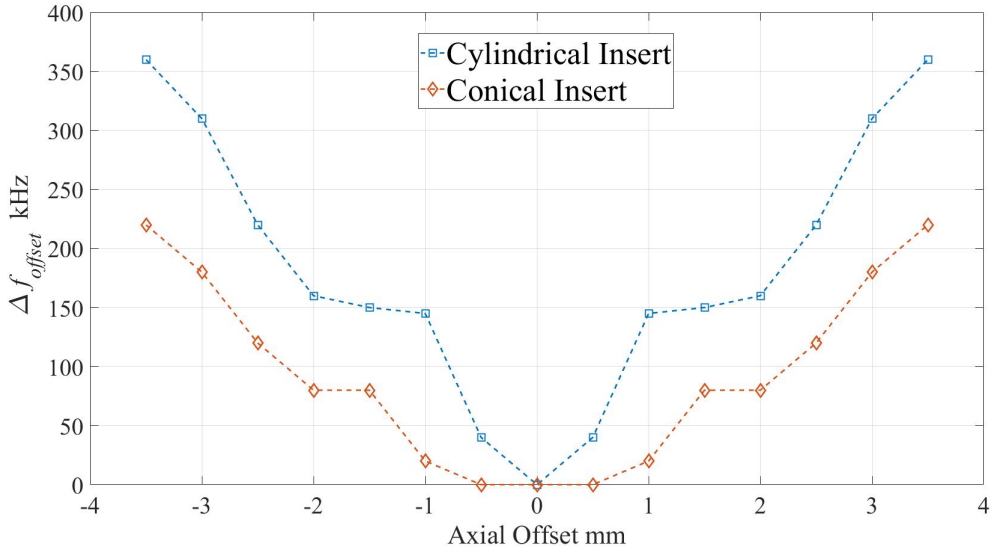


(a) Eccentricity kHz

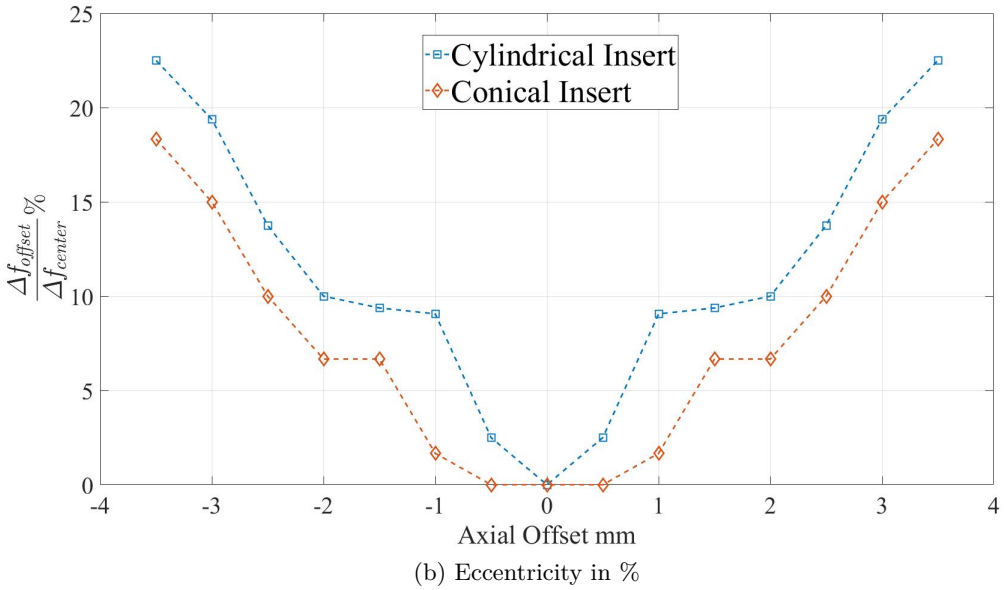


(b) Eccentricity in %

Figure 3.21: Meausured Frequency Detuning For Sample Offsets

# 4 Solution II: Coupled Cavity Configuration

The principle and operation of the pill-box $TM_{010}$ coupled cavity employed for simultaneous sensing of mass and concentric positioning of samples is elaborated in this chapter. The scheme presents an alternative solution to the problem of electric field inhomogeneity in $TM_{010}$ cavities with larger openings for sample insertion. The solution is derived from the implementation techniques of inter-stage couplings in the synthesis and design procedures of narrow bandpass filters. Moreover, the solution is conceptually based on the principle of differential transmission lines which propagate the energy in even and odd transmitting modes. As demonstrated in the previous chapter, the shaped bi-conical dielectric insert can reduce the effect of the electric field inhomogeneity to a measurable extent inside the sensing column. The shaped dielectric profile improves the overall bending of the longitudinal component of the electric field in the sensing column [Faz et al., 2015b]. However, the unaccounted contribution from the radial component of the electric field in the insertion holes remains a major factor contributing to the unnecessary frequency detuning caused by the sample offset movements. The attempt to improve the homogeneity by changing the thickness of insert tube along the cavity length adjacent to the opening does not influence the evanescent radial electric field inside the insertion hole openings. Consequently, the problem demands to be reviewed and analysed from a different perspective. Instead of minimizing the phenomenon causing the unnecessary detuning the solution incorporates the radial component effects of a relatively larger opening into the measurement scheme of the pill-box $TM_{010}$ cavity design. The outcome of approximation methods like variational and perturbations techniques characterize the cavity resonator in terms of changes in the resonance frequency and variations in the quality factor. However, the resonance description is insufficient for the present problem as the knowledge of the electric field distribution inside the non-ideal $TM_{010}$ cavity is highly significant due to its application as a mass and position sensor. Nevertheless, the field distribution for large openings and varying sizes of the coupling apertures can be numerically estimated using full wave simulations available in CST Microwave Studio [Computer Simulation Technology, 2017].

The presented solution includes design and development of a two-port cylindrical cavity using full wave electromagnetic simulations. The $TM_{010}$ cavity is bisected into a pair of segments along its length by a metal plate in the perpendicular plane. Both of the cavity segments are mutually coupled via a formation of circular apertures in the separating metal wall of finite thickness. The cavity is employed for simultaneous detection of changes in the mass density with the additional property of sensing the offset in the concentric flow of the cylindrical dielectric samples [Faz et al., 2015a; Faz and Eibert, 2019]. The sensing region includes the cylindrical column marked by the openings of the insertion holes on top and bottom lids, wholly or partly overlapping the volume occupancy of the central circular aperture in the bisecting metal sheet. The central circular aperture serves as the passage for the flow of the samples besides providing coupling between both cavity sections. Unlike the conventional $TM_{010}$ mode structure, the bisected cavity operates on two coupled resonance modes termed as the anti-symmetric and the symmetric modes with respect to the coupling or symmetry plane. Both modes are separated in frequency determined by the value and the type of the coupling. In principle, a small aperture in a separation wall of finite thickness between the cavities causes anti-symmetrical and symmetrical field distributions of the longitudinal electric field $E_z$ and the circumferential magnetic fields $H_\phi$ (see Eq.(2.13)) above and below the separation [McDonald, 1972; Eastham and Chang, 1991]. Numerically, the inter-cavity coupling is a function of the relative aperture to cavity dimensions and its position in the bisecting metal sheet [Wheeler, 1964]. In the proposed design,

one of the coupled modes identical to the fundamental $TM_{010}$ mode detects the variations in the mass density of the specimen, similar to the permittivity based measurement methods in practice. Additionally, the other coupled resonance mode detects the offset movement from the axial center of the cylindrical cavity. The difference in functionality between the closely occurring resonance modes is due to the distribution of the electric field of anti-symmetrical and the symmetrical nature in the vicinity of the electric polarization aperture. Regarding the limitations of the design, the presented measurement approach employing mutually coupled $TM_{010}$ cavity resonators is generally applicable to relatively large sensing columns with a reduced height or length of a $TM_{010}$ cavity referred to as the pill-box structure. The term relatively large implies that the diameter of the sensing is around one-tenth of the overall cavity diameter. Moreover, the significance of the limit on the cavity height/length is due to the coupling coefficient being a function of the total height of the cavity besides the aperture dimensions in the principal axis, as elaborated in the work of Wheeler [Wheeler, 1964], where coupling coefficients are treated by employing the effective volume models. The first section provides details on the principle of the coupling in view of bandpass filters and transmission lines. It is followed by the general description of coupling apertures and their implementation in the $TM_{010}$ coupled cavity design. The third section provides a number of computational results performed using CST Microwave Studio [Computer Simulation Technology, 2017] to evaluate the performance of the optimal coupled cavity design fitting the sensor specifications and requirements. The verification of the principle of the coupled cavity is demonstrated through measurement results of the constructed sensor prototype.

## 4.1 The Concept of Mutual Coupling

A study of the coupling phenomenon is detailed to serve the basis for the development of the proposed coupled cavity design. The concept of coupling is highly significant in multi-stage filters which are based on coupled resonators, where each resonating stage is mutually coupled to the next stage by employing a lumped or an equivalent distributed element [Dishal, 1949]. In addition, the concept of mutual coupling is the working principle for some distinct types of transmission lines referred to as parallel coupled lines [Getsinger, 1962]. Such physical carriers of signals usually comprise two or more parallel placed conductors inside a shielding, that are characterized by the presence of mutual electromagnetic coupling between the conductors. A unit-less term called the coefficient of coupling is used to quantitatively indicate the value of coupling between any two transmission line segments or adjacent stages of the filters. There are numerous ways to define the coefficient of coupling as its definition varies with the employed model to represent the coupling [Dishal, 1949; Tyurnev, 2010]. In network synthesis theory, the phenomenon of coupling can be demonstrated by bisecting the lumped element based impedance or admittance representation of the T or the Pi two-port network. The T and the Pi network configurations are derived from the impedance and the admittance matrix representations of [Dicke and Purcell, 1948]

$$Z = \begin{bmatrix} Z_{11} & Z_{12} \\ Z_{21} & Z_{22} \end{bmatrix} \qquad \text{and} \qquad Y = \begin{bmatrix} Y_{11} & Y_{12} \\ Y_{21} & Y_{22} \end{bmatrix}, \tag{4.1}$$

respectively. Figure 4.1 depicts the two-port equivalent representations of the matrices shown in Eq.(4.1), where a reciprocal, i.e. $Z_{12} = Z_{21}$ and $Y_{12} = Y_{21}$, two-port network is assumed. In order to demonstrate mutual coupling between the two terminals, the bisection theorem can be applied to the T and Pi networks. First, both networks are sectioned into two equal halves by introducing a symmetry plane at the junction of the shunt arm or at the mid-point of the series arm in their respective impedance or admittance representations, as illustrated with the help of the dashed line in Fig.4.2. According to the bisection theorem, applying equal magnitude

and similar polarity voltages to terminals marked 1 and 2 of the networks in Fig.4.2 causes equal flow of the currents into the two pairs of terminals but zero current flow across the plane of symmetry. As a consequence, it can be stated that the symmetry plane acts as an open circuit or alternately referred to as the perfect magnetic boundary plane. Similarly, if equal voltages but with opposite polarity are applied to terminals 1 and 2, the symmetry plane has zero voltage drop across it, implying a short-circuited symmetry plane which is also termed as the perfect electric boundary plane. If both networks are considered symmetric, i.e. $Z_{11} = Z_{22}$ and $Y_{11} = Y_{22}$, then there are two kinds of input impedances seen from either terminal of the bisected networks called the half network impedances or admittances due to the apparent bisected networks. Open circuit impedance and admittance of the half network seen either from terminal 1 or 2 are given by [Dicke and Purcell, 1948]

$$Z_{open_{1/2}} = Z_{11} + Z_{12}, \tag{4.2a}$$
$$Y_{open_{1/2}} = Y_{11} + Y_{12}, \tag{4.2b}$$

respectively. In the other case, the short-circuit impedance and admittance of the half network either from terminal 1 or 2 are given by [Dicke and Purcell, 1948]

$$Z_{short_{1/2}} = Z_{11} - Z_{12}, \tag{4.3a}$$
$$Y_{short_{1/2}} = Y_{11} - Y_{12}, \tag{4.3b}$$

respectively. The coupling coefficient between adjacent sections, denoted by $k_{i,i+1}$, can be derived from the half network impedances or admittances of the bisected two-port network.

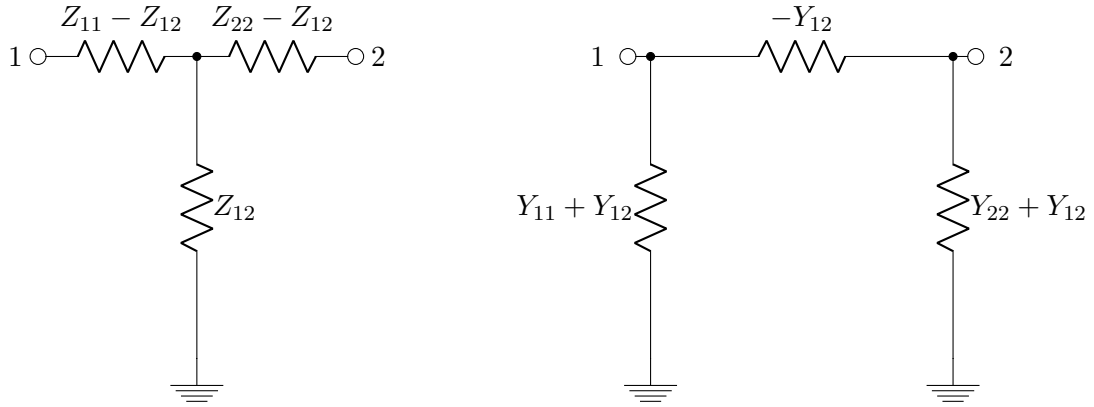


Figure 4.1: Two-Port T (left) and Pi (right) Networks

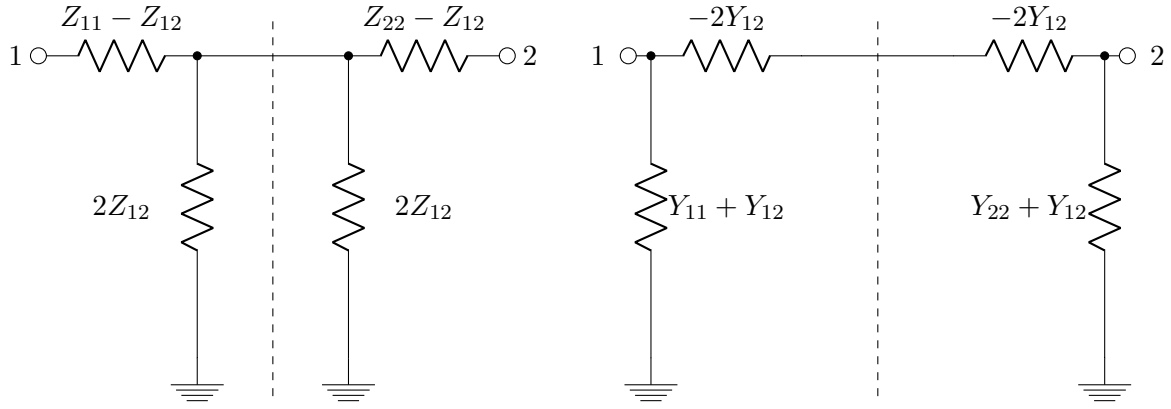


Figure 4.2: Illustration of Bisection Theorem Applied to T (left) and Pi (right) Networks

For instance, the value for the coupling coefficient $k_{21}$ referring to the bisected two-port is proportional to the ratio of the shunt arm impedance (series arm admittance) to the series arm impedance (shunt arm admittance) of a symmetric T network (Pi network) representation [Dicke and Purcell, 1948], i.e.

$$k_{21} = \frac{Z_{short_{1/2}} - Z_{open_{1/2}}}{Z_{short_{1/2}} + Z_{open_{1/2}}} = \frac{Z_{12}}{Z_{11}}, \tag{4.4}$$

alternatively,

$$k_{21} = \frac{Y_{short_{1/2}} - Y_{open_{1/2}}}{Y_{short_{1/2}} + Y_{open_{1/2}}} = \frac{Y_{12}}{Y_{11}}. \tag{4.5}$$

Hence, the coupling coefficient for a two-port bisected network between the two terminals or interfaces is directly related to the measure of the open and short circuit input impedances/admittances derived after bisecting the network.

### 4.1.1 Filters and Coupled Resonators

The synthesis and design of coupled bandpass filters involves the transformation and frequency translation of the low pass prototype to the upper $\omega_2$ and the lower $\omega_1$ pass-band frequencies [Dishal, 1951]. In cascaded designs of synchronously tuned filters, each resonator stage of the bandpass is mutually coupled to the adjacent stage while the individual resonators of each stage are tuned to the center of the pass-band frequency, i.e. $\omega_0 = 2\pi f_0$. It can be deduced from bandpass filter design equations used in the insertion loss method that the fractional bandwidth of the pass-band, denoted by $w = (\omega_2 - \omega_1)/\omega_0$, is directly proportional to the value of inter-resonator couplings derived from the coefficients of the low pass prototype [Jones et al., 1980]. The overall filter configuration comprises either alternate series and parallel lumped element LC resonators connected in a ladder scheme or distributed elements in the form of half or quarter-wavelength long transmission lines with shorted or open-ended output terminals. The simplest definition of coupling for a series-parallel LC cascaded network of resonators in a bandpass design relates the parasitics of either the capacitance or the inductance in one series leg to the similar element in the adjacent parallel leg, formulated in terms of electric $k_E$ and magnetic $k_M$ couplings [Tyurnev, 2010]

$$k_{E(i,i+1)} = \sqrt{\frac{C_s}{C_p}} \qquad \text{or} \qquad k_{M(i,i+1)} = \sqrt{\frac{L_s}{L_p}}, \tag{4.6}$$

where $C_s$ denotes the capacitance and and $L_s$ the inductance of the series LC resonator, with $C_p$ and $L_p$ as the capacitance and the inductance of the adjacent parallel LC resonator, respectively. Due to large variations in the LC ladder network of series and parallel resonators, practical filter design involves employing either only series or parallel connected resonators that are coupled together. In practice, bandpass filter synthesis and design involves implementation of identical resonators whether series or parallel using impedance or admittance inverters. A multi-resonance response is the property of impedance or admittance inversion between similar types of resonators, which can either be synchronously tuned or adjusted by staggered tuning [Zverev, 2005; Dishal, 1951]. Synchronous tuning refers to all resonant elements tuned to a single resonance frequency, whereas staggered tuning refers to symmetrically detuned resonant elements around the center frequency [Dishal, 1951]. Ideally, an inverter operates like a quarter wavelength line of characteristic impedance $K$ or admittance $J$ at all frequencies. Both inverter types are dual to each other, i.e. $J = 1/K$, which are completely identical for the case of unit impedance and admittance inversion, i.e. $K = 1/J = 1$. By definition, the impedance or admittance seen at one end while the other end is terminated by $Z_L$ or by $Y_L$ can be expressed as [Jones et al., 1980]

$$Z_K = \frac{K^2}{Z_L} \qquad \text{and} \qquad Y_J = \frac{J^2}{Y_L}, \tag{4.7}$$

respectively. The quarter wave functionality indicates that a shorted load translates to an open and vice versa, when viewed from the opposite ends. Moreover, by employing the inversion concept series capacitors can be mapped onto shunt inductors, whereas series inductors can be translated to shunt capacitors. In addition to the idealized quarter wave inverter, there are frequency selective narrow-band circuit representations of the inverters, as depicted in Fig.4.3. Negative inductor or capacitor values indicate that these elements are absorbed into the adjacent resonators. As depicted in the Fig.4.4, a pair of series resonators denoted by $i$ and $j$ in a cascade of series resonators for filter operation can be coupled using $K_{ij}$-inverters, whereas the $J_{ij}$-inverter can be used to cascade parallel resonators. A series resonator connected to the one terminal pair of an impedance inverter operates like a parallel/shunt resonator when viewed from the other terminal of the inverter. Similarly, an admittance inverter makes the shunt resonator connected to its one end appear like a series resonator at its opposite end.

### 4.1.2 Coupled Transmission Lines

There are numerous practical examples of coupled transmission lines that include parallel coplanar lines over a grounded substrate, broad-side coupled strip lines between ground planes and balanced twin conductor pairs inside a circular conducting tube also termed as the shielded twisted cable. The coupling properties of transmission lines are generally implemented and realized in a number of applications that include directional couplers, filters and baluns etc. The phenomenon of electromagnetic coupling between transmission lines occurs, for instance, when two unshielded TEM transmission lines of the same characteristic impedance $Z_0$ are placed in close proximity to each other. Such an arrangement will cause the respective transverse electric and magnetic fields on each line conductor to interact with the other line. Figure 4.5 shows the example of a parallel coupled transmission line comprising two rounded conductors with uniform cross-sections in a homogeneous and isotropic medium of permittivity $\epsilon$ and relative permittivity $\epsilon_r$ placed over a common ground. Due to the symmetric geometry, the impedance of the coupled line can be specified by two characteristic modes called the even mode $Z_{0e}$ and the odd $Z_{0o}$ mode impedance [Getsinger, 1962]. The definition of the overall characteristic impedance in the coupled transmission lines can then be stated as the geometric mean of even and odd impedances [Getsinger, 1962],

$$Z_0 = \sqrt{Z_{0e} Z_{0o}}. \tag{4.8}$$

In terms of excitation of the signals, the even and the odd mode on the transmission line are also

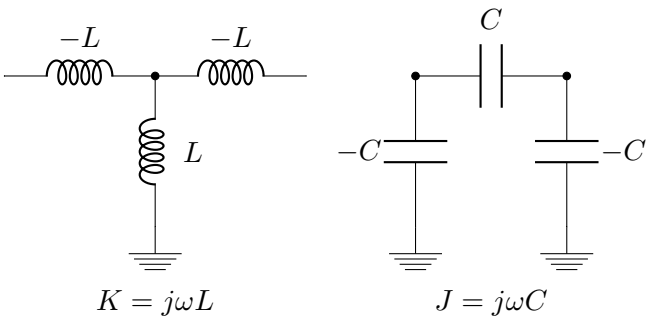


(a) Impedance Inverter (b) Admittance Inverter

Figure 4.3: Circuit Forms of Inverters

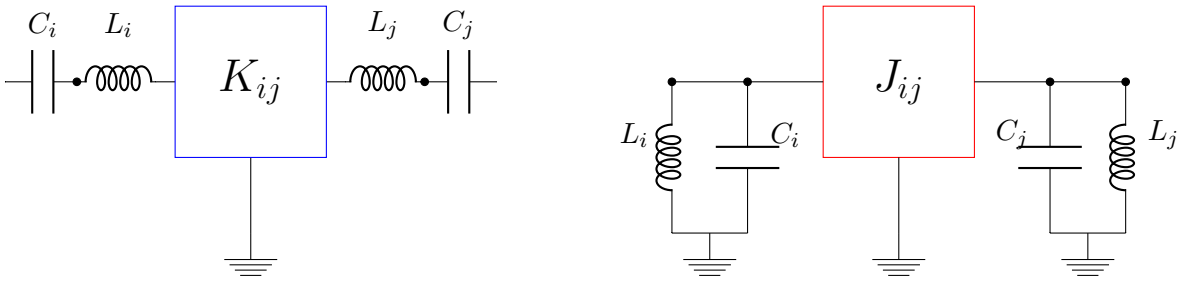


(a) Series Resonators with $K$-Inverter (b) Parallel Resonator with $J$-Inverter

Figure 4.4: Cascaded Bandpass Filter with Inverter

known as the common mode and the differential mode, respectively. The even or the common mode transmission refers to the same direction of current flow over both the conductors having equal polarity with respect to the common ground. The differential mode has opposite direction of current flowing over the conductor. Variational techniques and conformal mapping schemes are used to solve for the even and the odd mode characteristic impedances, that can be given for a parallel coupled line as [Jones et al., 1980]

$$Z_{0e}\sqrt{\epsilon_r} = \frac{120\pi}{C_{0e}/\epsilon}, \tag{4.9a}$$

$$Z_{0o}\sqrt{\epsilon_r} = \frac{120\pi}{C_{0o}/\epsilon}, \tag{4.9b}$$

respectively, where $C_{0e}$ is the static capacitance per unit length of one conductor to the ground in even mode operation, whereas $C_{0o}$ is the static odd mode capacitance, as indicated in Fig.4.5. The physical spacing between the two conductors and their respective distance to the common ground plane determine the amount of each associated capacitance. The plane of symmetry acts as a magnetic wall in the even mode and hence it is equivalent to the half-network open circuit impedance in Eq.(4.2). Similarly, the electrical wall in the odd mode is equivalent to the half network short circuit impedance stated in Eq.(4.3). Consequently, using Eqs.(4.4) and (4.8) the coupling coefficient in terms of characteristic impedances is given by

$$k_{21} = \frac{Z_{0e} - Z_{0o}}{Z_{0e} + Z_{0o}} \tag{4.10}$$

with the even and odd mode impedances stated as

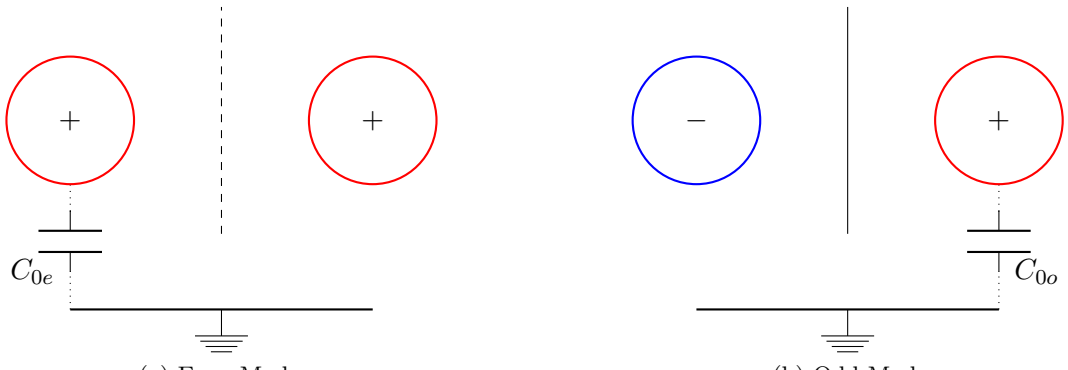


(a) Even Mode (b) Odd Mode

Figure 4.5: Even (left) and Odd (right) Mode Configurations

$$Z_{0e} = Z_0\sqrt{\frac{1+k}{1-k}}, \tag{4.11}$$

$$Z_{0o} = Z_0\sqrt{\frac{1-k}{1+k}}, \tag{4.12}$$

respectively. In terms of field distribution Fig 4.6 shows another example of the electric field for both types of modes in case of a coplanar transmission line. It can be observed that the static capacitances of $C_{0e}$ and $C_{0o}$ in this particular case are actually a sum of parallel plate capacitances and additional fringing capacitances [Jones et al., 1980]. The fringing capacitance effects account for the distortion of the electric field lines due to edges and finite thickness effects of the conductors. The fringing capacitances can be a useful property in electric coupling elements where its presence or absence dependent on the even or the odd mode can be extracted as a distinguishable factor to aid measurements. For example, a reduced distance between the two parallel bars increases the odd mode capacitance as well as the fringing capacitance between the conductors, which causes the odd mode impedance to decrease resulting in a tightly coupled system.

## 4.2 Coupled Cavity Sensor

The configuration of mutually coupled cavities is a widespread technique in filter and a variety of coupler designs. However, the principle of mutually coupled resonating structures for material sensing applications, such as the coupled pill-box $TM_{010}$ cavity, is a rarely employed technique in the published literature. Employing two mutually coupled cavities via apertures results in resonance mode splitting of symmetric and anti-symmetric nature similar to the characteristic impedance division into the even and the odd modes in parallel coupled transmission lines as discussed in the preceding section. If the cavity resonator is modeled by a LC tank circuit whose resonance is defined by $f_0 = \frac{1}{2\pi\sqrt{LC}}$, then the similarity between even and odd mode impedances and splitting of resonance modes can be easily drawn. For instance, from Eq.(4.9) it can be deduced that there exist a pair of frequencies corresponding to the odd mode capacitance $C_{0o}$ and the even mode capacitance $C_{0e}$, that can be given in terms of mode splitting as $f_{0o} = \frac{1}{2\pi\sqrt{LC_{0o}}}$ and $f_{0e} = \frac{1}{2\pi\sqrt{LC_{0e}}}$, respectively. A similar analogy can be drawn for the inductance values.
In order to implement the coupling, specifically between $TM_{010}$ cavities, a thin partitioning metal sheet with diaphragms or aperture openings in the sheet is presented as the coupling method. The implementation of the coupling elements realized as apertures in the bisected $TM_{010}$ cavity causes mode splitting yielding a pair of resonance modes with unique and distinguished field distribution that provide the possibility for additional sensing parameters. The response curve of a coupled cavity can be categorized according to over-coupled, under-coupled

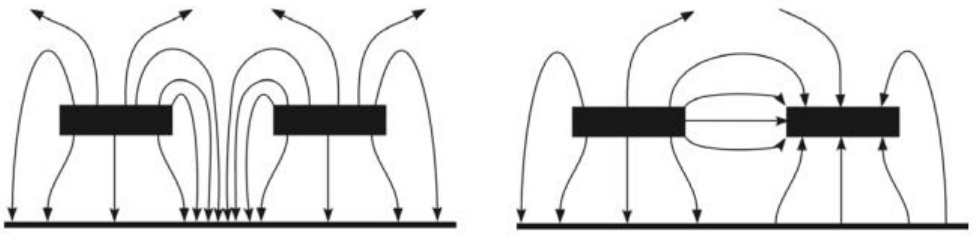

(a) Even Mode (b) Odd Mode

Figure 4.6: Electric Field Coplanar Line [Microwaves101, 2018]

or critically coupled. In filter theory such responses are rather dealt with in terms of Chebyshev and Butterworth response types [Dishal, 1951]. If the cavity sections are strongly coupled, i.e. over-coupled, two clear resonance peaks are observed, as illustrated in Fig.4.7, which occur when the coupling is greater than the critical value of the reciprocal of the Q-factor, i.e. $1/Q$ [Jia-Sheng Hong and Lancaster, 1996]. The technique of employing a coupled cavity sensor instead of multi-mode cavity measurement schemes, for example as detailed in [Lakshminarayana et al., 1979], is presented as an optimized and a practically viable option in terms of the selection and control of the resonance frequencies. The foremost advantage of using a coupled cavity sensor in comparison to the bi-modal sensors is that the separation frequencies or the split bandwidth BW $= f_2 - f_1$ are a direct function of the value of the coupling coefficients, as discussed in Sec.4.1.1, instead of the eigenfunctions of the cavity dimensions as in multi-mode cavities. It implies that based on the strength of the electric $k_E$ and the magnetic $k_M$ couplings the pair of coupled resonance frequencies can be accordingly adjusted on the frequency scale.

### 4.2.1 Aperture Coupling Definitions

In general, an aperture or an iris created by an opening in a metal partition perpendicular to the axis of a waveguide or a transmission line is usually treated as a discontinuity with an equivalent circuit representation, as discussed in Sec.4.1. Alternatively, an aperture in the partitioning metal plane can also be considered as a junction of two emergent and coupled waveguide or transmission lines of equal or unequal characteristic impedances at each end. Upon excitation from dominant mode energy at one end, the vicinity of the aperture is characterized by the presence of higher order electromagnetic fields of evanescent nature which represent the stored or reactive energy of electric or magnetic nature. A portion of the dominant mode incident energy is reflected back to one end while the other portion gets transmitted to the other coupled end usually connected to a reflection less load. Therefore, aperture loaded junctions in waveguides or cavities when viewed from one input end as the reference can be identified as complex impedance and admittance quantities. The input impedance $Z_{in}$ or input admittance $Y_{in}$ are based on the difference between the stored electric energy $W_E$ and magnetic energy $W_H$

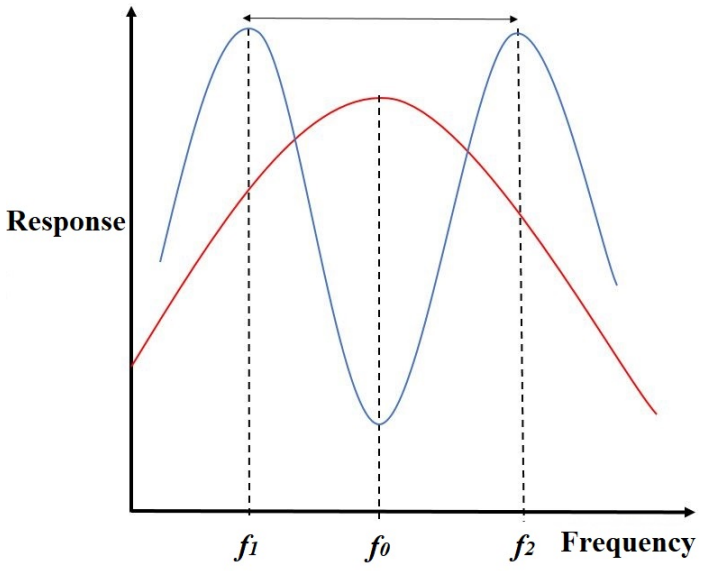


Figure 4.7: Coupling Response: Critically Coupled (red), Over-coupled (blue)

as well as the dissipated power $P_d$ inside the aperture stated as [Collin, 2001]

$$Z_{in} = R + jX = \frac{2j\omega(W_H - W_E) + P_d}{\frac{1}{2}II^*}, \tag{4.13a}$$

$$Y_{in} = G + jB = \frac{2j\omega(W_E - W_H) + P_d}{\frac{1}{2}VV^*}, \tag{4.13b}$$

where $I$ and $V$ represent the equivalent excitation or source currents and voltages, respectively. In the ideal lossless case the power dissipation is taken zero, i.e $P_d = 0$, which leaves a purely reactive or susceptive aperture representation with the magnitude of the reactance or susceptance proportional to the difference of the stored energy. The classification of the apertures is based on the contribution of the sign of the impedance or the admittance. For instance, $W_E > W_H$ implies that the aperture has positive susceptance which can be modeled by a shunt or a series capacitance depending on the excitation modes of transverse electric or transverse magnetic nature [Collin, 2001].
Regarding waveguides and cavities the full wave electromagnetic problem represented by Eq.(4.13) should be solved for the geometric configuration of the aperture to evaluate its reactance or susceptance values. Apertures based on its placement position inside a waveguide or a cavity act as either the electric or the magnetic current sources termed as dipoles. Small circular apertures in infinitesimally thin walls can be represented by an infinitesimal electric and magnetic dipole excited by the normal electric field and the tangential magnetic field present at the aperture position in its absence, respectively. Based on the image theory, the dipole excitations result in two oppositely directed electric polarization currents $\boldsymbol{P_e}$ normal to the conducting wall and magnetic polarization currents $\boldsymbol{P_m}$ tangential to the conducting wall [Pozar, 2011], as illustrated in Fig.4.8, which are defined as

$$\boldsymbol{P_e} = \epsilon_0 \alpha_e \boldsymbol{E_n}, \tag{4.14a}$$

$$\boldsymbol{P_m} = \alpha_m \boldsymbol{H_t}, \tag{4.14b}$$

where

- $\alpha_e$ electric polarization given by $\frac{2}{3}r_a^2$ for circular apertures with radius $r_a$.
- $\alpha_m$ is called the magnetic polarization given by $\frac{4}{3}r_a^2$ for circular apertures with radius $r_a$.

Regarding the coupling effects of apertures, Wheeler presented aperture coupling between resonant cavities in terms of effective volumes for various aperture shapes derived from the rule of one half, elaborated in [Wheeler, 1964]. For a dominant $TM_{010}$ mode cavity, Wheeler formulated the approximate method to evaluate the coefficient of coupling contributed by the aperture, whether electric $k_E$ or magnetic $k_M$ in nature. The coupling coefficient between cavities can be defined as approximately one-fourth the ratio of the effective volume of the aperture to the effective volume of the cavity [Wheeler, 1964]. For cylindrical apertures with radius $r_a$ and a finite thickness $t$ in a metal wall partitioning in the perpendicular plane along the length of a $TM_{010}$ mode cavity of radius $R$, the electric and the magnetic coupling coefficients can be stated as [Wheeler, 1964]

$$k_E = \frac{V_{ea}}{4V_{ec}}, \tag{4.15a}$$

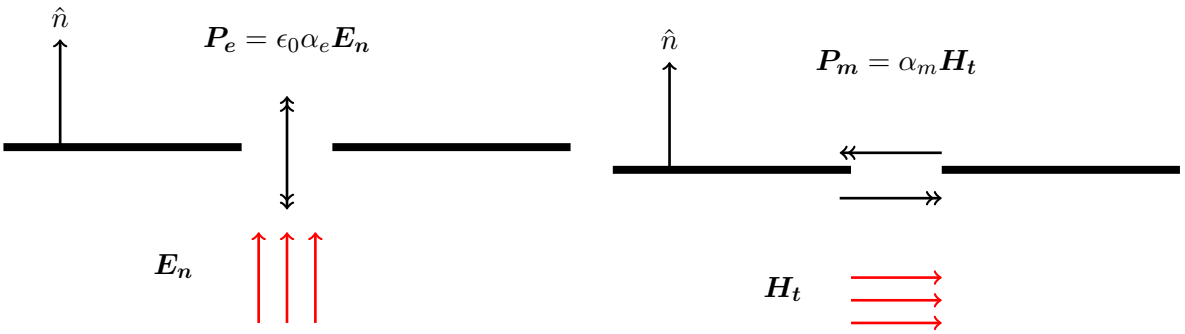


(a) Electric Polarization (b) Magnetic Polarization

Figure 4.8: Electric and Magnetic Apertures

$$k_M = \frac{V_{ma}}{4V_{mc}}, \tag{4.15b}$$

respectively, where

- $V_{ea}$ and $V_{ma}$ are the effective spherical volumes of electric and magnetic circular apertures stated as

$$V_{ea} = \frac{8}{3} r_a^3 e^{-2.405(t/r_a)}, \tag{4.16a}$$

$$V_{ma} = \frac{16}{3} r_a^3 e^{1.84(t/r_a)}, \tag{4.16b}$$

  respectively. The thickness correction terms $e^{-\text{const}(t/r_0)}$ are derived from McDonald's work which indicates the loss of coupling proportional to the exponential decay based on to thickness of the aperture [McDonald, 1972].

- $V_{ec}$ and $V_{mc}$ are the effective volumes of the cavity which are estimated in terms of a uniform distribution of the electric and the magnetic resonance fields. The effective volume of the resonant cavity is defined as the volume which would contain the same amount of the electric or the magnetic energy if filled with uniform intensity equal to the reference values of $E_z$ or $H_\phi$, respectively. For cylindrical cavities with $\text{TM}_{010}$ dominant mode, the value can be evaluated using the average distribution of the electric and the mangetic field functions, i.e. Bessel functions of zeroth and first oder, over the total volume of cylinder, i.e. $\pi R^2 h$ [Wheeler, 1964],

$$V_{mc} \approx 0.50 \pi R^2 h, \tag{4.17a}$$

$$V_{ec} \approx 0.425 \pi R^2 h. \tag{4.17b}$$

Substituting Eq.(4.16) and Eq.(4.17) in Eq.(4.15) provides a reasonably accurate estimate for the values of coupling coefficients based on the approximate geometric analysis. The above formulations for coupling coefficients are highly accurate for one-fourth the aperture radius relative to the cavity radius and fairly accurate for one-half of the aperture radius relative to the cavity radius [Wheeler, 1964].

### 4.2.2 Coupled Resonance Modes in $TM_{010}$ Cavity

As per the image theory, the two oscillation states for a coupled $TM_{010}$ cavity structure are derived from the electric and the magnetic boundary conditions of the bisecting plane along its length [McDonald, 1972]. With respect to the partitioning plane the oscillation states are symmetrically and anti-symmetrically oriented. The difference between the symmetric and the anti-symmetric mode in terms of the field distribution around the vicinity of the aperture is highlighted in this section. The knowledge of the field distribution around the vicinity of the aperture is significant in deducing a fitting representation of the coupling circuit model in the following Sec.4.2.3. Moreover, the difference in the mode distribution and orientation around the coupling space also provide an indication of the functionality of the respective mode in material sensing applications.

Figure 4.9 illustrates the phenomenon of mode splitting into anti-symmetric and symmetric electric field distributions in a two-dimensional analogy of the bisected $TM_{010}$ cavity of width/diameter $2R$ and $\boldsymbol{E_n}$ as the normal field. An anti-symmetric field distribution results when the cavity is partitioned in the plane perpendicular to its vertical length by placing a perfectly conducting strip, as shown in Fig.4.9a. Normal electric fields in each section, denoted by $\boldsymbol{E_n/2}$ and $\boldsymbol{E_2/2}$, tend to orient themselves in the same direction due to the boundary condition of the field at perfect electric boundaries. The presence of the electric field normal to the perfect electric boundary plane induces infinite charge density in the conducting plane, which defines the identical orientation of the electric fields in both section. When the partition is replaced with a perfectly insulating strip or a magnetic boundary plane, the field orientation in one of the cavity reverses in order to satisfy the boundary condition of zero normal electric field on perfectly magnetic boundaries, as illustrated in Fig.4.9b, which defines the existence of the symmetric mode with respect to the bisecting axis.

The definitions of anti-symmetric and symmetric modes can now be applied to the phenomenon of electric aperture coupling. An analogy to the aperture coupling in a perfectly conducting plane between two cavity sections of radius $R$ can be drawn by introducing an infinitesimally thin element of length $d_e$ at the position of maximum electric field given by $E_n \approx \mathrm{J}_0(\frac{2.405r}{R})$ to emulate the opening effect in an otherwise perfectly conducting partition. The thin strip can be replaced by either a perfectly conducting strip to represent the short circuit equivalent plane or a perfectly insulating strip to represent the open circuit equivalent plane, as elaborated in Sec.4.1. The introduction of a perfectly conducting strip has no effect on the anti-symmetric distribution hence the original field in the two-dimensional cavity can be represented by $\boldsymbol{E_e}$ as shown in Fig.4.10a. The magnetic boundary condition for the strip is emulated by replacing the thin conducting strip with an infinitesimally thin perfectly insulating strip. It results in the outward bending or fringing of the original $\boldsymbol{E_n^e}$ occurs due to the magnetic boundary condition at the strip position. The resulting electric field denoted by $\boldsymbol{E_n^m}$ occurs which is the equivalent of the symmetric mode, as depicted in Fig.4.10b, since the directions in each physically isolated

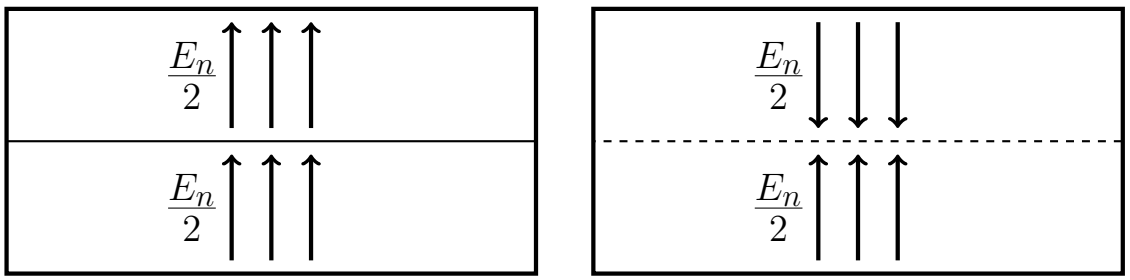


(a) Conducting Plane: Anti-Symmetric Electric Field (b) Insulating Plane: Symmetric Electric Field

Figure 4.9: Mode Splitting Definition: Electric Field

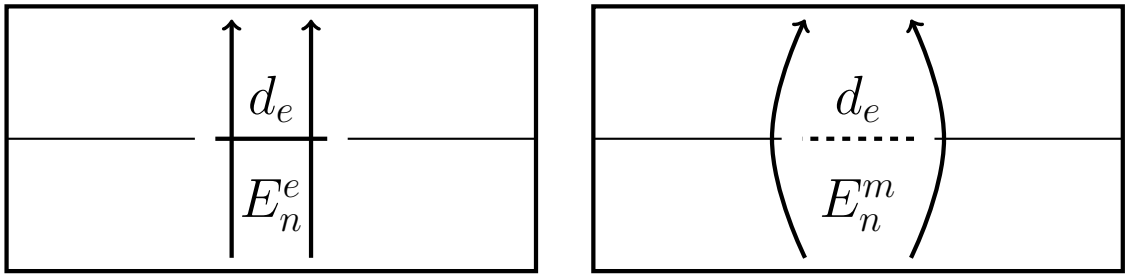


(a) Perfectly Conducting Strip: Aperture Analogy (b) Perfeclty Insulating Strip: Aperture Analogy

Figure 4.10: Analogy to the Electric Field Distribution in the Vicinity of the Coupling Aperture

sections can be reversed [Cohn, 1951]. In terms of energy description, when the former case is compared to the latter case, there is an overall reduction in stored electric energy $W_E$, i.e. $\frac{1}{2}\epsilon|E_n^e|^2 > \frac{1}{2}\epsilon|E_n^m|^2$. It also implies a proportional increase in the resonance frequency due to the reduced susceptance for the symmetric resonance mode [Zverev, 2005]. It is noteworthy to mention that when such fringing fields are present in the sensing column that overlaps an electric aperture, the symmetric electric field around the coupling space exhibits the ability to detect the variation in the axial offset of the sample.

Similarly, Figure 4.11 illustrates the phenomenon of mode splitting for anti-symmetric and symmetric magnetic field distributions, when the two-dimensional cavity of width $2R$ with the magnetic field $H_t$ is partitioned along its vertical length. The tangential magnetic fields in each section denoted by $\boldsymbol{H_t}/2$ and $\boldsymbol{H_t}/2$ remain oriented in the same direction when the split plane is perfectly conducting, as shown in Fig.4.11a. As the parallel directed magnetic fields on the perfect electric boundary induces infinite charge density resulting in identical orientation in both sections with respect to the splitting plane. When the partition is replaced with the magnetic wall, the field orientation in one of the cavity reverses to satisfy the boundary condition of zero tangential magnetic field on the insulating boundaries, as illustrated in Fig.4.11b. The former is an example of anti-symmetric mode distribution in the cavity whereas the latter refers to the symmetric resonance mode. A further analogy to the magnetic aperture coupling between the two cavity sections can be drawn by introducing a thin linear element of length $d_m$ to represent the opening at the maximum magnetic field $H_t \approx \mathrm{J}_1(\frac{2.405r}{R})$ position in the conducting partition. The introduction of such an element has no effect on the anti-symmetric distribution and hence the overall field can be represented by $\boldsymbol{H_t^e}$, as shown in Fig.4.12a. However, when the linear body representing the aperture is replaced with a magnetic element the bending or inward fringing of the field occurs denoted by $\boldsymbol{H_t^m}$, as depicted in Fig.4.12b. It results in an overall increase of the magnetic energy $W_M$, i.e. $\frac{1}{2}\epsilon|H_t^m|^2 > \frac{1}{2}\epsilon|H_t^e|^2$. Hence, a proportional decrease in

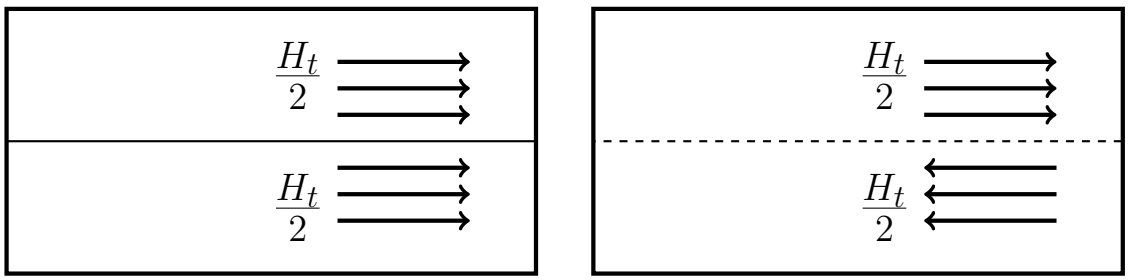


(a) Conducting Plane: Anti-Symmetric Magnetic Field (b) Insulating Plane: Symmetric Magnetic Field

Figure 4.11: Mode Splitting Definition: Magnetic Fields

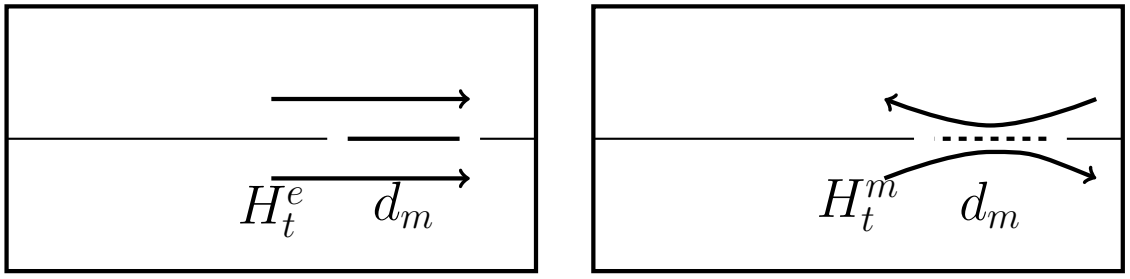


(a) Perfeclty Conducting Strip: Aperture Analogy (b) Perfeclty Insulating Strip: Aperture Analogy

Figure 4.12: Analogy to the Magnetic Field Distribution in the Vicinity of the Coupling Aperture

the resonance frequency of the symmetric resonance mode takes place as a result of the magnetic aperture coupling.
For thick apertures in a finite thickness wall $t$ the symmetric and anti-symmetric modes are characterized by the respective electrostatic or magnetostatic potential functions formulated and evaluated in [Gluckstern and Diamond, 1991; Lee and Eom, 1996, 1998]. The anti-symmetric electrostatic potential $\Phi_a$ inside the aperture has a dependence on $\sinh(2\pi t/\lambda_c)$ function whereas the symmetric electrostatic potential $\Phi_s$ has a $\cosh(2\pi t/\lambda_c)$ dependence, where $z$ is the longitudinal coordinate and $\lambda_c$ is the cut-off wavelength of the circular aperture. In order to satisfy the boundary conditions at the inner metal walls of finite thickness apertures, there is a strong radial or tangential component of the electric field $E_t$ and normal magnetic field $H_n$ inside the aperture, prominent for the symmetric mode.

### 4.2.3 Coupling Circuit Model for $TM_{010}$ Cavity

In a number of microwave applications including cavity resonators, a two-port equivalent circuit defined in terms of impedance or admittance matrix can be a significant tool for coupling analysis. The $TM_{010}$ cavity resonator is both axially and longitudinally symmetric in the $rz$ and $r\phi$ planes of the cylindrical coordinate system. Analogous to the half network division of T and Pi networks in Sec.4.1, the cavity structure when bisected in the perpendicular plane along its length by inserting a metal sheet can be termed reciprocal and symmetric due to its geometry. The representation of the aperture coupling can be modeled by employing respective $J$ or $K$ inverters based on the nature of the coupling elements in the metallic wall and its effect on the original field distribution, as elaborated in Sec.4.2.2. The series element in the $J$ inverter or equally the shunt element in the $K$ inverter usually represent(s) the dominant mode coupled energy through the aperture, primarily depending on the aperture excitation. On the other hand, the shunt elements in $J$ or equally the series elements in $K$ inverter represent(s) the decay effects or attenuation of the coupled energy usually as a function of its dimensions including the thickness of the aperture [Cohn, 1952]. The bisection results in a pair of short and open circuit impedances which correspond to the resonance mode-splitting phenomenon with a pair of distinguishable modes [Jia-Sheng Hong and Lancaster, 1996; Kobayashi and Minegishi, 1988].
A series or parallel $LC$ resonant circuit can be employed as a model for mapping the electromagnetic problem of the cavity resonator onto the equivalent lumped element model which is valid for a narrow band of frequencies centered at the resonance frequency of the cavity. Figure 4.13 depicts the models for a bisected pill-box cavity coupled via electric and magnetic polarization apertures in a metal sheet of finite thickness placed in the transverse plane dividing the cavity into two segments. Since the $TM_{010}$ has the electric field $E_z = \mathrm{J}_0(\frac{2.405r}{R})$ concentrated at the center, it can be represented by the equivalent capacitance $C_c$ of the cavity. Similarly,

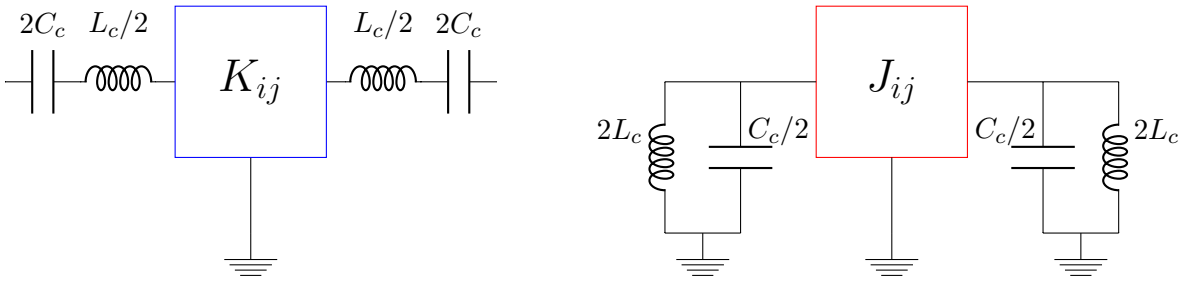


(a) Series $LC$ Resonator with $K$-Inverter: Magnetic Coupling Model

(b) Parallel $LC$ Resonator with $J$-Inverter : Electric Coupling Model

Figure 4.13: Series and Parallel Models for the Bisected and Halved Cavity Resonator

the magnetic field $H_\phi = \mathrm{J}_1(\frac{2.405r}{R})$ around the perimeter can be considered to represent the equivalent inductance $L_c$ of the cavity. The division into two cavity segments results in reduced or increased capacitance and inductance values which in turn are dependent on the type of coupling element. The electric coupling can be modeled via parallel $LC$ topology using $J$-inverters, whereas the magnetic coupling can be modeled by series $LC$ configuration using $K$-inverters. Each bisected cavity can be treated as an individual $LC$ resonator, similar to adjacent sections of a filter. The bisected cavity using the inverter model coupling technique will either enhance or reduce the energy storage capability [McDonald, 1972], causing the frequency split resulting in a pair of resonance modes. The circuit representation of $J$ and $K$ inverters and the effect of electric and magnetic walls of separation are further highlighted in Fig.4.14 and Fig.4.15. Considering $k_E$ and $k_M$ as the respective coupling coefficients and equating $L_c = L$ and $C_c = C$ from Fig.4.13. Further elaboration of the electric and the magnetic coupling models for the bisected cavities using the $J$ and $K$ inverter scheme is as follows:

- Figure 4.14a depicts the model for the $J$-inverter of unity impedance in the form of a Pi-network of capacitors based on the circuit representation of Fig.4.3. The inverter has a

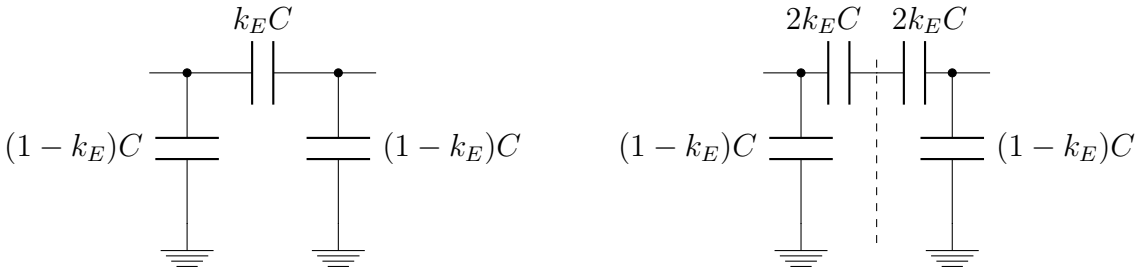


(a) Capacitive Coupling using Inverter

(b) Introduction of Symmetry Plane

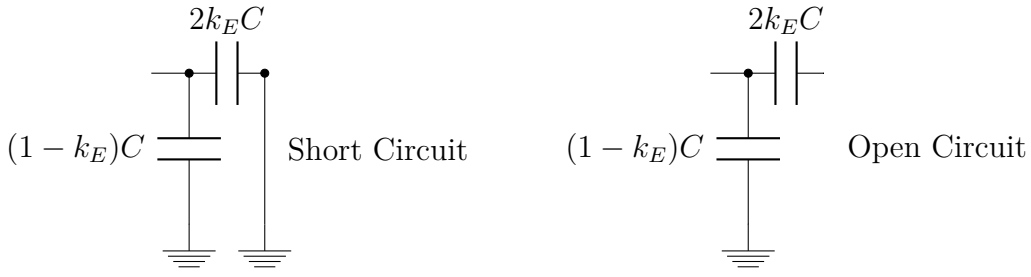


(c) Anti-Symmetric Mode

(d) Symmetric Mode

Figure 4.14: Capacitive Coupling using Inverters

positive series admittance $k_E C$ representing the polarization of the electric aperture and a negative shunt admittance $-k_E C$ representing the sum of evanescent fields inside the aperture that are radial in nature.

- The bisection of the cavity then can be represented by inserting a symmetry plane as shown in Fig.4.14b resulting in mode-splitting and a pair of resonance frequencies. One mode corresponds to replacing the symmetry plane with an short-circuited plane, whereas the other mode corresponds to a open-circuited plane.

- While treating the symmetry plane as an electric wall or a short circuit, as shown in Fig.4.14d, the total capacitances of the cavity increases by $(1+k_E)C$. Hence, the resonance frequency of the split mode (anti-symmetric mode) is given as [Zverev, 2005; Jia-Sheng Hong and Lancaster, 1996],

$$f_{anti-symmetric} = \frac{1}{2\pi\sqrt{L(1+k_E)C}}. \tag{4.18}$$

- While treating the symmetry plane as a magnetic wall or an open circuit, as shown in Fig.4.14c, the total capacitances of the cavity reduces by $(1-k_E)C$ indicating a decrease in the total energy, as discussed in Sec.4.2.2 (see Fig.4.10b). As a result, the resonance frequency of the split mode (symmetric mode) is given as [Zverev, 2005; Jia-Sheng Hong and Lancaster, 1996],

$$f_{symmetric} = \frac{1}{2\pi\sqrt{L(1-k_E)C}}. \tag{4.19}$$

Similarly, for the magnetic coupling model, the mode splitting can be elaborated as:

- Figure 4.15a depicts the unity impedance $K$-inverter in the T-configuration of inductors with values of negative series impedance $k_M L$ and positive shunt impedance $-k_M L$. The factor $k_M$ depends on the parameters of the realized coupling element employed for the coupling.

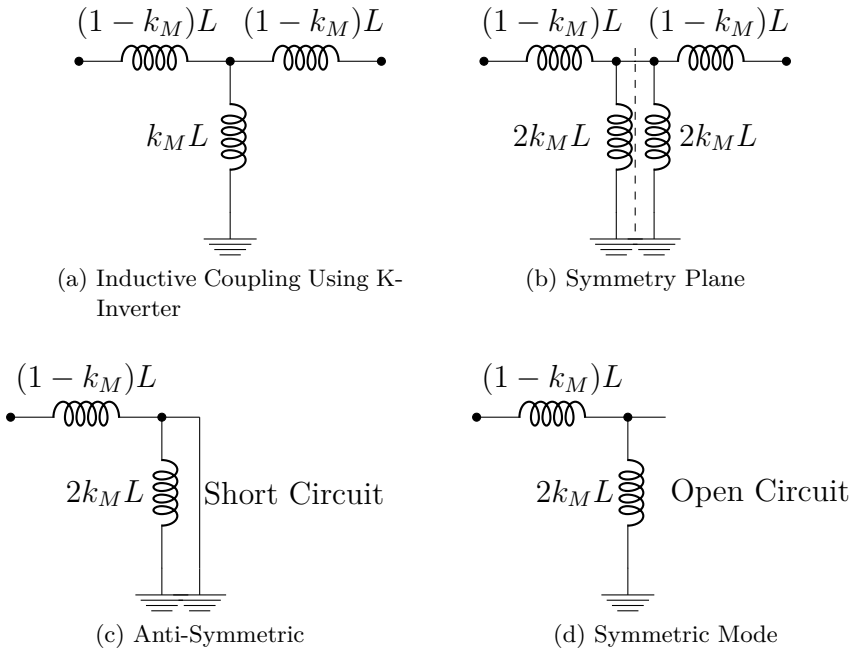


(a) Inductive Coupling Using K-Inverter

(b) Symmetry Plane

(c) Anti-Symmetric

(d) Symmetric Mode

Figure 4.15: Inductive Coupling using Inverters

- By inserting a symmetry plane as shown in Fig.4.15b which is a model for the bisected cavity, two possibilities of the split resonance frequencies occur.
- While treating the symmetry plane as an electric wall or a short circuit, as shown in Fig.4.15d, the total inductance of the cavity reduces to $(1-k_E)C$. The resonance frequency of the split mode is given as [Zverev, 2005; Jia-Sheng Hong and Lancaster, 1996],

$$f_{anti-symmetric} = \frac{1}{2\pi\sqrt{(1-k_M)LC}}. \tag{4.20}$$

- While treating the symmetry plane as a magnetic wall or an open circuit, as shown in Fig.4.15c, the stored magnetic energy increases and the inductance of the cavity is given by $(1+k_M)L$, as discussed in Sec.4.2.2 (see Fig.4.12b). This represents the resonance frequency of the split mode given by [Zverev, 2005; Jia-Sheng Hong and Lancaster, 1996],

$$f_{symmetric} = \frac{1}{2\pi\sqrt{(1+k_M)LC}}. \tag{4.21}$$

## 4.3 Computational Model

The three-dimensional model of the bisected $TM_{010}$ cavity is created with the aid of CST Microwave Studio [Computer Simulation Technology, 2017]. The model consists of the circular coupling apertures of both electric and magnetic nature in the metal wall of finite thickness bisecting the cavity. A large number of parametric runs are carried out in order to compute the optimized dimensions of required electric and magnetic apertures as well as the thickness of the metal sheet in the proposed bisected cavity. The primary specification that needs to be fulfilled by the proposed design comprises the ability of the sensor to differentiate between the longitudinal sample flow along the axis and its lateral offset from the axis. This specification is met by the presence of a single electric aperture that divides the sensing column of the cavity and results in two different field orientations due to the characteristic symmetric and anti-symmetric modes. Figure 4.16 shows the simulated representation of the electric field distribution and orientation for anti-symmetric and symmetric modes formed due to the presence of the electric aperture in the middle of the sensing column and the cavity. The anti-symmetric mode remains

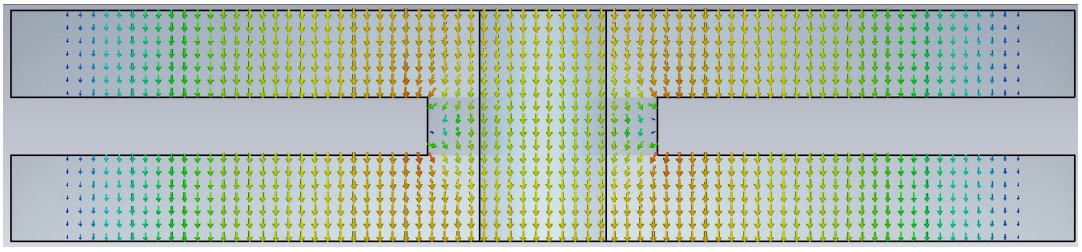

(a) Anti-symmetric Mode

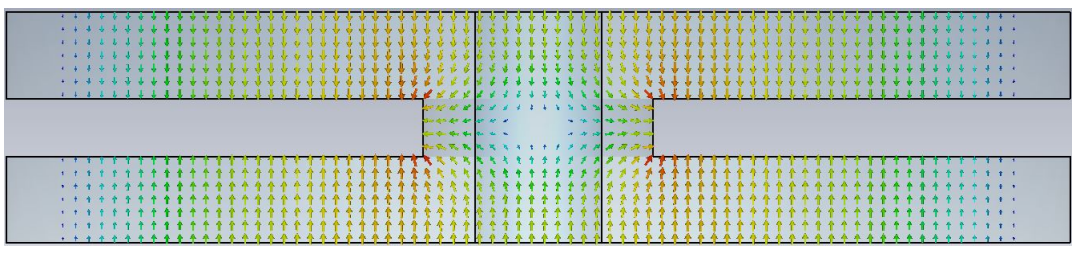

(b) Symmetric Mode

Figure 4.16: Split Resonances in a Bisected Pill-Box Cavity

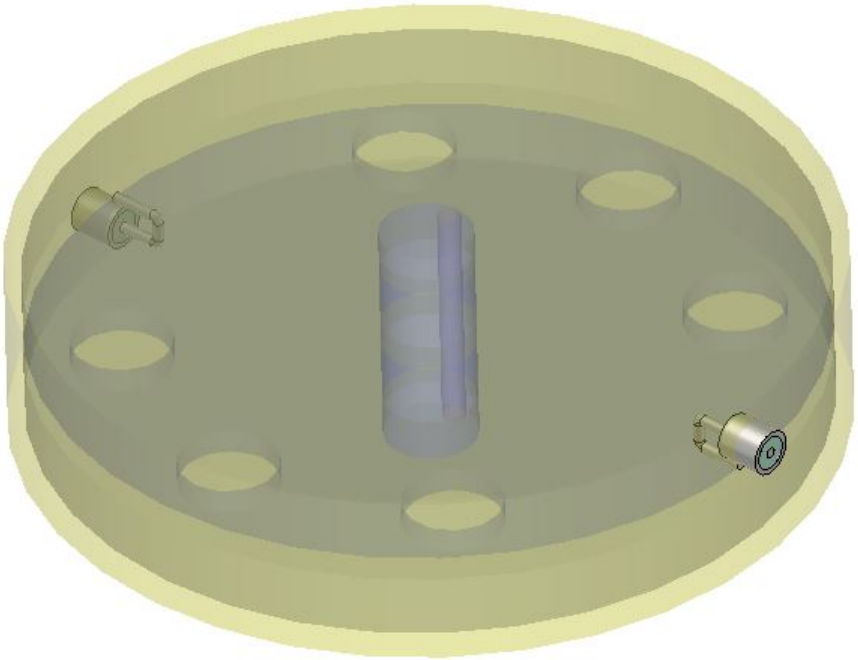

Figure 4.17: Coupled Cavity Design - 3D Perspective View

mostly unaffected in the vicinity of the aperture due to the electric wall effect in the transverse plane of the aperture. The symmetric mode undergoes a null at the center of the transverse plane of aperture due to the magnetic wall effect. Moreover, the symmetric mode has a relatively strong radial component of the electric field at the aperture inner walls in comparison to the anti-symmetric mode due to the inner wall boundary of the aperture acting as a virtual ground. This useful property can be employed to detect the offset movements of the sample flowing through the cavity towards or away from the axis. A secondary requirement of the sensor is to adjust the coupling strength between the cavity sections by inclusion of either electric or magnetic or both types of apertures to operate the proposed coupled resonator at two closely placed frequency modes within the 2.4 GHz to 2.5 GHz ISM band. A mix of the electric $k_E$ and the magnetic couplings $k_M$ are employed to ensure that the coupled frequencies are separated enough to be detectable yet close enough to lie within the specified band. The frequency of the symmetric coupled mode can be set to greater or lower than the fundamental frequency of the $TM_{010}$ mode, i.e. the anti-symmetric mode, as the former is a function of the dimensions and the type of the coupling apertures in the finite thickness sheet bisecting the cavity. For desired ISM band operation between 2.4 GHz to 2.5 GHz the anti-symmetric mode can be set by scaling of the radial dimension of the cavity. For instance, setting the dominant $TM_{010}$ mode or the anti-symmetric mode at 2.49 GHz and the symmetric coupled mode at 2.44 GHz can be adapted for sensing low-loss materials. In such a configuration, the detuning remains within the limits of the ISM band particularly for low loss and medium permittivity materials.

### 4.3.1 Simulation Model

A three-dimensional model of the cavity that includes both electric and magnetic apertures is depicted in Fig.4.17. The design specifications are as follows:

- The main resonating half-section consists of a cylindrical cross section frame of radius measures 46.25 mm and the longitudinal dimension referred to as length of the cavity

dimensioned at 7.5 mm. The other half-section vertically placed over the first half makes the total length of the cavity 15 mm in addition to the thickness of the bisecting metal sheet. Such a relatively flat pillbox cavity design, with height less than the cavity radius is preferable for high spatial measurement resolution in limited space conditions. In addition, the difference between anti-symmetric and symmetric mode is more prominent when the aperture volume is comparable to the overall volume of the cavity.

- Similar to the previous design, through-hole openings of radius 5.5 mm are present in the cavity top and bottom walls for sample flow through the sensing column along the length of the cavity.

- A metal plate of finite thickness for provision of inter-cavity coupling apertures is loaded in between the two halved sections of the cavity. The strength of the longitudinal and the radial electric field components in each of the respective anti-symmetric and symmetric modes is optimized through numerical evaluation of radius and thickness values of the electric coupling aperture. The parametric computation carried out in CST Microwave Studio [Computer Simulation Technology, 2017] for the variations in radius and thickness of the metal sheet containing the apertures are performed with variables depicted in Table.4.1. The radius of the circular aperture, labeled as $s1$ to $s4$, is varied from 3.5 mm to 10 mm in four discrete steps. Similarly, the thickness of the metal wall or the aperture, labeled as $t1$ to $t4$, is varied from 0.5 mm to 5 mm.

  The effect of electrical coupling $k_E$ on the frequency separation by introducing an aperture in the center of the bisecting metal wall while employing a pill-box $TM_{010}$ cavity can be formulated as

$$k_E = \frac{f_2^2 - f_1^2}{f_2^2 + f_1^2} \qquad \text{with} \qquad f_2 > f_1, \tag{4.22}$$

  where $f_1$ is the anti-symmetric mode and $f_2$ is the symmetric resonance mode. The relation implies that the value of the $k_E$ directly influences separation between mode frequencies. In terms of geometry $k_E$ is a function of the aperture radius and the thickness as well the overall cavity length, which can be simply stated as the ratio of effective volumes of the aperture $V_a$ and the cavity $V_c$ [Wheeler, 1964],

$$k_E = \frac{V_e a}{4 V_e c}. \tag{4.23}$$

  In order to isolate the effects of frequency separation and strength of the radial component other coupling means are required. Therefore, magnetic coupling was also introduced in the design to essentially fix the frequency separation between the symmetric and anti-symmetric modes. The electric aperture is primarily used to only optimize the radial electric field strength irrespective of the frequency separation.

- An additional set of six radially symmetric apertures of radius 5.75 mm are provided along the perimeter of the metal sheet. Due to the location the outer apertures with center at 37 mm, since the peak magnetic field occurs at 0.76 times the radius [Lin and Afsar, 2006], provide for the magnetic coupling resulting in an overall mixed inter-resonartor coupling between the two cavity segments. The relation between magnetic coupling $k_M$ and its influence on frequency separation between the symmetric and anti-symmetric modes can be stated as

$$k_M = \frac{f_1^2 - f_2^2}{f_2^2 + f_1^2} \qquad \text{with} \qquad f_1 > f_2, \tag{4.24}$$

Table 4.1: Labelling of Aperture Size and Thickness

| Symbol | Aperture Radius mm |
|---|---|
| $s1$ | 3.5 |
| $s2$ | 5.5 |
| $s3$ | 7.5 |
| $s4$ | 10.0 |
| Symbol | Sheet Thickness mm |
| $t1$ | 0.5 |
| $t2$ | 1.0 |
| $t3$ | 3.0 |
| $t4$ | 5.0 |

which implies that the symmetric mode $f_2$ is shifted towards right, i.e. the lower frequency point relative to the anti-symmetric mode $f_1$, an effect opposite of the electric coupling.

- The cavity is fed via a pair of loops diametrically opposite to each other around the circular periphery of the cavity. One loop is coupled to the top and the other to the bottom section of the cavity. It is to be noted that while performing measurements using the prototype various loop lengths were tested to observe the effect of external coupling on the sensitivity of the cavity.

### 4.3.2 Simulation Results

The computational scheme for evaluation of the longitudinal and the radial components of the electric field are already discussed in detail in Sec.3.3.1. The electric field components across unit radius columns are root mean squared and then summed along the whole column length using stepwise horizontal computational lines for both the anti-symmetric and the symmetric resonance modes. Additionally, the area bounded by the electric aperture in the center of the cavity is also included in each unit radius column. The numerical evaluation of the electric field across the sensing column provides functional understanding of the anti-symmetric and symmetric resonance modes for varying the radius and the thickness of the central electric aperture. It is validated from the computation results that the radial component $E_r$ and the axial or longitudinal electric field $E_z$ vary in magnitude due to changing aperture dimensions for the respective symmetric and anti-symmetric modes. A selection of the computational results for the normalized magnitude of the electric field components is provided as bar graphs from Fig.4.18 to Fig.4.23. Each bar refers to the position of the unit radius columns inside the sensing column with respective normalized strength of axial and radial components. The computational results related to the magnitude of the normalized electric field within the sensing column are explained below:

- Figure 4.18 depicts the column-wise distribution of the electric field in the cross section of the sensing column without the insertion holes for varying radius values of the electric aperture with fixed magnetic apertures. The computation shows that the normalized longitudinal electric field $E_z$ for the anti-symmetric mode reduces to roughly 2 % in magnitude along the radial axis relative to its magnitude at the center. The variations in the $E_z$ component of the anti-symmetric mode are in accordance with the zero order Bessel function. The symmetric mode exhibits larger variations of the $E_z$ component of approximately 20 % with an opposite slope compared to the anti-symmetric mode, i.e. increasing away from the axis relative to its magnitude at the center. The increase in slope is due to the cancellation of the $E_z$ component at the center of the electric aperture for the symmetric mode. The normalized $E_r$ component for the anti-symmetric mode is almost

negligible showing a slight increase away from the axis only due the vicinity to the aperture walls. The radial component $E_r$ of the symmetric mode exhibits larger variations of 40 % to 50 % increasing in magnitude towards the boundary of the aperture inner wall. The difference between the magnitude of $E_r$ component of the anti-symmetric mode and the symmetric mode for the cavity without insertion holes indicates that the anti-symmetric field distribution is largely independent from the influence of the dimensions of the electric aperture in the principal axis. The predominant influence of the electric aperture on the $E_r$ component of the symmetric mode as compared to to the negligible effects on the anti-symmetric mode can be employed to advantage. It can serve to provide different functionalities of sensing and detection due to the orientation of the respective modes. In addition, it is apparent from the Fig.4.18 that the overall difference between the electric field components of the anti-symmetric mode and the symmetric mode reduces for smaller aperture sizes. This property can be attributed to the reduced $k_E$ coupling resulting in even and odd impedances whose values are close to each other, as is the case of weakly coupled transmission lines in Eq.(4.11) and Eq.(4.12).

- Similarly, Fig.4.19 shows the result for the cavity in the presence of insertion holes of radius 5.5 mm. By comparing the results of the cavities with and without the insertion holes, it can be deduced that the increase in the radial component $E_r$ for the anti-symmetric resonance mode is largely due to the presence of the insertion holes and reduces to a minimal variation for the closed cavity, as discussed and illustrated in the computation results of Fig.4.18. Moreover, equal variations for different radius parameters of the electric aperture also validate that the influence on the $E_r$ component of the anti-symmetric mode is mainly due to the insertion holes irrespective of the dimensions of the electric aperture. On the other hand, the $E_r$ component of the symmetric mode shows a proportional increase, depicted in Fig.4.19, due to the additional effect of the insertions holes besides the direct influence of the dimensions of the electric aperture on the corresponding radial field.

- Figure 4.20 and 4.21 refer to the computational results for the fixed 5.5 mm aperture radius with and without the insertion holes, respectively. The parametric variations are performed for the changing thickness value of the bisection metal sheet. A thicker aperture reduces the coupling due to the increased decay inside the hole. Therefore, the $E_z$ fields of the anti-symmetric and the symmetric modes with fixed insertions holes in Fig.4.21 are comparable for the $t4$ value, i.e. the 5.0 mm thick metal sheet. In practice, a strong coupling $k_E$ with a reduced decay is desired which can be fulfilled with a minimum possible thickness of the aperture. Moreover, a thicker aperture also shows an increase in the relative magnitude of the $E_r$ component of the anti-symmetric mode which means a reduced distinguishing factor between the anti-symmetric and symmetric mode.

- In addition, Fig.4.22 as well as Fig.4.23 are used for larger electric apertures of 15 mm and 20 mm, respectively. The increased coupling $k_E$ causes an increase in the difference between the longitudinal component $E_z$ of the anti-symmetric and the symmetric mode. Moreover, the change in the slope of the $E_r$ is less pronounced than for the symmetric modes, which implies a decreased sensitivity to the offset movement of the sample.

## 4.4 Cavity Prototype and Measurement

### 4.4.1 Prototype Description and Setup

A cylindrical cavity prototype for measurement was constructed from aluminium using the milling procedure. The cavity radius is dimensioned at 46.25 mm and two half sections called the base and the cover of the resonator are milled with a depth profile of 7.50 mm, i.e. the length

of half the cavity, as illustrated in the cavity drawings of Figs.4.24 and 4.25. Through-holes of radius 5.5 mm are milled in the base and cover sections of the cavity, as shown in Fig.4.25a. Additionally, apertures in the metal sheet of thickness 1.00 mm are provided for inter-cavity coupling, as depicted in Fig.4.25b. The sheet contains a total of seven apertures, that includes an electric aperture of 5.5 mm in the center and three pairs of radially symmetric magnetic apertures with radius 5.75 mm and center located at 35 mm from the axis. The construction of apertures in the metal sheet portion directly above the external coupling loops, marked by diametrically placed notches in Fig.4.25b, is avoided to minimize the influence of the external coupling on the inter-cavity coupling. The metal sheet is placed in between and attached to the resonator base and cover part using metallic screws. The finished prototype of the cavity sensor along with the metal sheet is shown in Fig.4.26. The holes for the assembling screws are visible besides the SMA connector with a small loop soldered to the cavity inner wall for the

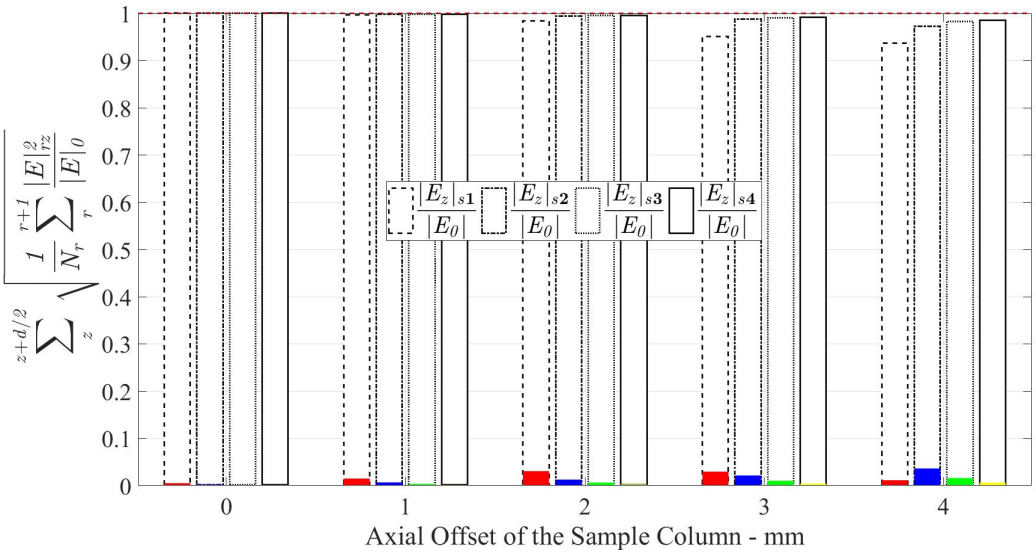


(a) Anti-symmetric Mode

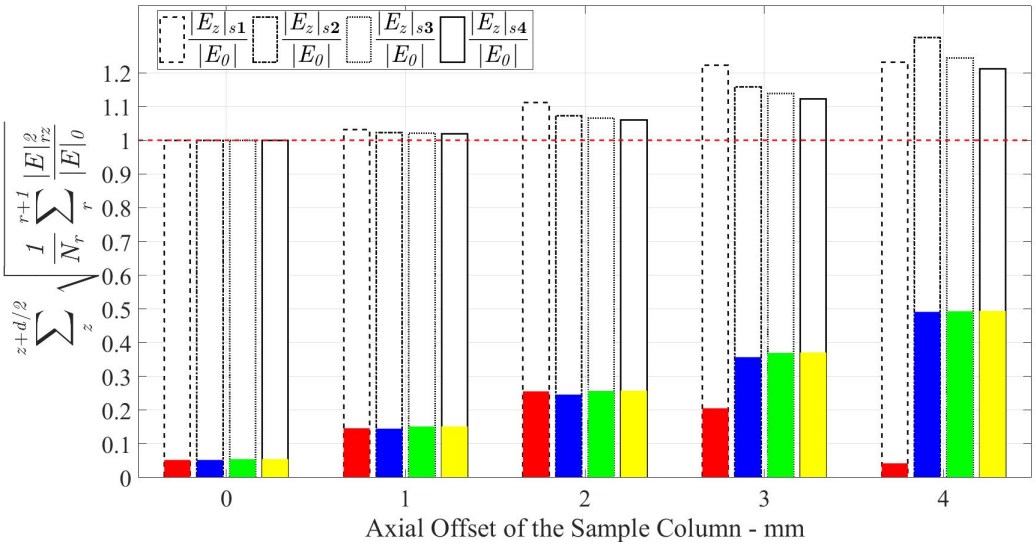


(b) Symmetric Mode

Figure 4.18: Normalized Components of the Electric Fields inside the Sensing Region: Varying Diameters of the Electric Apertures / No Insertion Holes

purpose of excitation of the cavity.

The measurement setup consisted of a vector network analyzer to record the transmission coefficients of the two-port cavity. The network analyzer was calibrated to a frequency band between 2.4 GHz to 2.5 GHz with 0 dBm power level and a step bandwidth of 10 kHz. The cavity was mounted on a custom-built structure referred to as the mounting frame in order to perform measurements for both the varying sample positions and changing linear mass density. The frame provided the means to attach single as well as multiple textile fibers/threads that pass through the insertion holes of the cavity mounted and fixed on a platform, as demonstrated in Fig.4.27. A thread of diameter of approximately 2 mm made up of 100 % cotton is used as the sample under test. A spring loaded mechanism is connected to a micrometer gauge to move the thread linearly in both directions. A single thread passing from top to bottom through

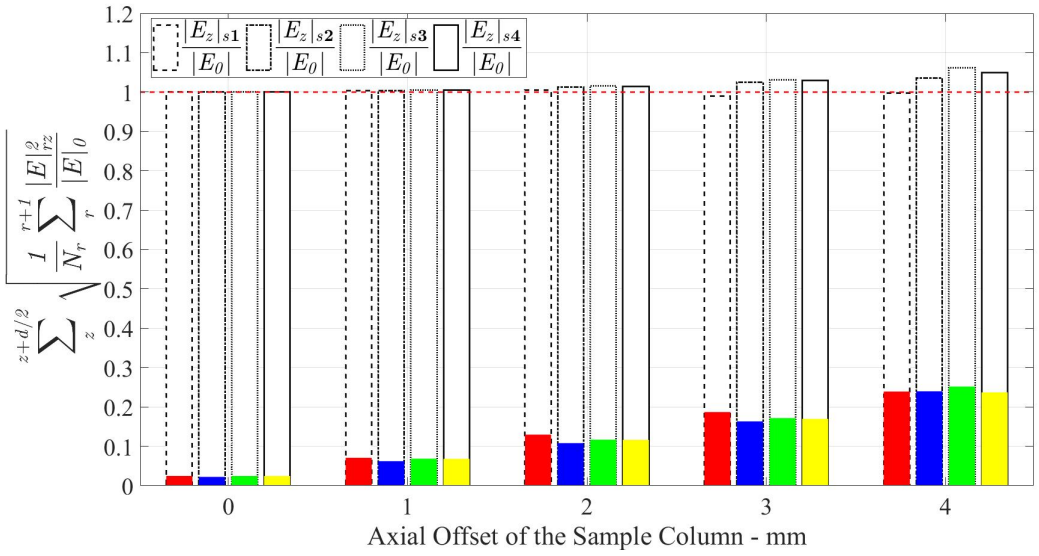


(a) Anti-symmetric Mode

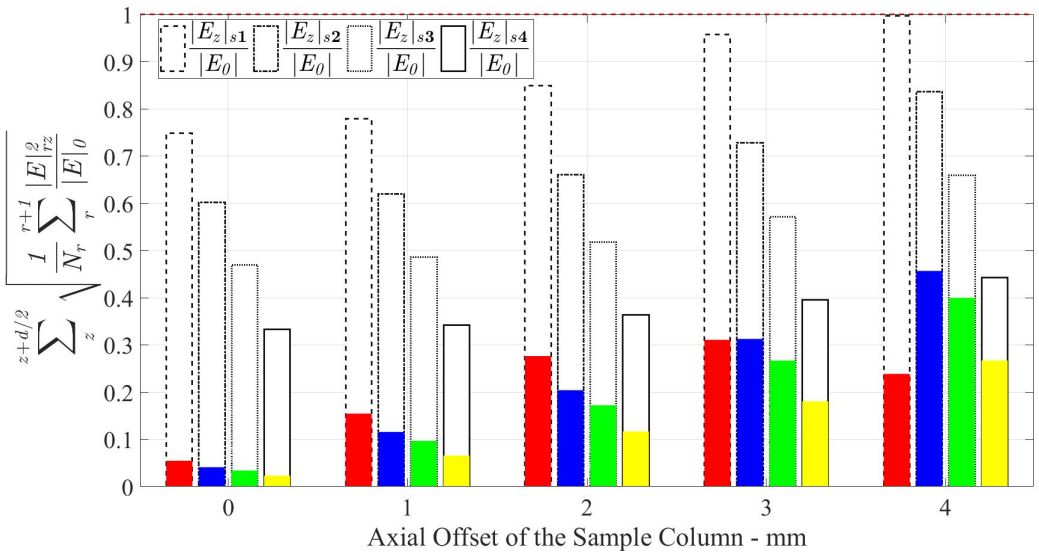


(b) Symmetric Mode

Figure 4.19: Normalized Components of the Electric Field inside the Sensing Region: Varying Diameters of the Electric Apertures / Fixed Diameter = 11 mm of the Insertion Holes

the cavity can be aligned concentric to the sensing region using the micrometer. To perform the sample offset test the thread can be moved using the screw gauage to emulate the effect of position offset from the center towards the inner boundary walls of the insertion holes. To emulate the increase in mass number of threads are added together and the effect was measured. Figure 4.28 shows the case of a single as well as multiple threads passing through the insertion hole.

### 4.4.2 Measurement Results

The measurement of cavity detuning for a single thread with changing positions inside the sensing column and the measurement for multiple threads were performed. The measured $S_{21}$

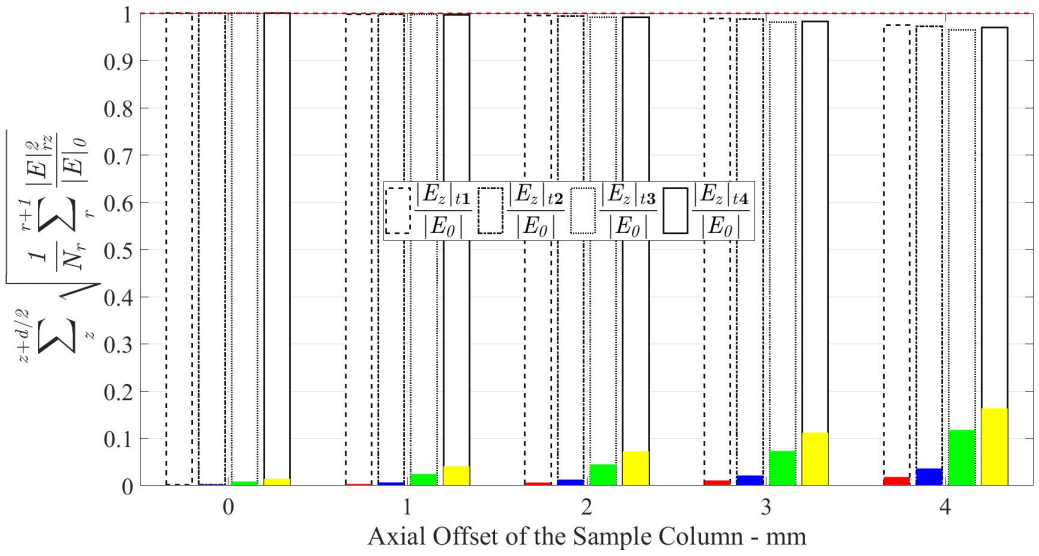


(a) Anti-symmetric Mode

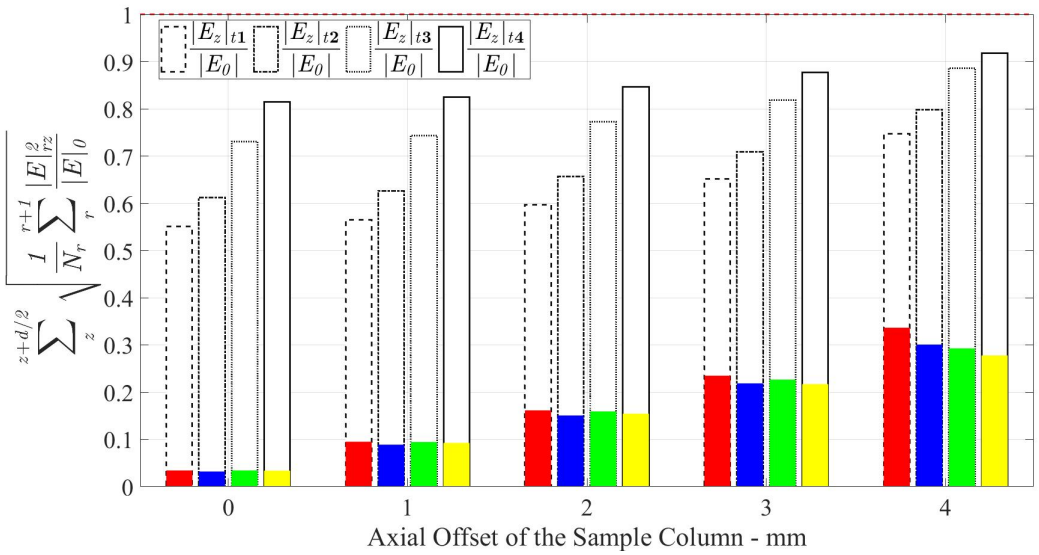


(b) Symmetric Mode

Figure 4.20: Normalized Components of the Electric Field inside the Sensing Region: Fixed Diameter = 11 mm of the Electrical Apertures with Varying Thickness of the Aperture / No Insertion Holes

values for a single cotton thread with varying offset away from the axis were recorded for the symmetric and the anti-symmetric modes. The difference in resonance shift or detuning due to change in mass density by using multiple threads was also undertaken for both operating modes. From the detuning values it can be deduced that the anti-symmetric resonance mode responds with higher sensitivity to changes in mass emulated by the increase in number of threads, whereas the symmetric mode shows increased sensitivity to the sample offset.

**Effect of position offset:** A variable called eccentricity is defined as a pointer to the sample position inside the sensing region with the concentric point marked as 0 mm. As the cotton thread sample is moved stepwise from the center towards the inner periphery of the insertion hole the eccentricity value gradually increases to 3.5 mm. A number of readings are taken for the sample movement from the axial center of the sensing region, i.e., offset 0 mm, towards the

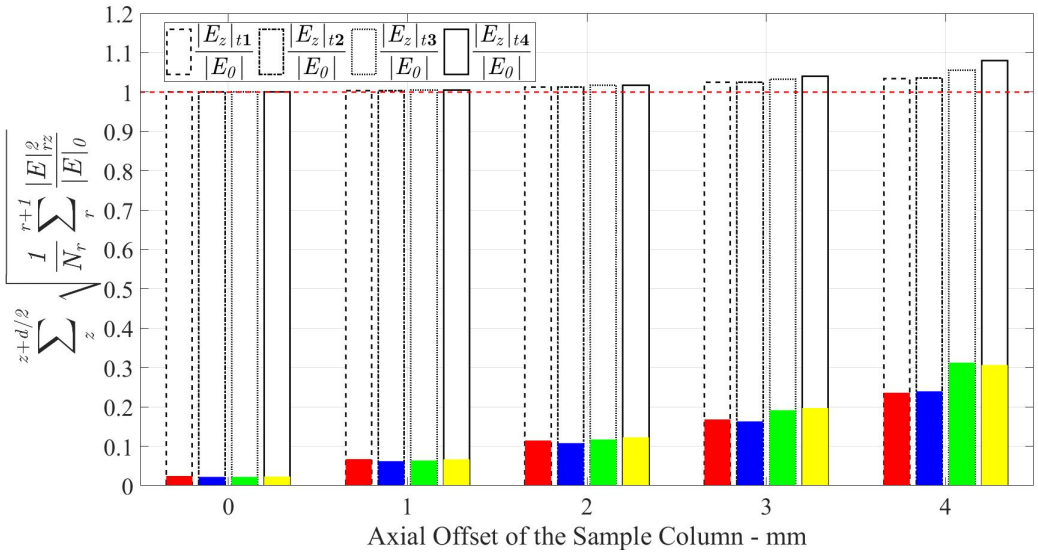


(a) Anti-symmetric Mode

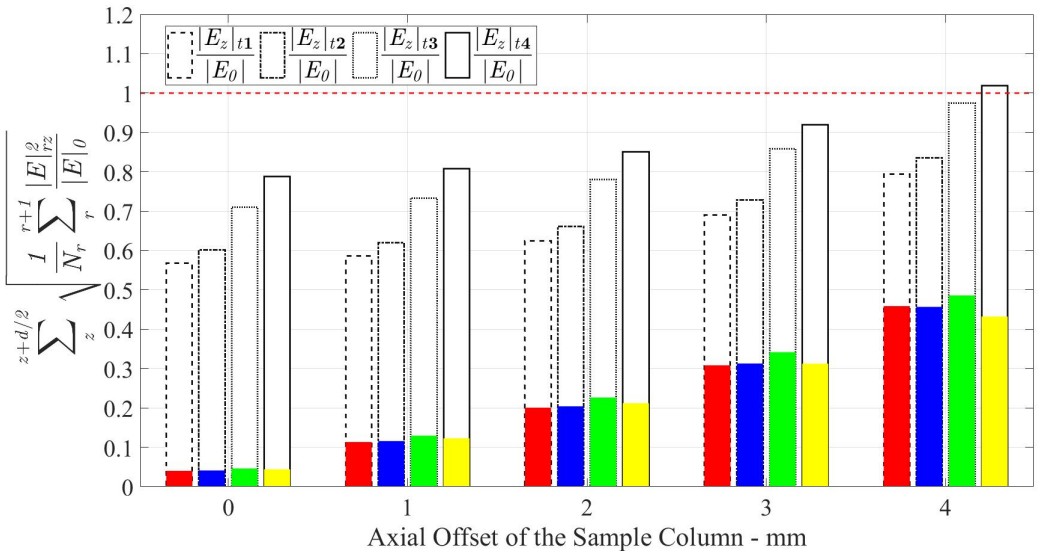


(b) Symmetric Mode

Figure 4.21: Normalized Components of the Electric Field inside the Sensing Region: Fixed Diameter = 11 mm of the Electrical Apertures with Varying Thickness of the Aperture / Fixed Diameter = 11 mm of the Insertion Holes

boundary wall, i.e., offset 3.5 mm position with step sizes of 0.5 mm. The results of detuning sensitivity to change in sample offset of the anti-symmetric and the symmetric modes in terms of both the absolute and the percentage measures are depicted in Fig.4.29 and Fig.4.30 for two different external coupling values, respectively. Based on the length of the coupling loops connected to the feeding network, two different arrangements of external coupling are employed to record the effect of the external coupling due to the magnetic loops on the measurement.

**Effect of mass variation:** The functionality of the resonance modes for measuring change in thickness or mass density of the sample can be tested by adding more threads passing through the sensing region. The experiment was performed by increasing the number of sample threads in the sensing column for each reading. The anti-symmetric mode is more responsive as expected in comparison to the symmetric mode to changes in mass while testing for multiple threads

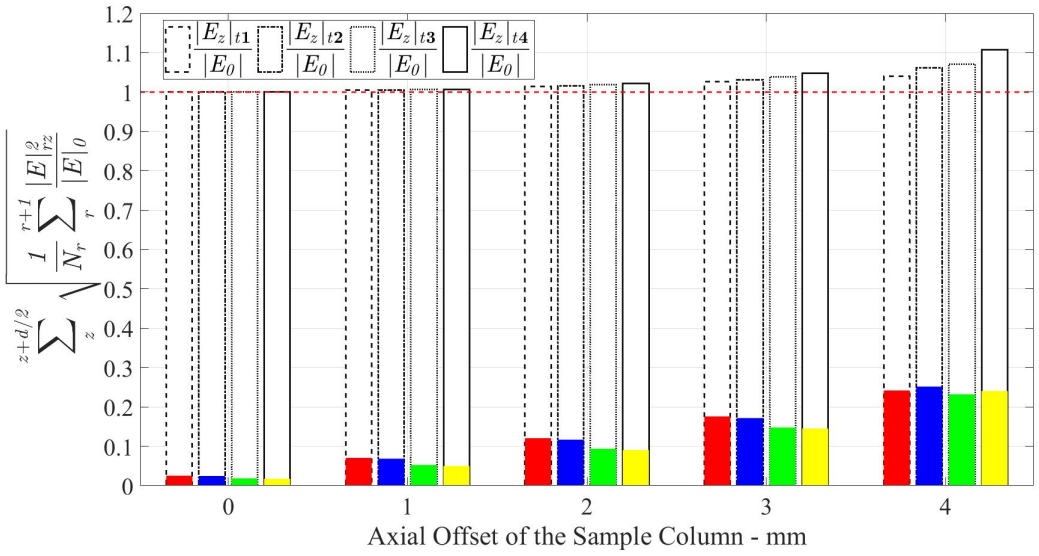


(a) Anti-symmetric Mode

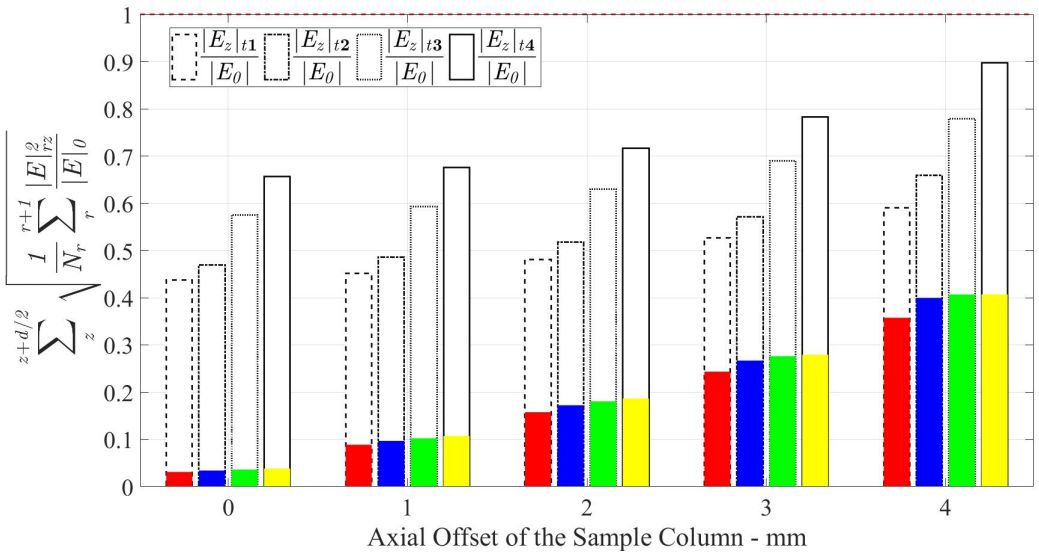


(b) Symmetric Mode

Figure 4.22: Normalized Components of the Electric Field inside the Sensing Region: Fixed Diameter = 15 mm of the Electrical Apertures with Varying Thickness of the Aperture / Fixed Diameter = 11 mm of the Insertion Holes

scheme. The results for the detuning sensitivity of the employed cavity resonator for respective anti-symmetric and symmetric modes in terms of absolute and percentage shift related to mass variations are shown in Fig.4.31.
Consequently, it can be deduced that the coupled cavity resonances for cylindrical structures can be effectively employed to perform two different functions of mass detection and position sensing simultaneously. The anti-symmetric mode functions like the conventional $TM_{010}$ mode and upon interaction with the dielectric specimen it provides the measure of mass or thickness based on the bulk permittivity of the material under test. The symmetric mode detects position offsets of the dielectric specimen away from the concentric axis of the sensing column. It is verified through simulations that the symmetric mode has reduced electric field component $E_r$ in the central sensing region but stronger electric field away from the axis. In addition, it is

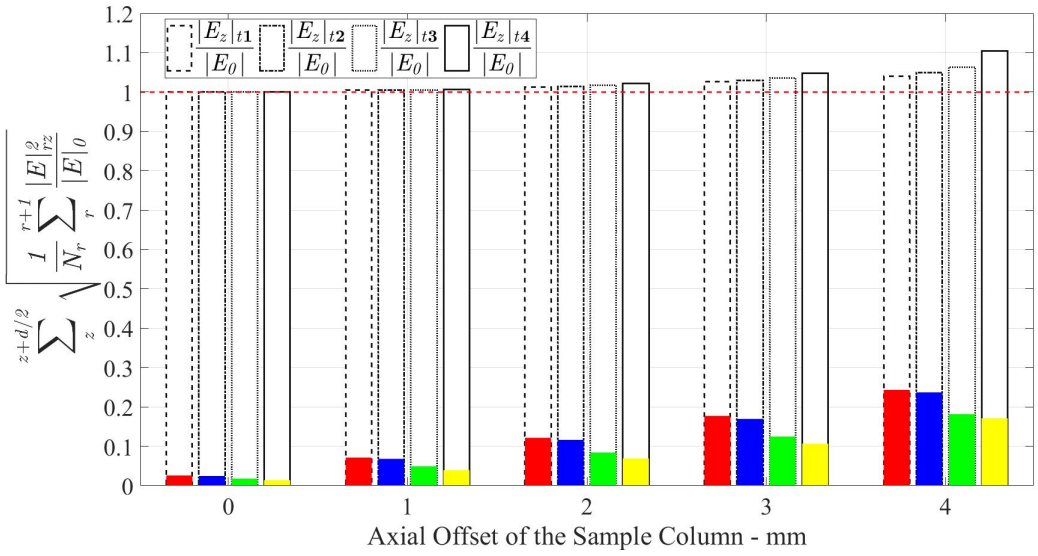


(a) Anti-symmetric Mode

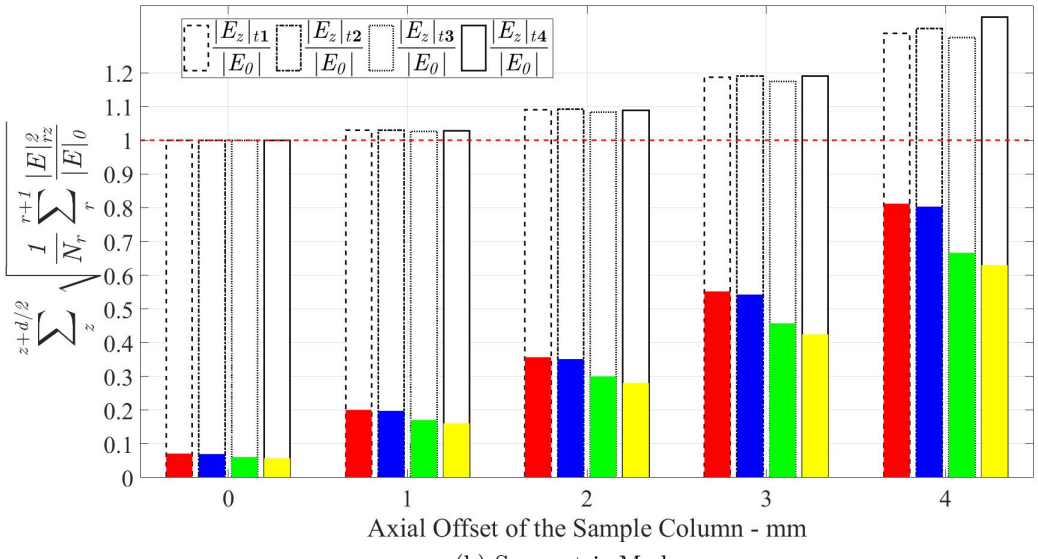


(b) Symmetric Mode

Figure 4.23: Normalized Components of the Electric Field inside the Sensing Region: Fixed Diameter = 20 mm of the Electrical Apertures with Varying Thickness of the Aperture / Fixed Diameter = 11 mm of the Insertion Holes

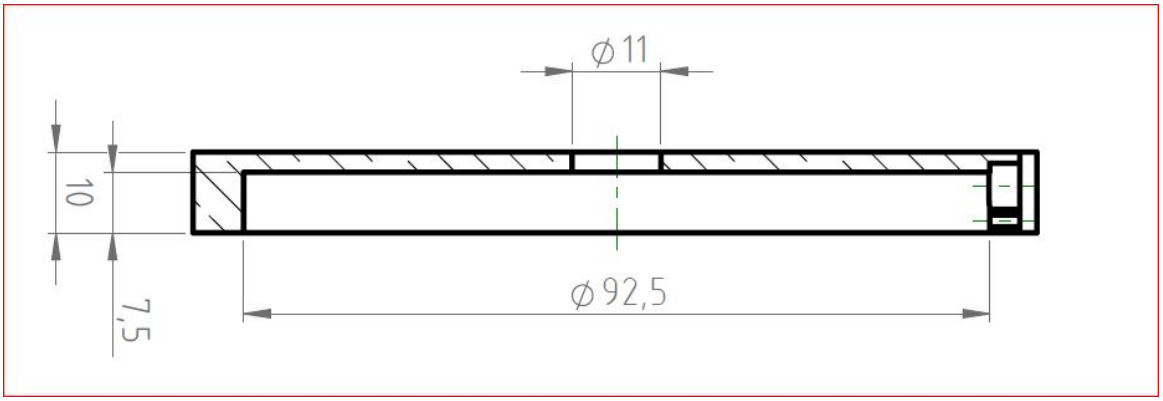


(a) Resonator Cover

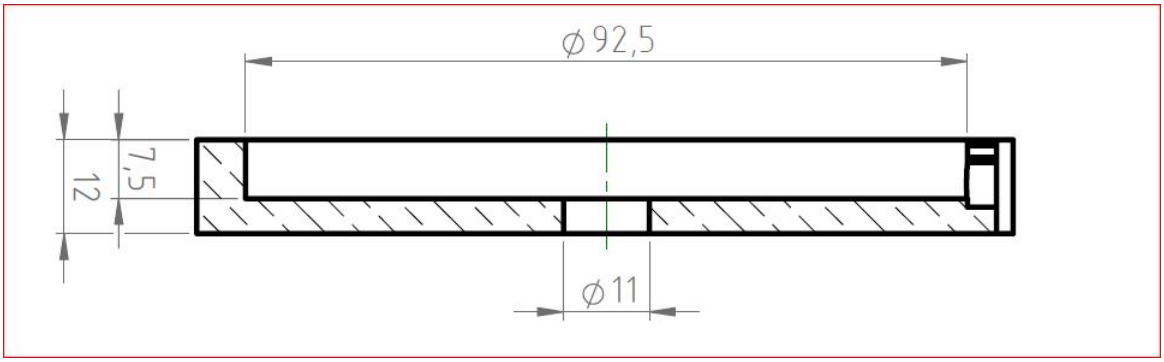


(b) Resonator Base

Figure 4.24: Construction Drawing of the Cavity Prototype

also verified through measurements of the cavity prototype that the minimum possible radius of the central aperture in the region of specimen flow increases the sensitivity of the proximity mode. Hence, the combination of both modes can be a significant advantage in measurement environments that require simultaneous detection of mass and position of the dielectric specimen which continuously streams through the cavity.

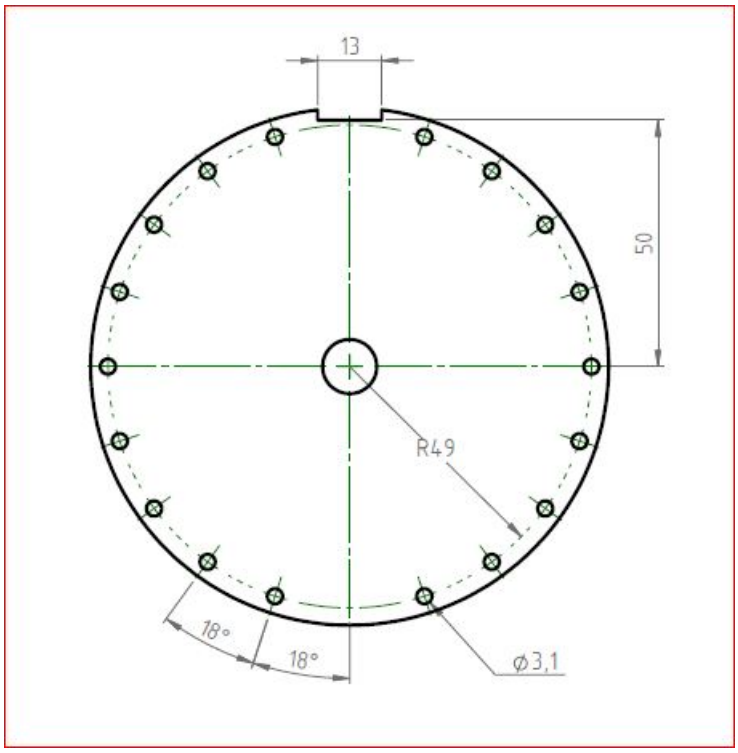


(a) Top/Bottom View of Resonator Base/Cover

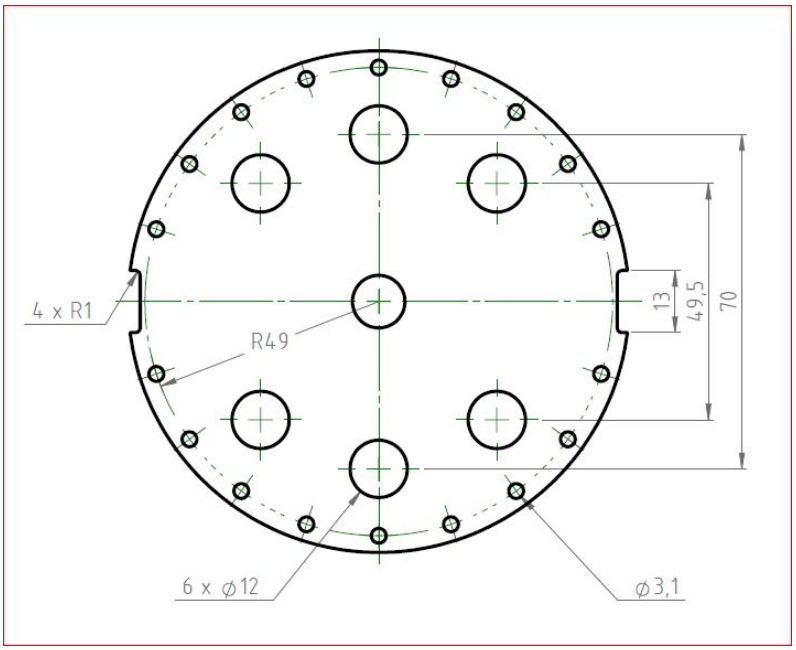


(b) Separation Sheet

Figure 4.25: Insertion Hole and Aperture Profile of the Cavity Prototype

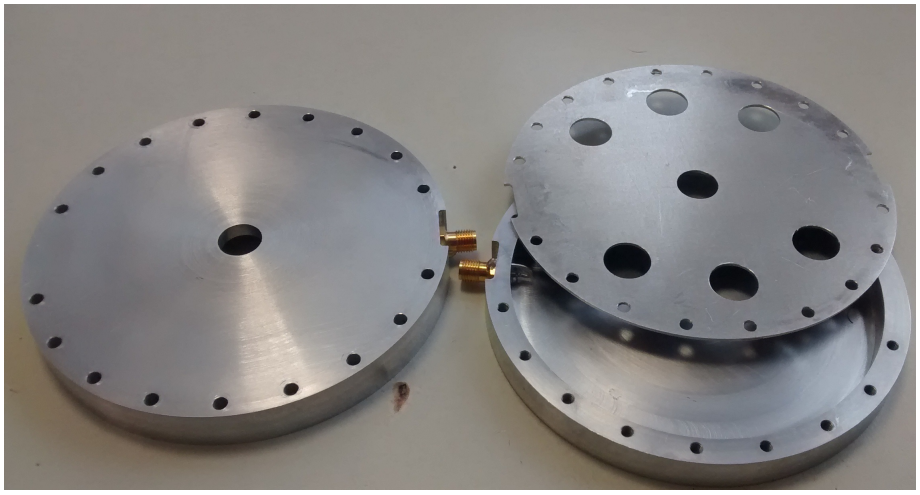

(a) Prototype Sections

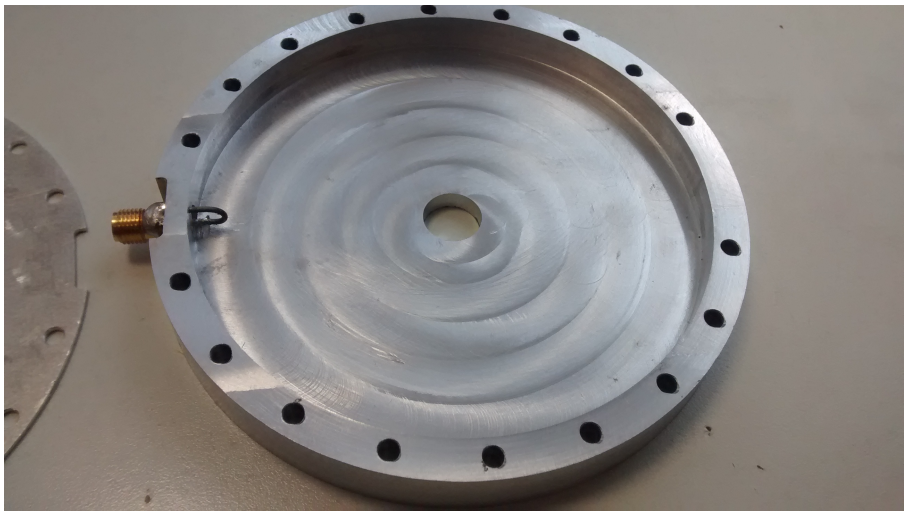

(b) External Coupling Loop

Figure 4.26: Milled Prototype

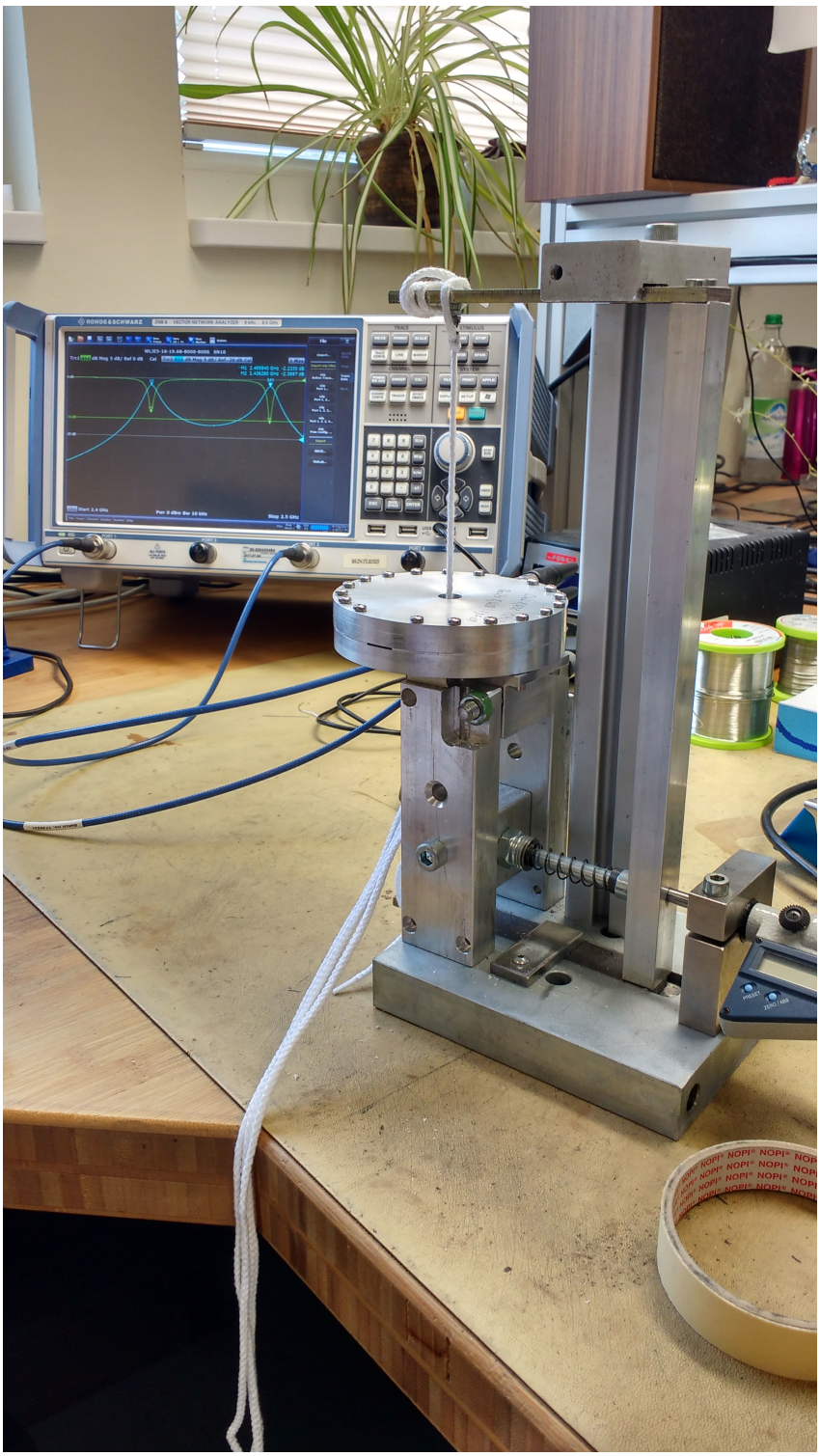


Figure 4.27: Measurement Fixture and Equipment

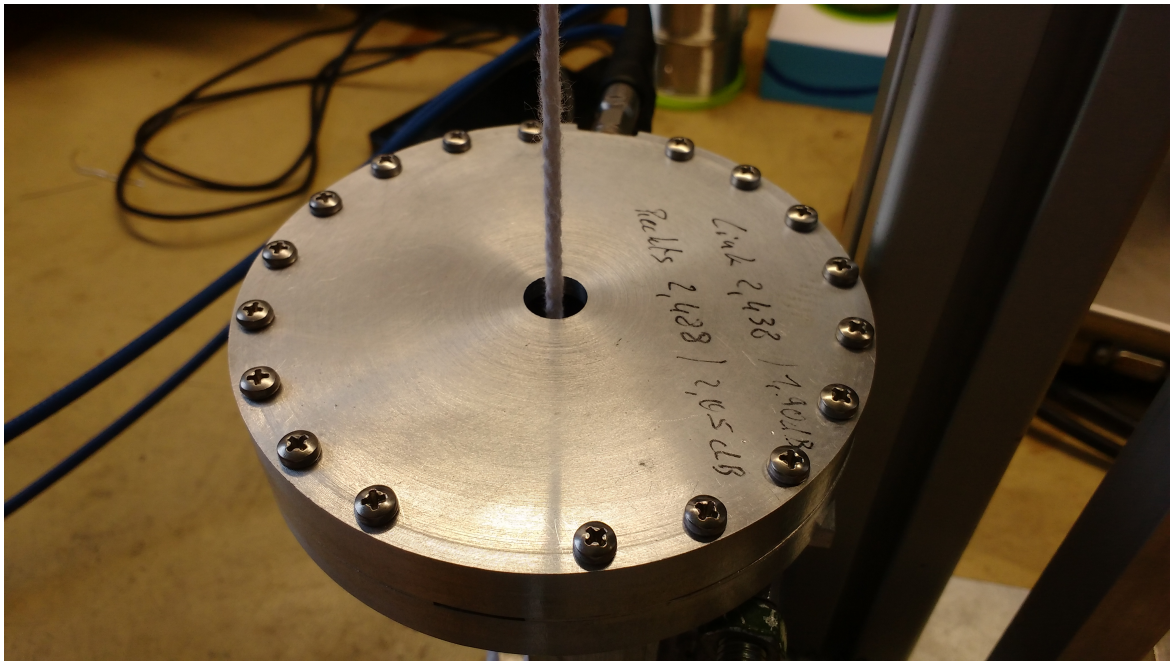

(a) Single Thread Measurement

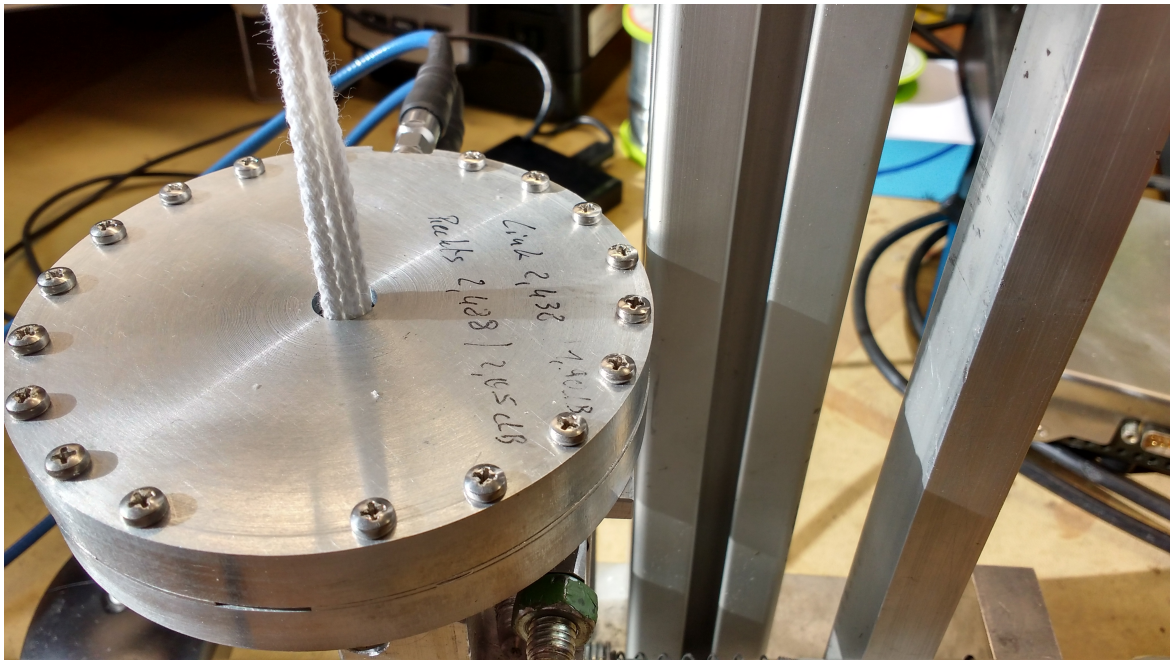

(b) Multiple Thread Measurement

Figure 4.28: Sample Offset Sensing

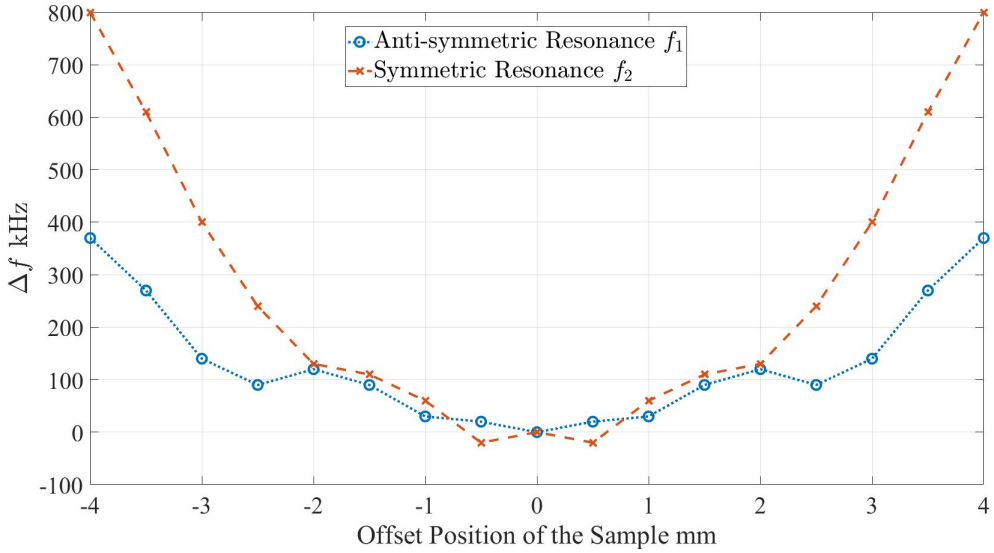


(a) Absolute Measure of Frequency Shift

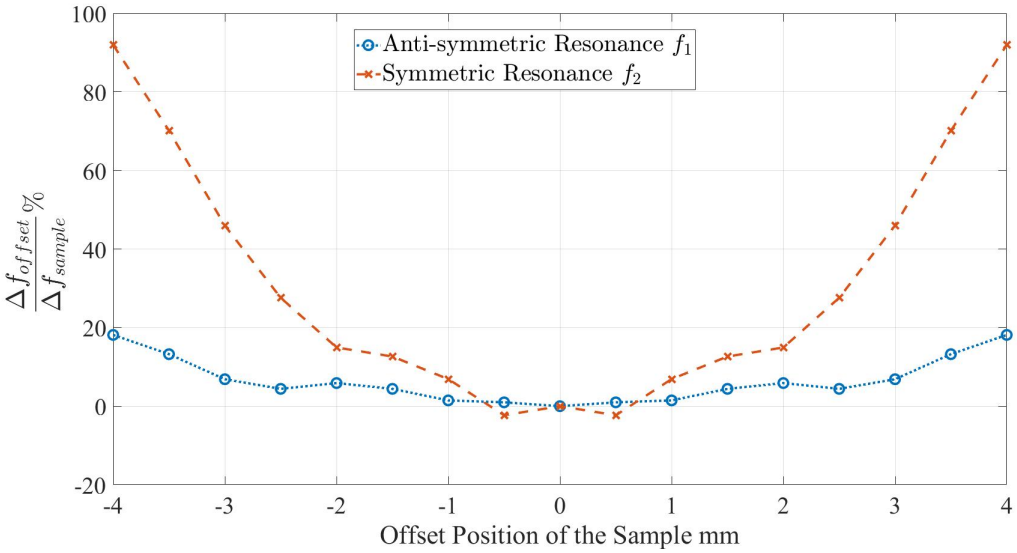


(b) Percentage Measure of Frequency Shift

Figure 4.29: Sample Offset Sensing for Relatively Weak External Coupling - Loop Length = 4 mm / $S_{21}$ = 2.0 dB

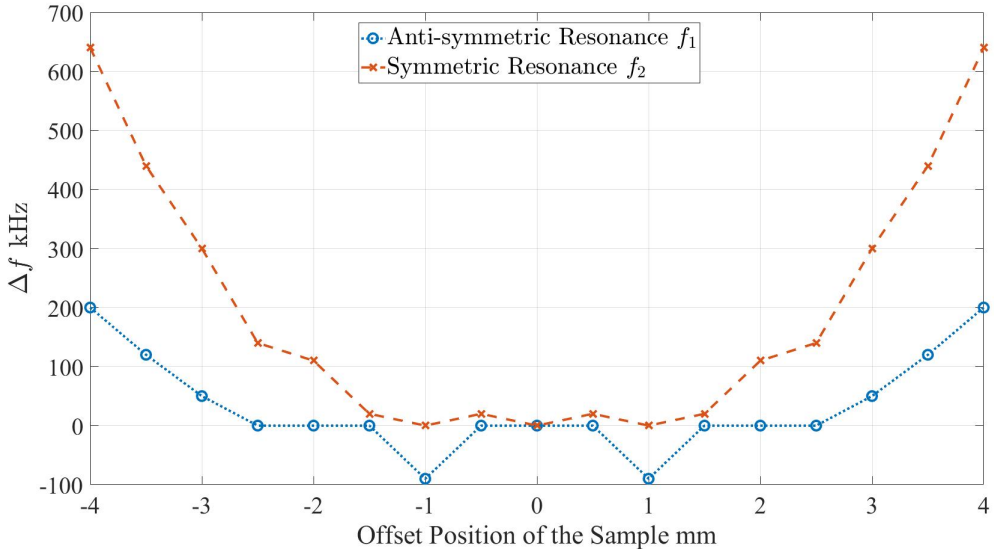


(a) Absolute Measure of Frequency Shift

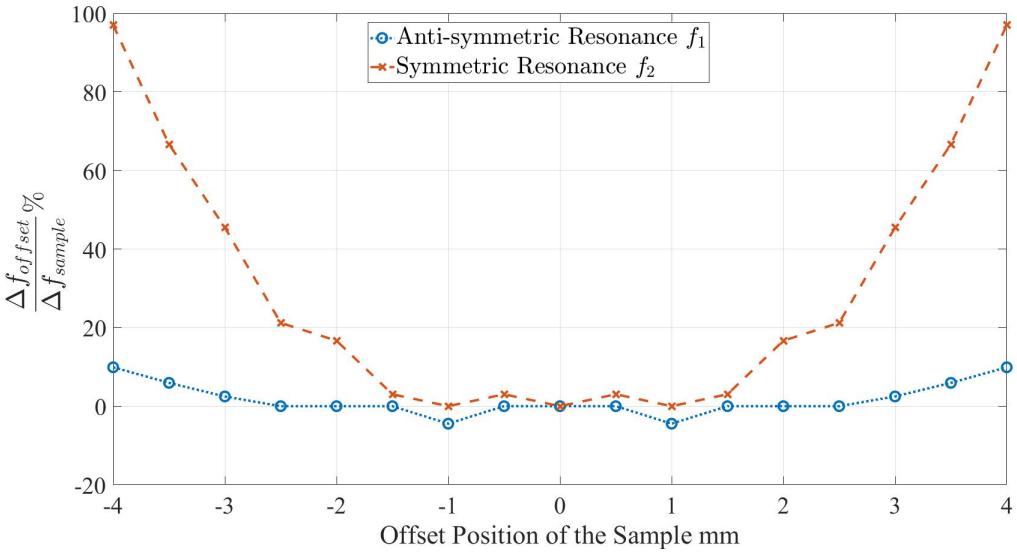


(b) Percentage Measure of Frequency Shift

Figure 4.30: Sample Offset Sensing for Relatively Strong External Coupling - Loop Length $= 7\,\text{mm}$ / $S_{21} = 1.0\,\text{dB}$

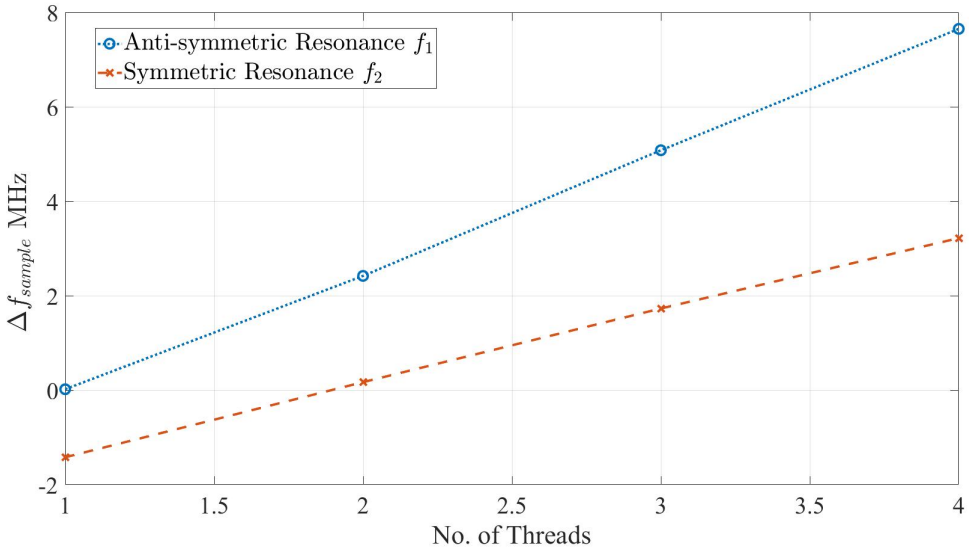


(a) External Coupling $S_{21} = 1.5\,\mathrm{dB}$

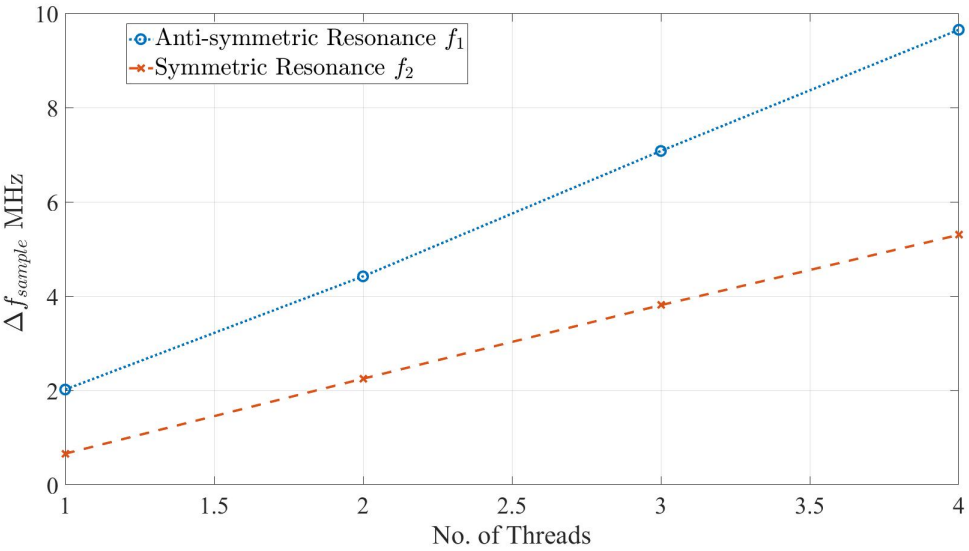


(b) External Coupling $S_{21} = 1.0\,\mathrm{dB}$

Figure 4.31: Sample Mass Sensing

# References


Afsar, M., Birch, J., Clarke, R., and Chantry, G. (1986). The measurement of the properties of materials. *Proceedings of the IEEE*, 74(1):183–199.

Baker-Jarvis, J., Geyer, R., Grosvenor, J., Janezic, M., Jones, C., Riddle, B., Weil, C., and Krupka, J. (1998). Dielectric characterization of low-loss materials: A comparison of techniques. *IEEE Transactions on Dielectrics and Electrical Insulation*, 5(4):571–577.

Baker-Jarvis, J., Janezic, M. D., and Degroot, D. C. (2010). High-frequency dielectric measurements. *IEEE Instrumentation and Measurement Magazine*, 13(2):24–31.

Bal, K. and Kothari, V. K. (2010). Permittivity of woven fabrics: A comparison of dielectric formulas for air-fiber mixture. *IEEE Transactions on Dielectrics and Electrical Insulation*, 17(3):881–889.

Balanis, C. A. (2012). *Advanced Engineering Electromagnetics*. John Wiley & Sons, New York.

Banos, A., Saxon, D. S., and Gruen, H. (1951). Propagation characteristics in a coaxial structure with two dielectrics. *Journal of Applied Physics*, 22(2):117–123.

Bethe, K. and Verweel, J. (1969). On dielectric losses at microwaves: Sensitive measurements and results. *IEEE Transactions on Magnetics*, 5(3):474–477.

Bussey, H. E. (1967). Measurement of RF properties of materials: A survey. *Proceedings of the IEEE*, 55(6):1046–1053.

Carter, R. G. (2001). Accuracy of microwave cavity perturbation measurements. *IEEE Transactions on Microwave Theory and Techniques*, 49(5):918–923.

Chao, S. H. (1985). Measurements of microwave conductivity and dielectric constant by the cavity perturbation method and their errors. *IEEE Transactions on Microwave Theory and Techniques*, 33(6):519–526.

Cohn, S. (1951). Determination of aperture parameters by electrolytic-tank measurements. *Proceedings of the IRE*, 39(11):1416–1421.

Cohn, S. (1952). Microwave coupling by large apertures. *Proceedings of the IRE*, 40(6):696–699.

Collin, R. E. (2001). *Foundations for Microwave Engineering*. Wiley-IEEE Press, New York.

Computer Simulation Technology (2017). *https://www.cst.com CST Microwave Studio 3D EM Solver*.

Dicke, R. H. and Purcell, E. M. (1948). *Principles of Microwave Circuits*. McGraw Hill Book Co., New York.

Dishal, M. (1949). Design of dissipative band-pass filters producing desired exact amplitude-frequency characteristics. *Proceedings of the IRE*, 37(9):1050–1069.

Dishal, M. (1951). Alignment and adjustment of synchronously tuned multiple-resonant-circuit filters. *Proceedings of the IRE*, 39(11):1448–1455.

Eastham, G. and Chang, K. (1991). Analysis and closed-form solutions of circular and rectangular apertures in the transverse plane of a circular waveguide. *IEEE Transactions on Microwave Theory and Techniques*, 39(4):718–723.

Estin, A. J. and Bussey, H. E. (1960). Errors in dielectric measurements due to a sample insertion hole in a cavity. *IRE Transactions on Microwave Theory and Techniques*, 8(6):650–653.

Faz, U. and Eibert, T. F. (2019). A coupled-cavity resonator technique for simultaneous mass and position detection of continuous dielectric material streams. *To be submitted*, -(-):–.

Faz, U., Siart, U., and Eibert, T. F. (2015a). A cylindrical cavity resonator for material measurements with coupled resonant modes for sensing and position offset compensation of the dielectric specimen. In *German Microwave Conference, Nuremberg*.

Faz, U., Siart, U., Eibert, T. F., and Hermann, T. (2015b). Electric field homogeneity optimization by dielectric inserts for improved material sensing in a cavity resonator. *IEEE Transactions on Instrumentation and Measurement*, 64(8):2239–2246.

Gajda, G., Gajda, G., and Stuchly, S. S. (1983). An equivalent circuit of an open-ended coaxial line. *IEEE Transactions on Instrumentation and Measurement*, 32(4):506–508.

Gajda, G. B. and Stuchly, S. S. (1983). Numerical analysis of open-ended coaxial lines. *IEEE Transactions on Microwave Theory and Techniques*, 31(5):380–384.

Gauthier, S., Marchildon, L., and Akyel, C. (1989). Shift of the complex resonance frequency of a dielectric-loaded cavity produced by small sample insertion holes. *IEEE Transactions on Microwave Theory and Techniques*, 37(4):801–804.

GE Data (2017). *http://www.quartz.com/gedata.html, Fused Quartz properties and usage guide*.

Getsinger, W. (1962). Coupled rectangular bars between parallel plates. *IEEE Transactions on Microwave Theory and Techniques*, 10(1):65–72.

Gluckstern, R. and Diamond, J. (1991). Penetration of fields through a circular hole in a wall of finite thickness. *IEEE Transactions on Microwave Theory and Techniques*, 39(2):274–279.

Gregory, A. P. and Clarke, R. N. (2006). A review of RF and microwave techniques for dielectric measurements on polar liquids. *IEEE Transactions on Dielectrics and Electrical Insulation*, 13(4):727–743.

Hamid, M. A. K. and Mostowy, N. J. (1974). Open circuit step cavity resonator for continuous monitoring of sheet moisture content. *International Journal of Electronics*, 37(4):511–520.

Harrington, R. F. (2001). *Time-Harmonic Electromagnetic Fields*. Wiley-IEEE Press, New York.

Helios Quartz (2017). *http://www.heliosquartz.com, Quartz glass production methods*.

Heraeus Quarzglas (2017). *https://www.heraeus.com, Making of fused Quartz and fused Silica*.

Hermann, T., Olbrich, G. R., and Russer, P. (2008). A novel microwave-based inspection system for continuously streaming materials using a cavity resonator. In *Proceedings of the 38th European Microwave Conference, Amsterdam*, pages 901–904.

Horner, F., Taylor, T. A., Dunsmuir, R., Lamb, J., and Jackson, W. (1946). Resonance methods of dielectric measurement at centimetre wavelengths. *Electrical Engineers - Part III: Radio and Communication Engineering, Journal of the Institution of*, 93(21):53–68.

Ikeda, M., Fukunaga, T., and Miura, T. (2003). Influence of sample insertion hole on resonant cavity perturbation measuring method. In *IEEE MTT-S International Microwave Symposium Digest, Philadelphia*, pages 1423–1426.

Janezic, M. D. and Baker-Jarvis, J. (1999). Full-wave analysis of a split-cylinder resonator for non-destructive permittivity measurements. *IEEE Transactions on Microwave Theory and Techniques*, 47(10):2014–2020.

Janezic, M. D., Kuester, E. F., and Jarvis, J. B. (2004). Broadband complex permittivity measurements of dielectric substrates using a split-cylinder resonator. In *IEEE MTT-S International Microwave Symposium Digest, Fort Worth*, pages 1817–1820.

Jia-Sheng Hong and Lancaster, M. (1996). Couplings of microstrip square open-loop resonators for cross-coupled planar microwave filters. *IEEE Transactions on Microwave Theory and Techniques*, 44(11):2099–2109.

Jones, E. T., Matthaei, L., and Young, L. (1980). *Microwave Filters Impedance-Matching Networks and Coupling Structures*. Artech House, Boston.

Kanpan, P., Khansalee, E., Puangngernmak, N., and Chalermwisutkul, S. (2012). $TM_{010}$ mode cylindrical cavity for complex permittivity measurement of liquid using field analysis technique. In *9th International Conference on Electrical Engineering/Electronics, Computer, Telecommunications and Information Technology, Thailand*, pages 1–4.

Kawabata, H. and Kobayashi, Y. (2005). Accurate measurements of complex permittivity of liquid based on a $TM_{010}$ mode cylindrical cavity method. In *Proceedings of the 35th European Microwave Conference, Paris*, pages 369–372.

Kawabata, H., Tanpo, H., and Kobayashi, Y. (2004). Analysis and experiments of a $TM_{010}$ cylindrical cavity to measure accurate complex permittivity of liquid. *IEICE Transaction Electronics*, 87(5):694–699.

Kik, A. (2016). Complex permittivity measurement using a ridged waveguide cavity and the perturbation method. *IEEE Transactions on Microwave Theory and Techniques*, 64(11):3878–3886.

Kobayashi, Y. and Minegishi, M. (1988). A bandpass filter using electrically coupled $TM_{01\delta}$ dielectric rod resonators. In *IEEE MTT-S International Microwave Symposium Digest, New York*, pages 507–510.

Kraszewski, A. and Nelson, S. (1991a). Microwave resonator as a dielectric object sorting device: Advantages and limitations. In *Proceedings of the 21st European Microwave Conference, Stuttgart*, pages 435–440.

Kraszewski, A. and Nelson, S. (1991b). Sorting biological objects with microwave resonant cavities. In *IEEE Instrumentation and Measurement Technology Conference, Atlanta*, pages 40–43.

Kraszewski, A. and Nelson, S. (1994). Resonant-cavity perturbation measurement for mass determination of the perturbing object. In *IEEE Instrumentation and Measurement Technology Conference, Hamamatsu*, pages 1261–1264.

Kraszewski, A. W. and Nelson, S. O. (1992). Observations on resonant cavity perturbation by dielectric objects. *IEEE Transactions on Microwave Theory and Techniques*, 40(1):151–155.

Krupka, J. (2006). Frequency domain complex permittivity measurements at microwave frequencies. *Measurement Science and Technology*, 17(6):55–70.

Kumar, A. and Singh, G. (2007). Measurement of dielectric constant and loss factor of the dielectric material at microwave frequencies. *Progress In Electromagnetics Research*, 69:47–54.

Kumar, A. and Smith, D. G. (1977). Microwave properties of yarns and textiles using a resonant microwave cavity. *IEEE Transactions on Instrumentation and Measurement*, 26(2):95–98.

Lakshminarayana, M. R., Partain, L. D., and Cook, W. A. (1979). Simple microwave technique for independent measurement of sample size and dielectric constant with results for a gunn oscillator system. *IEEE Transactions on Microwave Theory and Techniques*, 27(7):661–665.

Lee, J. and Eom, H. (1996). Electrostatic potential through a circular aperture in a thick conducting plane. *IEEE Transactions on Microwave Theory and Techniques*, 44(2):341–343.

Lee, J. and Eom, H. (1998). Magnetostatic potential distribution through a circular aperture in a thick conducting plane. *IEEE Transactions on Electromagnetic Compatibility*, 40(2):97–99.

Li, S. and Bosisio, R. G. (1982). Composite hole conditions on complex permittivity measurements using microwave cavity perturbation techniques (Short Papers). *IEEE Transactions on Microwave Theory and Techniques*, 30(1):100–103.

Lin, M. and Afsar, M. N. (2006). A new cavity perturbation technique for accurate measurement of dielectric parameters. In *IEEE MTT-S International Microwave Symposium Digest, San Francisco*, pages 1630–1633.

Marcuvitz, N. (1986). *Waveguide Handbook*. Wiley-IEEE Press, New York.

Martinelli, M., Rolla, P. A., and Tombari, E. (1985). A method for dynamic dielectric measurements at microwave frequencies : applications to polymerization process studies. *IEEE Transactions on Instrumentation and Measurement*, 34(3):417–421.

McDonald, N. (1972). Electric and magnetic coupling through small apertures in shield walls of any thickness. *IEEE Transactions on Microwave Theory and Techniques*, 20(10):689–695.

Meng, B., Booske, J., and Cooper, R. (1995). Extended cavity perturbation technique to determine the complex permittivity of dielectric materials. *IEEE Transactions on Microwave Theory and Techniques*, 43(11):2633–2636.

Meyer, W. (1977). Dielectric measurements on polymeric materials by using superconducting microwave resonators. *IEEE Transactions on Microwave Theory and Techniques*, 25(12):1092–1099.

Meyer, W. and Schilz, W. M. (1981). Feasibility study of density-independent moisture measurement with microwaves. *IEEE Transactions on Microwave Theory and Techniques*, 29(7):732–739.

Microwaves101 (2018). *https://www.microwaves101.com/encyclopedias/even-and-odd-mode-impedances, Even and odd mode impedances*.

Narayanan, P. M. (2014). Microstrip transmission line method for broadband permittivity measurement of dielectric substrates. *IEEE Transactions on Microwave Theory and Techniques*, 62(11):2784–2790.

Ocera, A., Dionigi, M., Fratticcioli, E., and Sorrentino, R. (2006). A novel technique for complex permittivity measurement based on a planar four-port device. *IEEE Transactions on Microwave Theory and Techniques*, 54(6):2568–2574.

Parkash, A., Vaid, J., and Mansingh, A. (1979). Measurement of dielectric parameters at microwave frequencies by cavity-perturbation technique. *IEEE Transactions on Microwave Theory and Techniques*, 27(1):791–795.

Penaranda-Foix, F. L., Catala-Civera, J. M., Canos-Marin, A. J., and Garcia-Banos, B. (2007). Frequency deviation due to a sample insertion hole in a cylindrical cavity by circuital analysis. In *IEEE MTT-S International Microwave Symposium Digest, Honolulu*, pages 1683–1686.

Peng, Z., Hwang, J. Y., and Andriese, M. (2014). Maximum sample volume for permittivity measurements by cavity perturbation technique. *IEEE Transactions on Instrumentation and Measurement*, 63(2):450–455.

Piekarz, I., Sorocki, J., Wincza, K., and Gruszczynski, S. (2016a). Coupled-line sensor with Marchand balun as RF system for dielectric sample detection. *IEEE Sensors Journal*, 16(1):88–96.

Piekarz, I., Sorocki, J., Wincza, K., and Gruszczynski, S. (2016b). Effective permittivity measurement with the use of coupled-line section sensor. In *IEEE Radio and Wireless Symposium RWS, Austin*, pages 165–168.

Pozar, D. M. (2011). *Microwave Engineering*. John Wiley & Sons, New York.

Rieter GmbH (2017). *http://www.rieter.com/en/rikipedia/articles/spinning-preparation, Spinning preparation Online Article*.

Rouleau, J. F., Goyette, J., Bose, T. K., and Fréchette, M. F. (2001). Optimization study of a microwave differential technique for humidity measurement in gases. *IEEE Transactions on Instrumentation and Measurement*, 50(3):839–845.

Saeed, K., Shafique, M. F., Byrne, M. B., and Hunter, I. C. (2002). Planar microwave sensors for complex permittivity characterization of materials and their applications. *Applied Measurement Systems*, pages 319–350.

Santra, M. and Limaye, K. U. (2005). Estimation of complex permittivity of arbitrary shape and size dielectric samples using cavity measurement technique at microwave frequencies. *IEEE Transactions on Microwave Theory and Techniques*, 53(2):718–721.

Sheen, J. (2009). Study of microwave dielectric properties measurements by various resonance techniques. *Measurement Science and Technology*, 37(2):123–130.

Sheen, J. and Weng, C. M. (2016). Modifications of the cavity perturbation technique for permittivity measurements of laminated samples. *IEEE Transactions on Dielectrics and Electrical Insulation*, 23(1):532–536.

Shete, M., Shaji, M., and Akhtar, M. J. (2013). Design of a coplanar sensor for RF characterization of thin dielectric samples. *IEEE Sensors Journal*, 13(12):4706–4715.

Shihe, L., Akyel, C., and Bosisio, R. (1981). Precise calculations and measurements on the complex dielectric constant of lossy materials using $TM_{010}$ cavity perturbation techniques. *IEEE Transactions on Microwave Theory and Techniques*, 29(10):1041–1048.

Siddiqui, O. F. and Ramahi, O. M. (2011). A novel dielectric detection system based on wire-loaded waveguides. *IEEE Microwave and Wireless Components Letters*, 21(2):2010–2012.

Stuchly, M. A., Stuchly, M. A., and Stuchly, S. S. (1980). Coaxial line reflection methods for measuring dielectric properties of biological substances at radio and microwave frequencies: A Review. *IEEE Transactions on Instrumentation and Measurement*, 29(3):176–183.

Stuchly, S. S. and Hamid, M. A. K. (1971). State of art in microwave sensors for measuring non-electrical quantities. *International Journal of Electronics*, 71(1):142–143.

Subramanian, V., Sivasubramanian, V., Murthy, V., and Sobhanadri, J. (1996). Measurement of complex dielectric permittivity of partially inserted samples in a cavity perturbation technique. *Review of Scientific Instruments*, 67(1):279–282.

Thomas, R. and Dube, D. (1997). Extended technique for complex permittivity measurement of dielectric films in the microwave region. *Electronics Letters*, 33(3):218–220.

Thomassen, K. I. (1965). Microwave plasma density measurements. *Journal of Applied Physics*, 36(11):3642–3644.

Tyurnev, V. V. (2010). Coupling coefficients of resonators in microwave filter theory. *Progress In Electromagnetics Research B*, 21:47–67.

Venkatesh, M. S. and Raghavan, G. S. V. (2005). An overview of dielectric properties measuring techniques. *Canadian Biosystems Engineering / Le Genie des biosystems au Canada*, 47:715–730.

Verma, A. and Dube, D. C. (2005). Measurement of dielectric parameters of small samples at X-band frequencies by cavity perturbation technique. *IEEE Transactions on Instrumentation and Measurement*, 54(5):2120–2123.

Waldron, R. A. (1960). Perturbation theory of resonant cavities. *Proceedings of the IEE Part C: Monographs*, 107(12):272.

Wang, Z., Javadi, H., and A.J., E. (1991). Application of microwave cavity perturbation techniques in conducting polymers. In *IEEE Instrumentation and Measurement Technology Conference, Atlanta*, pages 79–82.

Wheeler, H. (1964). Coupling holes between resonant cavities or waveguides evaluated in terms of volume ratios. *IEEE Transactions on Microwave Theory and Techniques*, 12(2):231–244.

Zverev, A. I. (2005). *Handbook of Filter Synthesis*. John Wiley & Sons, New York.

# List of Publications of the Author

Faz, U. and Eibert, T. F. (2019). A coupled-cavity resonator technique for simultaneous mass and position detection of continuous dielectric material streams. To be submitted.

Faz, U., Siart, U., and Eibert, T. F. (2015a). A cylindrical cavity resonator for material measurements with coupled resonant modes for sensing and position offset compensation of the dielectric specimen. In *German Microwave Conference*, Nuremberg.

Faz, U., Siart, U., Eibert, T. F., and Hermann, T. (2015b). Electric field homogeneity optimization by dielectric inserts for improved material sensing in a cavity resonator. *IEEE Transactions on Instrumentation and Measurement*, 64(8):2239—2246.